SAND2016-7649R

SANDIA REPORT

SAND
Printed August 2016

Filtration testing for enhanced performance of Radionuclide Monitoring Stations for Nuclear Treaty Verification

Joshua Hubbard, Dora Wiemann, Jill Wheeler, Michael Omana, Jamie Gerard, Sean Fournier, Stephen, Stromberg, and Elliott Leonard

Prepared by
Sandia National Laboratories, MS-0968
Albuquerque, New Mexico 87185 and Livermore, California 94550

Sandia National Laboratories is a multi-program laboratory managed and operated by Sandia Corporation, a wholly owned subsidiary of Lockheed Martin Corporation, for the U.S. Department of Energy's National Nuclear Security Administration under contract DE-AC04-94AL85000.

Sandia National Laboratories

Issued by Sandia National Laboratories, operated for the United States Department of Energy by Sandia Corporation.

SAND2016-
Printed August 2016

Filtration testing for enhanced performance of Radionuclide Monitoring Stations for Nuclear Treaty Verification

Joshua Hubbard, Dora Wiemann, Jill Wheeler, Michael Omana, Jamie Gerard, Sean Fournier, Elliott Leonard, and Stephen Stromberg

Sandia National Laboratories
P.O. Box 5800 MS 0968
Albuquerque, New Mexico 87185

ABSTRACT

A study of aerosol filtration was conducted to improve U.S. Radionuclide Monitoring Station (RMS) performance for Nuclear Treaty Verification. The primary objectives of this study were to improve system operability and maintainability, reduce power consumption and operational cost, and reduce baseline radionuclide sensitivity. To meet these goals, Sandia National Laboratories (SNL) studied the performance of alternate filter materials and aerosol collection technologies that could be engineered into U.S. Radionuclide Monitoring Stations. Laboratory-scale filtration experiments were conducted with Filter Material 1, FM1 (current filter), Filter Material 2, FM2, and Filter Material 3, FM3. All three materials employ electrostatically charged filter fibers to enhance nanoparticle collection. FM2 and FM3 both had higher air permeability with respect to FM1 which is advantageous for high volume collection and power savings. Particle pre-charging, a well-established industrial technique used in electrostatic precipitators, was tested to see if electrostatically charging particles prior to filtration could enhance filter performance. We found that particle-pre-charging did enhance aerosol collection efficiencies for materials which would not have otherwise satisfied RMS performance requirements. Laboratory-scale testing indicated it may be possible to reduce the baseline radionuclide sensitivity to approximately 60% of its current value by increasing the volume of air sampled in 24 hours to 2.5 times the current air volume. Improvements to geolocation may also be possible with shorter air samples (e.g., 12 hours). A new methodology was developed at SNL to assess filter performance using established RMS certification procedures. We coined these tests "mid-scale" since they bridged the gap between laboratory-scale and full-scale RMS testing. Four filter specimens were drawn from the exact same atmospheric aerosol. Gamma spectroscopy was used to assess radiological backgrounds due to radon progeny and other naturally occurring radionuclides. Direct comparisons between the four filters allowed SNL to quantify the relative change in baseline sensitivity by altering air flow rate, filter material, and particle-pre-charging. Mid-scale results agreed with laboratory-scale results: alterations to RMS configuration (filter, flow, and particle charge) may result in baseline sensitivities approximately 55-60% of their current values. Finally, an assessment of scalability was performed to determine if technical approaches used in laboratory-scale and mid-scale testing could be engineered into full-scale Radionuclide Monitoring Stations. Results suggested that particle-pre-charging is a viable technical approach if reductions in baseline sensitivity or power consumption are desired.

ACKNOWLEDGMENTS

This work was funded by the Nuclear Arms Control Technologies Office of the Defense Threat Reduction Agency.

CONTENTS

Abstract 3
Acknowledgments 4
Contents 5
Figures 7
Tables 11
Nomenclature 13
Executive Summary 14
1 Introduction 17
1.1 Radionuclide Aerosol Sampler and Analyzer (RASA) 17
1.2 Current Filter Media 19
1.3 System Requirements 19
2 Laboratory scale filtration testing 21
2.1.1 Filter Test Bed 21
2.1.2 Test Matrix 26
2.1.3 Materials 27
2.2 Calculations 33
2.2.1 Particle Diameter Conversion 33
2.2.2 Collection Efficiency 34
2.2.3 Neutralizer Dead Volume Correction 34
2.3 Data 36
2.3.1 Filter Pressure Drop 36
2.3.2 Aerosol Collection Efficiency 38
3 Mid-scale filtration testing 45
3.1 Background 45
3.2 Aerosol Collection 46
3.2.1 Test Setup 46
3.2.2 Mid-scale test system performance validation 59
3.2.3 Data 60
3.3 Radiometric methods 72
3.3.1 Introduction 72
3.3.2 Theory 73

3.3.3 Experiment and Data Reduction Methods....77
3.3.4 Experiment Plan....78
3.4 Data....79
3.4.1 Results and Discussion....81
3.4.2 Summary and Conclusion....84
4 Discussion....85
4.1 Weighted average collection efficiency....85
4.2 Electrostatic effects....95
4.2.1 Space charge effect....98
4.2.2 Analysis....99
5 Recommendations....109
5.1 FM1, baseline, standard flow....109
5.2 FM1, particle pre-charging, standard flow....109
5.3 FM2, no particle pre-charging, standard flow....109
5.4 FM2, particle pre-charging, standard flow....111
5.5 FM2, no particle pre-charging, marginally increased flow....111
5.6 FM2, particle pre-charging, marginally increased flow....111
5.7 FM2, no particle pre-charging, 2.5x flow....111
5.8 FM2, particle pre-charging, 2.5x flow....112
5.9 FM3, particle pre-charging, standard flow....112
5.10 FM3, particle pre-charging, 2.5x flow....112
References....113
Distribution....115

FIGURES

Figure 1. Radionuclide Aerosol Sampler Analyzer (RASA): 21 Mar 2014 - Radionuclide Station RN23 Rarotonga, Cook Islands. Image taken from www.CTBTO.org. 17

Figure 2. Global network of Radionuclide Aerosol Sampler Analyzers (RASA) constituting the International Monitoring System (IMS). R+ denotes a RASA installation with noble gas collection. As of 2016 June 08, 63 stations have been installed and certified with 17 others planned, under construction, or installed. Image taken from www.CTBTO.org. 18

Figure 3. Aerosol number concentration plotted against particle diameter for NaCl test aerosol 22

Figure 4. Laboratory scale filter test system developed in 2009 and utilized in Harvester and RASA research and development....23

Figure 5. Particle pre-charging apparatus to impart unipolar electrical charge on aerosol particles for enhanced collection efficiency....25

Figure 6. Five point pinner electrostatic charging applicator used to create a corona discharge, ionize air, and charge aerosol particles....25

Figure 7. S1 scrim material used in current RASA filter material 27

Figure 8. S2 proposed substitute scrim material with low pressure drop with respect to S1 28

Figure 9. FM1 filter fibers coated in ISO test dust after a laboratory scale collection efficiency measurement 29

Figure 10. FM1 filter fibers coated in sodium chloride aerosol after a laboratory scale collection efficiency measurement 30

Figure 11. FM2 filter material proposed as substitute for FM1 31

Figure 12. FM3 filter material proposed as substitute for FM1 32

Figure 13. Filter pressure drop (ΔP_d) vs. filter face velocity (U) for FM1, FM2, FM3 and 2 layers of scrim materials S2 and S1. Filter materials FM2, and FM3 were sandwiched between two layers of S2. FM1 was sandwiched between two layers of S1. 37

Figure 14. Aerosol collection efficiency (E) plotted against aerodynamic equivalent particle diameter (d_a) for FM1 at filter face velocities of 1.1, 2.75, and 5.5

m/s, and electrostatically charged in negative and positive coronas, and to the Boltzmann charge distribution (neutral or uncharged).....39

Figure 15. Aerosol collection efficiency (E) plotted against aerodynamic equivalent particle diameter (d_a) for FM2 at filter face velocities of 1.1, 2.75, and 5.5 m/s, and electrostatically charged negatively, positively, and to the Boltzmann charge distribution (neutral). 40

Figure 16. Aerosol collection efficiency (E) plotted against aerodynamic equivalent particle diameter (d_a) for FM2 at filter face velocities and electrostatic charge states that would satisfy CTBT requirements for RASA collections. 41

Figure 17. Aerosol collection efficiency (E) plotted against aerodynamic equivalent particle diameter (d_a) for FM3 at filter face velocities of 1.1, 2.75, and 5.5 m/s, and electrostatically charged negatively, positively, and to the Boltzmann charge distribution (neutral). 42

Figure 18. Aerosol collection efficiency (E) plotted against aerodynamic equivalent particle diameter (d_a) for FM3 at filter face velocities and electrostatic charge states that would satisfy CTBT requirements for RASA collections. 43

Figure 19. 10" diameter sampling duct use to draw in ambient air to the mid-scale filter test system.....49

Figure 20. Sampling plenum used to pre-charge aerosol particles with unipolar ions and measure ambient aerosol concentration prior to distribution of aerosol into four separate filter sections.....50

Figure 21. Interior of aerosol sampling plenum 51

Figure 22. Exit of aerosol sampling plenum into four separate filter sampling sections of equal particle-air concentration 52

Figure 23. Individual filter sampling section with upstream aerosol sampling probe and diaphragm control valve 53

Figure 24. Mid-scale test system side-view showing aerosol sampling plenum and four separate filter sampling sections 54

Figure 25. Mid-scale test system side-view showing aerosol sampling plenum, four separate filter sampling sections, aerosol instrumentation, data acquisition system, and power supply for ion generators.....55

Figure 26. Mid-scale test system rear-view showing air exhaust (vacuum) plenum, laminar flow elements used to measure air flow, and HEPA filters used to clean the air stream prior to entry into the laminar flow element.....56

Figure 27. Data acquisition system and differential pressure transducers used to measure air flow rates in each of the filter sampling sections.....57

Figure 28. Aerosol instrumentation used to size and count aerosol particles in air stream and ion generator power supply used to pre-charge aerosol particles.....58

Figure 29. nSMPS total concentration (cm^{-3}) as a function of sampling time during the first hour of sampling. The total concentration varies 10-20% over time intervals of 5-10 minutes.....71

Figure 30: High-Purity Germanium (HPGe) Gamma Spectrometer. Low-background graded shield, liquid nitrogen cooled.....73

Figure 31: Gamma Spectrum for Trial 1, Configuration 3 (in black) compared to a background spectrum (in blue).....76

Figure 32: Comparison of Pb-212 Activity on Baseline Trial 000 Filters in Configuration 1.....80

Figure 33. Aerosol number distribution plotted against particle size for "standard" atmospheric aerosol parameters taken from Whitby and Sverdrup (1980).....88

Figure 34. Cumulative aerosol number distribution plotted against particle size for "standard" atmospheric aerosol parameters taken from Whitby and Sverdrup (1980). Ordinate (y-axis) values can be interpreted as the percent of the total number of particles in the aerosol distribution with sizes less than the abscissa value (d_p). Greater than 95% of the particles, by number, have particle diameters less than 100 nm.....89

Figure 35. Aerosol surface area distribution plotted against particle size for "standard" atmospheric aerosol parameters taken from Whitby and Sverdrup (1980).....90

Figure 36. Cumulative aerosol surface area distribution plotted against particle size for "standard" atmospheric aerosol parameters taken from Whitby and Sverdrup (1980). Ordinate (y-axis) values can be interpreted as the percent of the total surface area of particles in the aerosol distribution with sizes less than the abscissa value (d_p).....91

Figure 37. Mathematical weighting function for aerosol collection efficiency based on atmospheric aerosol number and surface area distributions.....93

Figure 38. Aerosol number concentration for NaCl test aerosol in laboratory scale system. Data are given for uncharged aerosol, positively charged aerosol, and negatively charged aerosol.....96

Figure 39. Ratio of charged to uncharged particle concentration for positively, and negatively, charged NaCl test aerosol particles in the laboratory scale test system.....97

Figure 40. Particle charge associated with diffusion and field charging mechanisms for laboratory scale tests and mid-scale tests 102

Figure 41. Combined particle charge for laboratory scale tests and mid-scale tests compared to theoretical particle charge limit 103

Figure 42. Aerosol number distribution for NaCl aerosol used in laboratory experiments. Data fitted with lognormal distribution. 104

Figure 43. Radial component of electric field inside pipe due to space charge effect..... 105

Figure 44. Estimated terminal electrostatic migration velocities for mid-scale and laboratory-scale testing, along with gravitational settling velocity of particles with density of 2300 kg m^{-3} 106

Figure 45. Charged particle penetration through laboratory-scale tubing (2" OD), mid-scale test inlet (14" OD), and aerosol sampling tubing (1/4" OD) along with cumulative surface area distribution for atmospheric aerosol. 108

TABLES

Table 1. CTBT Radionuclide Monitoring Station Performance Requirements taken from CTBTO (2010). 20

Table 2. Particle properties for filter challenge aerosols. NaCl data were taken from the work of Spencer et al. (2007) and ISO 12103-1 data were taken from Endo et al. (1999) 22

Table 3. Variable definitions for neutralizer dead volume corrections 35

Table 4. Variable definitions for equation (6), Minimum Detectable Concentration (MDC) 45

Table 5. Beginning and end air flow rates (Q) for each filter sample and trial 60

Table 6. Test Configuration Details 62

Table 7. Trial numbers and filter configurations where “x” represents a single filter sample being included in the trial 63

Table 8. Radionuclides of interest for treaty monitoring 72

Table 9: HPGe Detector Relative Efficiencies 74

Table 10. Correction factors for each detector and each radionuclide of interest. The correction factor is ratio of LAB01 MDA to the MDA of each detector for the given nuclide. 74

Table 11. Minimum Detectable Activity for a 60 min count of a 2" air filter on contact (units are arbitrary) 75

Table 12. Normalized MDAs for a 60 min count of a 2" air filter on contact (units are arbitrary) 75

Table 13. Detector Correction Factors 80

Table 14. Relative Uncertainty in the Detector Correction Factor 81

Table 15. Mid-Scale Testing Results Summary 83

Table 16. Variable definitions for equation (14), tri-modal, lognormal, aerosol particle size distribution 86

Table 17. Tri-modal, lognormal, atmospheric particle size distribution parameters from Whitby and Sverdup (1980) 87

Table 18. Weighted aerosol collection efficiencies for FM1, FM2, and FM3 for filter face velocities of 1.1, 2.75, and 5.5 m/s, and particle charge states of negative, positive, and neutral. 94

Table 19. Estimated and measured parameters used to calculate particle charge for laboratory and mid-scale filtration tests....101

Table 20. Recommended RASA configurations for power savings and reduction of minimum detectable concentration (MDC)....110

NOMENCLATURE

ACFM	Air flow rate - actual cubic feet per minute
APS	Aerodynamic Particle Sizer
CTBT	Comprehensive Test Ban Treaty
CTBTO	Comprehensive Test Ban Treaty Organization
DTRA	Defense Threat Reduction Agency
FM1	Blown microfiber, 20 weight, Fine fibers (current RASA filter material)
FM2	Blown microfiber, 40 weight, Coarse fibers (proposed RASA filter material)
FM3	Filter media, ribbon-like fibers, electrostatically charged (proposed RASA filter material)
GD	General Dynamics Company
HEPA	High Efficiency Particulate Air
HPGe	High purity germanium detector
IMS	International Monitoring System
ISO	International Standards Organization
LFE	Laminar Flow Element
MDC	Minimum Detectable Concentration
nSMPS	Nanoscan Scanning Mobility Particle Sizer
OPS	Optical Particle Sizer
PA6	Nylon
PET	Polyethylene terephthalate
PNNL	Pacific Northwest National Laboratory
PSIA	Absolute pressure - pounds per square inch
PSID	Differential pressure - pounds per square inch
RASA	Radionuclide Aerosol Sampler and Analyzer
RMS	Radionuclide Monitoring Station
RN	Radionuclide Station (same as RMS)
RN+	Radionuclide Station with noble gas collection
S1	Scrim material 1 (current RASA filter scrim)
S2	Scrim material 2 (proposed RASA filter scrim)
SEM	Scanning electron microscopy
SMPS	Scanning Mobility Particle Sizer
SNL	Sandia National Laboratories

EXECUTIVE SUMMARY

The Radionuclide Aerosol Sampler Analyzer (RASA) is the U.S. system designed to support the Comprehensive Test Ban Treaty (CTBT) through the collection and analysis of aerosols which may be generated during nuclear weapons testing. The U.S. operates and maintains 11 Radionuclide Monitoring Stations (RMS). The objectives of this study were to (1) improve system maintainability and operability, (2) reduce power consumption and operational cost, (3) and reduce baseline radionuclide sensitivity for enhanced performance. We addressed these objectives through testing and evaluation of alternate filter materials at increased air flow rates. We also developed and studied the use of particle-pre-charging as a novel approach to enhance performance. Increasing air flow rates may also lead to collections on a shorter time intervals which could improve the capability to geolocate radionuclide sources.

The first task of this study was to perform laboratory-scale tests of filter materials using Sandia National Laboratories' distinguishing aerosol measurement capability. These types of tests have been performed extensively under previously funded research and development projects for airborne and ground-borne aerosol collection systems. Aerosol collection efficiencies were measured for particles ranging from approximately 10 nanometers to 5 micrometers for three different filter materials: (1) Filter Material 1, FM1 (current RASA material), (2) FM2, and (3) FM3. All three filter materials employ electrostatically charged polymer fibers to capture nanoparticles (< 200 nanometers) efficiently. Aerosol collection efficiency curves were measured at three filter face velocities: (1) the current filter face velocity of the RASA, (2) 2.5 times the filter face velocity of the RASA, and (3) 5.0 times the filter face velocity of the RASA. Particle-pre-charging was developed to enhance performance at higher filter face velocities. Electrostatically charging aerosol particles upstream of aerosol collectors is used in industrial scale electrostatic precipitators. Electrostatically charged aerosol particles experience additional body forces in electric fields which can be exploited to capture those particles on filter fibers.

Good performance was observed for all materials where different flow configurations were tested to provide enhanced baseline sensitivity or power reduction. From laboratory-scale testing, the major conclusions were that FM2 can be used in the RASA to provide moderate improvements to baseline sensitivity and power consumption without substantial system

modifications, and FM3 may be used with particle-pre-charging to attain baseline sensitivities approximately 55-60% of current values. FM3 may also result in more substantial power savings with respect to FM2. Some engineering changes would be necessary to integrate FM3 for enhanced baseline sensitivity and power savings.

Sandia National Laboratories developed and executed mid-scale filtration tests to bridge the gap between laboratory-scale testing and full-scale testing. Full-scale testing would only be possible with RASA test beds available at General Dynamics (GD) or Pacific Northwest National Laboratory (PNNL). The SNL mid-scale approach was developed to compare filters after having been exposed to the same ambient aerosol. Gamma spectroscopy and approved RASA certification methods were used to quantify relative changes in baseline sensitivity for different filters, flow configurations, and particle charges. Mid-scale tests were guided by results from laboratory-scale tests and resulted in complementary data. Mid-scale tests confirmed that alternate RASA configurations could be used to obtain baseline sensitivities 55-60% of their current values using methods similar to RMS certification protocols.

The particle-pre-charging approach was analyzed for feasibility and scalability of implementation into fielded RASAs. Laboratory-scale tests showed that particle losses occurred inside the laboratory-scale test apparatus when particle-pre-charging was employed. Theoretical analysis of electrostatic aerosol transport was performed. Our analysis showed that particle-pre-charging is most likely scalable and could be implemented without particle losses in fielded RASAs. High electric fields in close proximity to corona charging devices should be avoided, and particle-pre-charging should be implemented close to the filter to avoid particle losses upstream of the filter material.

The following recommendations were made based on laboratory-scale and mid-scale testing.

- FM2 could be used in place of FM1 to obtain marginal improvements to air flow and baseline sensitivity (5-10% of current values) without substantial engineering modifications to the RASA. Based on this study, this low risk option may provide moderate performance enhancements.
- FM3 could be used in place of FM1 to obtain more moderate improvements to air flow and baseline sensitivity (55-60% of current values). This approach would require the engineering and implementation of particle-pre-charging in fielded RASAs thereby

representing more technical risk. FM3 may be suitable for some aerosol samplers and not others. Changes to the RASA blower system would likely be required to obtain the flows necessary for this reduction in baseline sensitivity. An engineering study is recommended prior to system implementation. However, the current filtration study lays a foundation for particle-pre-charging in full-scale RASA systems.

1 INTRODUCTION

1.1 Radionuclide Aerosol Sampler and Analyzer (RASA)

A network of Radionuclide Monitoring Stations (RMS) is used to monitor for comprehensive nuclear test ban treaty compliance (CTBT) as a part of the International Monitoring System (IMS). Radionuclide stations consist of an automated collection and analysis system for aerosol particles containing radionuclides. The U.S. developed Radionuclide Monitoring Station was designed by Pacific Northwest National Laboratory (PNNL) and is called the Radionuclide Aerosol Sampler Analyzer (RASA). RMS is a general term. RASA is the U.S. system. System design and performance features can be found in Miley et al. (1998) and Forrester et al. (2012). The system samples aerosols for 24 hours, allows background radiation to decay for 24 hours, and then counts the radiation spectrum for 24 hours with a high purity germanium detector (HPGe). The total flow of the system is approximately 1000 cubic meters per hour of air (m^3 h^{-1}) which is filtered by 0.25 m^2 of electrostatically charged FM1 blown microfiber filter media. The baseline radionuclide sensitivity for each station is 10 µBq m^{-3} Ba-140 in air. The power consumption for a radionuclide and noble gas station is on the order of several kilowatts (CTBT 2010).

Figure 1. Radionuclide Aerosol Sampler Analyzer (RASA): 21 Mar 2014 - Radionuclide Station RN23 Rarotonga, Cook Islands. Image taken from www.CTBTO.org.

An image of RN23 (Radionuclide Station 23), Rarotonga, Cook Islands, is shown in Figure 1. The global IMS network is shown in Figure 2. The United States is responsible for operations and maintenance of 11 radionuclide monitoring aerosol systems (symbol R) and 4 xenon noble gas systems (symbol R+). General Dynamics (GD) is responsible for operations and maintenance of U.S. radionuclide stations.

Figure 2. Global network of Radionuclide Aerosol Sampler Analyzers (RASA) constituting the International Monitoring System (IMS). R+ denotes a RASA installation with noble gas collection. As of 2016 June 08, 63 stations have been installed and certified with 17 others planned, under construction, or installed. Image taken from www.CTBTO.org.

1.2 Current Filter Media

FM1 (electrostatically blown microfibers, fine fibers) is the filter media currently utilized in the RASA. The polypropylene fibers are electrostatically charged to enhance the capture of nanoparticles which are not captured as efficiently in non-electrostatic filter media. Thompson et al. (2002) originally selected this media based on measurements provided by a research organization in Finland (Valmari et al. 2000). Under NA-22 and DTRA NTV funding, SNL has performed additional characterization of FM1 (Hubbard et al. 2012a, Hubbard et al. 2013, Hubbard et al. 2014, Sanchez et al. 2013). SNL found that electrostatic effects were more dominant at lower filter face velocities (0.5 m/s) with some particle losses at 1.5 m/s and 2.5 m/s for supra-micrometer particles due to inertial particle rebound. The addition of retention agents to the surfaces of polymer fibers was moderately successful for enhancing particle capture and mitigating particle losses at lower velocities.

1.3 System Requirements

Minimum system requirements are specified by CTBTO (2010) and are provided in Table 1. The objective of this study was to enhance RASA performance through any combination of the following performance parameters:

1. reduced power consumption (reduced operational cost and deployment to remote locations),
2. reduced baseline sensitivity for Ba-140,
3. improved air flow,
4. reduction in collection time for enhanced geolocation, and
5. enhanced data availability (reduced downtime).

Many of these performance metrics are coupled. For instance, increasing airflow decreases the minimum detectable concentration of Ba-140. However, increasing airflow generally requires more power consumption and a larger blower to pull higher air flows at increased system pressure drop. The required minimum aerosol collection efficiency of 80% at 200 nanometers (nm) is also challenging since increased airflow generally reduces the performance of electrostatically charged filters. The coupling between performance parameters makes system optimization a challenge. For system enhancement, aerosol collection efficiency

must be improved or maintained while other performance enhancing measures generally counteract filter collection mechanisms.

Table 1. CTBT Radionuclide Monitoring Station Performance Requirements taken from CTBTO (2010).

Characteristics	Minimum Requirements
System	Manual or automated
Airflow	500 m^3/hour
Collection time[a]	24 hours
Decay time[b]	≤24 hours
Measurement time[c]	≥20 hours
Time before reporting	≤3 days
Reporting frequency	Daily
Filter	Adequate composition for compaction, dissolution and analysis
Particulate collection efficiency	For filter: ≥80% at ∅ = 0.2 µm Global[d]: ≥60% at ∅ = 10 µm
Measurement mode	High purity germanium high resolution gamma ray spectrometry
High purity germanium relative efficiency	≥40%
High purity germanium resolution	<2.5 keV at 1332 keV
Baseline sensitivity[e,f]	10 to 30 µBq/m^3 for Ba-140
Calibration range	88 to 1836 keV
Data format for gamma spectra and auxiliary data	Radionuclide Monitoring System format[g]
State of health	Status data transmitted to International Data Centre
Communication	Two way
Auxiliary data	Meteorological data, flow rate measurement every 10 min
Data availability	≥95%
Downtime[h]	≤7 consecutive days ≤15 days annually

[a] Time specifications allow for an uncertainty of 10%, except for the reporting time parameter.
[b] This value can be reduced, to a minimum of 6 hours, if other stations or techniques detect a suspicious event.
[c] This value allows for authentication measurements for manual systems.
[d] This global value includes the 80% filter efficiency and the collection efficiency of the incoming air circuitry.
[e] The upper limit is intended for high background areas.
[f] Certification procedures to be defined for baseline sensitivities (a posteriori minimum detectable concentrations) as well as the efficiency. Sample preparation losses should not affect baseline sensitivities.
[g] This format should make provision for auxiliary data, authentication data and state of health data.
[h] Provision should be made for spare parts in particular areas where periodicity of transportation facilities is more than 7 days.

2 LABORATORY-SCALE FILTRATION TESTING

2.1.1 Filter Test Bed

A filter test system capable of operating at high filter face velocities, low air pressures, and low air temperatures, was constructed during the work of Dellinger et al. (2009, 2012) and Hubbard et al. (2012b) to characterize inertial filtration at filter face velocities ranging from 5.0 to 20.0 m/s and at air pressures ranging from 0.2 to 0.8 atmospheres. The system was modified during the work of Hubbard et al. (2012a) and Sanchez et al. (2013) to characterize the performance of electrostatically charged filter media at moderate filter face velocities ranging from 0.5 to 2.5 m/s at atmospheric pressure representative of the RASA aerosol sampling regime. The performance of FM1 at atypically high filter face velocities was also reported in Hubbard et al. (2013, 2014).

HEPA filtered air is drawn in to a 5.08 centimeter diameter (2 inch) stainless steel tube where test aerosol is injected and diaphragm valves are used to control the filter face velocity and air pressure in the filter test section. Air flow rates are measured using two laminar flow elements (Merriam Process Technologies, Cleveland, Ohio) with maximum air flow rates of 27.0 and 170.0 cubic meters per hour at a pressure drop of 8 inches of water. Two LFEs are needed to cover the range of flow rates studied in laboratory-scale tests. Two aerosols were generated to test collection efficiencies: Arizona road dust (ISO 12103-1 A2, 0.5-5.0 μm) dispersed with a fluidized bed, and sodium chloride (NaCl, 30-400 nanometers) atomized from solution.

Particle densities and shape factors for each particle type are given in

Table 2 where NaCl data were taken from the work of Spencer et al. (2007) and ISO 12103-1 data were taken from Endo et al. (1999). The measured NaCl particle size distribution is shown in Figure 3 and was fitted with a lognormal distribution utilizing the MATLAB curve fitting toolbox. The geometric mean diameter (d_g) was approximately 40 nanometers (nm) and the geometric standard deviation (σ_g) was approximately 1.76.

Table 2. Particle properties for filter challenge aerosols. NaCl data were taken from the work of Spencer et al. (2007) and ISO 12103-1 data were taken from Endo et al. (1999).

Property	Units	NaCl	ISO12103-1
ρ_p	(kg/m^3)	2040	2650
χ	(-)	1.11	1.5

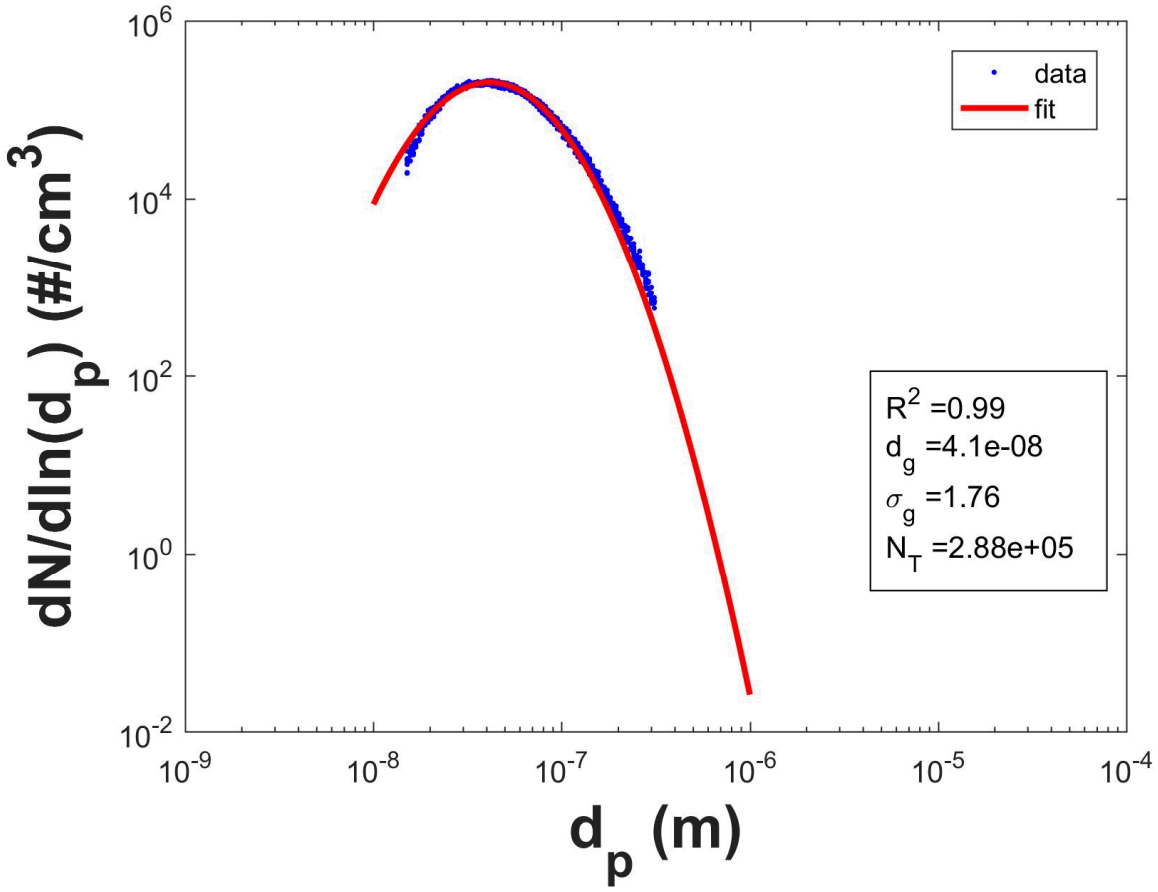

Figure 3. Aerosol number concentration plotted against particle diameter for NaCl test aerosol

Aerosol samples were taken upstream and downstream of the filter sample to calculate aerosol collection efficiency. Upstream and downstream measurements of aerosol concentration required approximately 5 minutes each including aerosol extraction from the filter test system and subsequent measurement by the SMPS and APS. A single experiment consisting of 6 measurements (3 upstream and 3 downstream samples) typically required 30-45 minutes

including test setup and data collection. Upstream and downstream measurements were alternated and the six aerosol concentration measurements constituted a single experiment. Each flow condition (e.g., filter face velocity) was measured in triplicate for both ISO and NaCl test aerosols. In the past both aerosols have been generated simultaneously but using multiple aerosol measurement instruments resulted in undesirable dilution of measured samples (low signal). Collection efficiency tests using NaCl and ISO aerosols were therefore conducted independently. A TSI Scanning Mobility Particle Sizer (SMPS) was used to measure aerosol size and concentration of NaCl aerosol (10-400 nm) and a TSI Aerodynamic Particle Sizer (APS) was used to measure the aerosol size and concentration of ISO test aerosol. Detailed experimental procedures, data analysis, and aerosol physics governing electrostatic and inertial aerosol filtration can be found in the following references: Dellinger et al. (2009, 2012), Hubbard et al. (2012a, 2012b, 2013, 2014), and Sanchez et al. (2013). Figure 4 shows the laboratory-scale filter test system used to characterize the performance of fibrous filters.

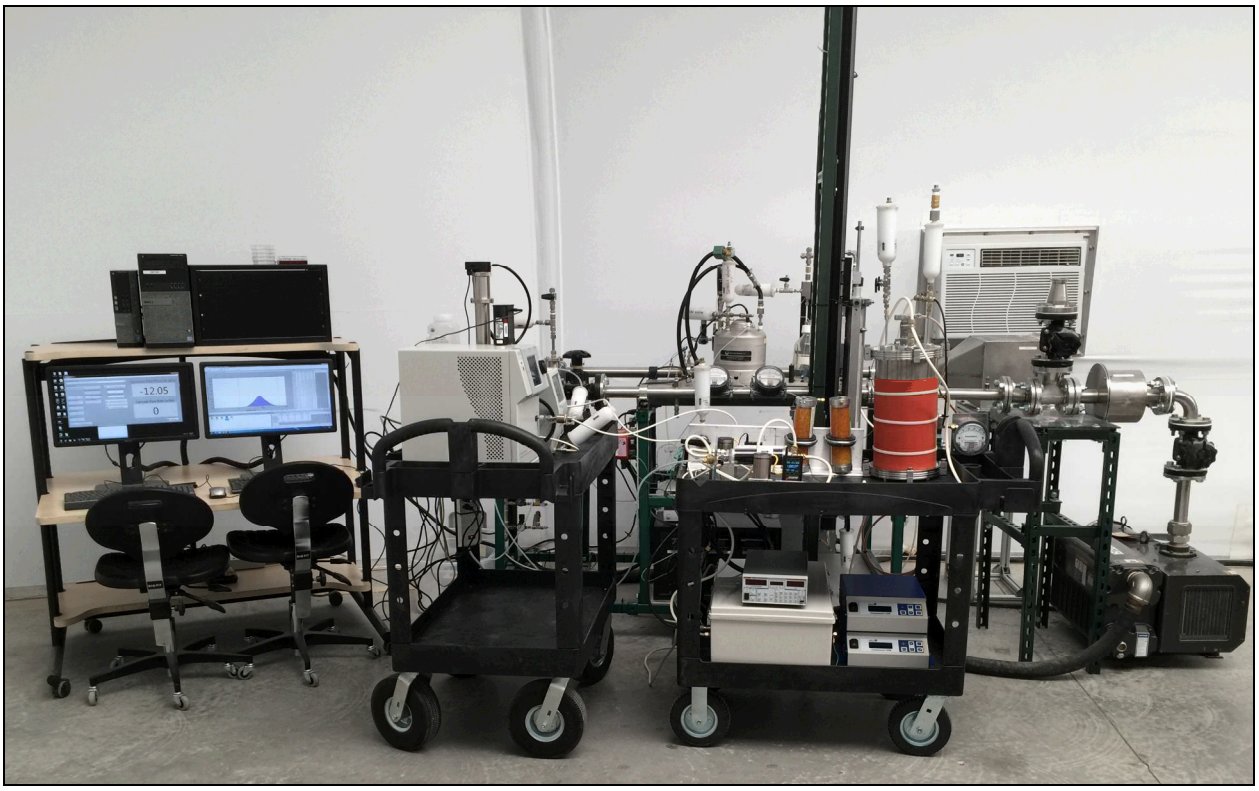

Figure 4. Laboratory scale filter test system developed in 2009 and utilized in Harvester and RASA research and development

The current RASA filtration media, FM1, uses electrostatically charged filter fibers to enhance the collection efficiency of nanoparticles. SNL has performed extensive studies of electrostatic filtration in the past. In the current study, we hypothesized that collection efficiency could be increased by electrostatically particle-pre-charging the aerosol particles. Particles in the atmosphere generally have some electrostatic charge, but it is small, and the charge distribution is centered about zero following a Poisson distribution. Electrostatic charges on filter fibers can polarize particles thereby creating a particle-fiber attraction force. Coulombic forces can also enhance particle-fiber capture if particles possess some charge. Particle-pre-charging was implemented in laboratory-scale testing to determine if aerosol collection efficiencies could be improved substantially through Coulombic attraction between fibers and highly charged particles.

The filter test system utilized in previous studies was altered to include particle-pre-charging. Figure 5 shows a section of the filter test bed upstream of the filter housing. Aerosol flows from left to right. Two ¾" bore-thru Swagelok fittings were welded onto a piece of 2" tube. Two particle pre-charging probes (SIMCO Ion Five Point Pinner Charging Applicator, model 4004738) were inserted approximately 2 cm into the air stream. Particle pre-charging probes ionized adjacent air through a corona discharge. The physics of particle charging and corona discharges will be included in the *Discussion* section. The tip of a particle-pre-charging probe is shown in Figure 6. For scale, the diameter of the pre-charging tip is ¾". The tips on the pre-charging probe were operated with a SIMCO Ion Chargemaster VCM Power Supply (VCM30-Bipolar) capable of creating positive or negative polarity corona discharges. The potential gradient at the sharp points of the pre-charging probe cause the adjacent air to become ionized by accelerating free electrons to create an electron avalanche in the gas phase. The air ions then attach to aerosol particles passing the probes in the air stream. Electrostatic diffusion charging and field charging of aerosols has been studied extensively and will be presented in the *Discussion*. Each probe was limited to approximately 250 μA output current corresponding to a power supply voltage of approximately 25-30 kV.

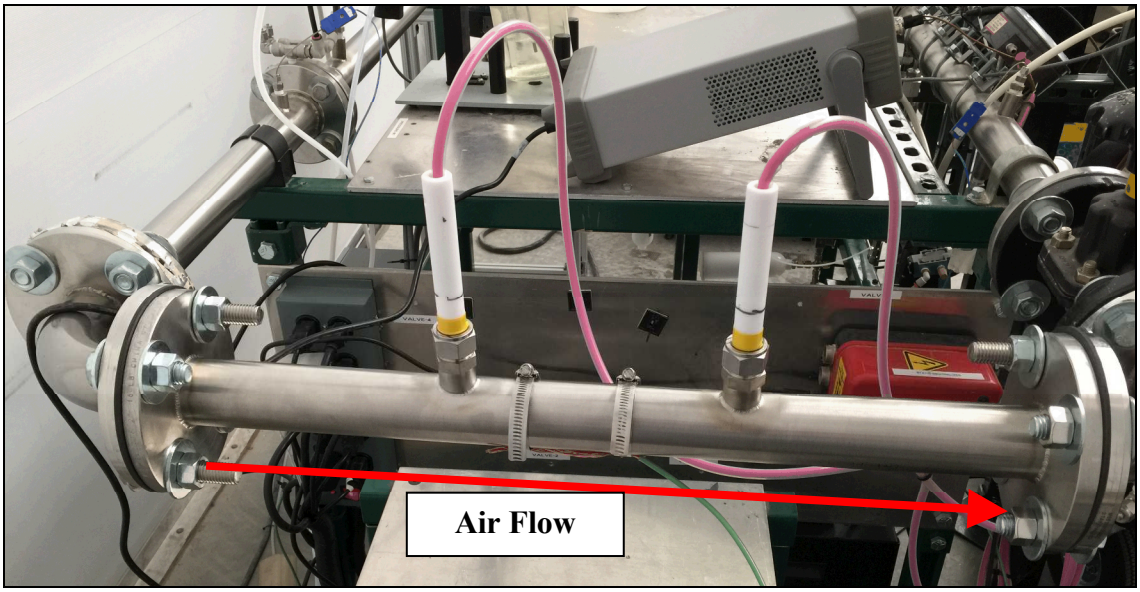

Figure 5. Particle pre-charging apparatus to impart unipolar electrical charge on aerosol particles for enhanced collection efficiency

Figure 6. Five point pinner electrostatic charging applicator used to create a corona discharge, ionize air, and charge aerosol particles

Commercial electrostatic precipitators employ the same technology implemented here (particle-pre-charging). A corona discharge is used to pre-charge aerosol particles. In an electrostatic precipitator, conducting plates are used to create an electric field. Charged particles migrate across the electric field and are collected on the plates. In the RASA, if particle-pre-charging were applied to enhance RASA sensitivity, charged particles would experience greater Coulombic attraction forces to electrostatically charged filter fibers thereby increasing particle collection efficiency.

2.1.2 Test Matrix

The test matrix to be described in this report is given below. Many preliminary tests were performed to develop the use of particle pre-charging. Our final data represents one-hundred and sixty two individual experiments. Approximately one-hundred preliminary experiments were performed before down-selecting to the conditions of the final test matrix.

1. Filter materials
    a. FM1 with S1 (front and back)
    b. FM2 with S2 scrim (front and back)
    c. FM3 with S2 scrim (front and back)
2. Filter face velocity
    a. 1.1 m/s (RASA operating point)
    b. 2.8 m/s (2.5 x RASA operating point)
    c. 5.5 m/s (5 x RASA operating point)
3. Electrostatic fiber charge
    a. charged
4. Electrostatic particle charge
    a. Boltzmann equilibrium charge distribution
    b. Positive polarity
    c. Negative polarity
5. Test aerosol
    a. Sodium chloride nanoparticles
    b. ISO test dust microparticles

2.1.3 Materials

2.1.3.1 Scrim 1 (S1)

For the RASA aerosol sampling platform, filter media is sandwiched between two layers of S1 "scrim" material. This scrim protects the filter material from mechanical devices (e.g., rollers) used to automatically move the filter material through the system. It has been suggested that the manufacturer formulated a special version of S1 with minimal titanium background. Titanium is commonly used as a whitener in fibrous materials but adversely effects radiochemical separations. S1 is shown below in Figure 7 where the fiber diameter is on the order of 25-35 µm.

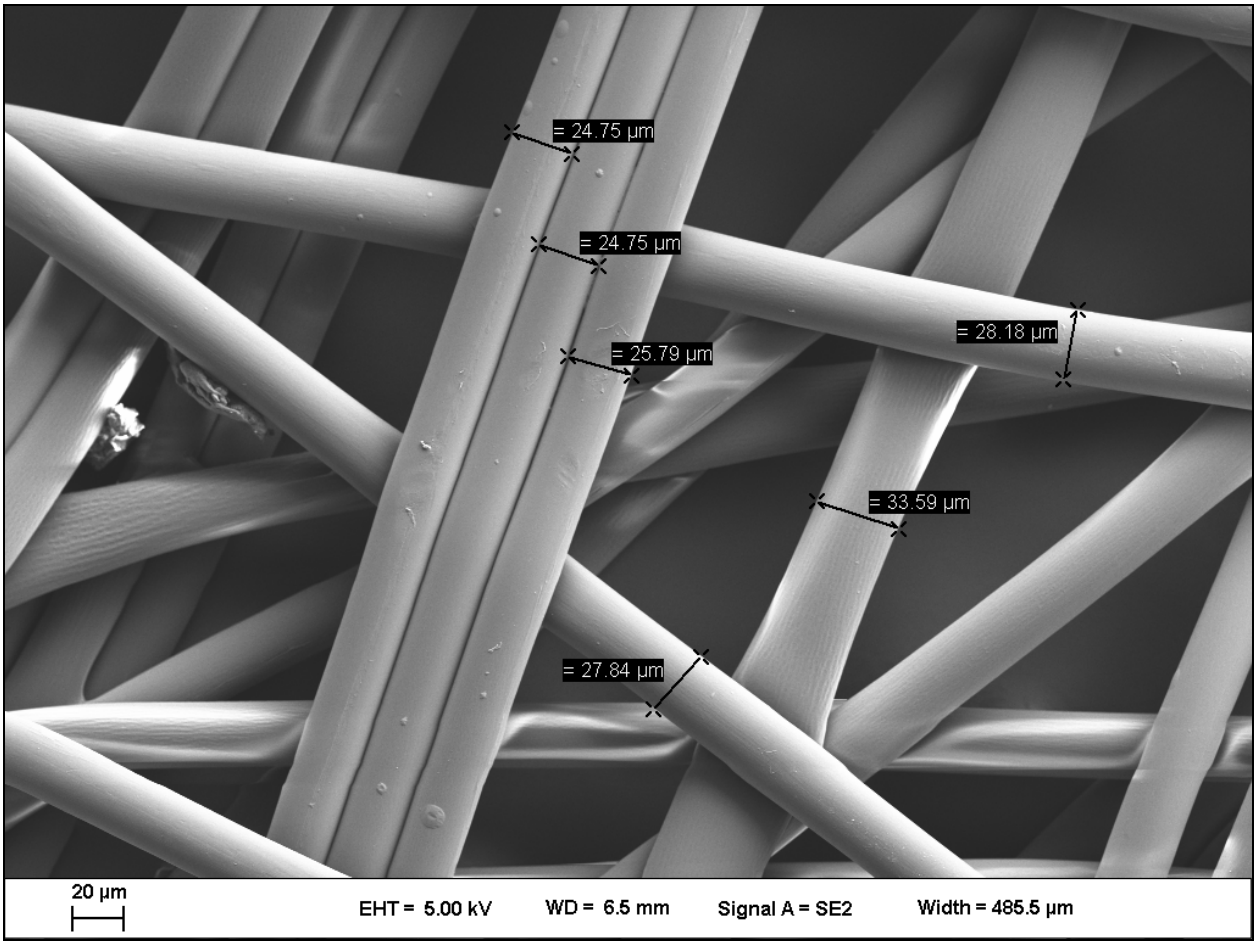

Figure 7. S1 scrim material used in current RASA filter material

2.1.3.2 Scrim 2 (S2)

Through separately funded DTRA research, SNL has identified and characterized a structural support material with lower pressure drop than S1. The material will be called S2. The manufacturer provided information regarding the composition of S2 fibers. The fibers have a polyester core with a nylon skin where the PET/PA6 ratio is approximately 75/25%. The estimated skin thickness of PA6 is 2-3 µm. Fibers are first spun and then the non-woven material is made where fibers are bonded with hot air (the lower melting PA6 acts as the 'bonding agent'). The fibers are 'fully drawn' which means the PET (and PA6) polymer chains are oriented such that fibers possess high bending stiffness. Any increase in air permeability obtainable through structural support materials should also be considered in addition to the air permeability of the filter. S2 is a dark grey color which suggests titanium may not be used during the production process to enhance its whiteness. S2 is shown below in Figure 8 where individual fibers are approximately 30-40 µm.

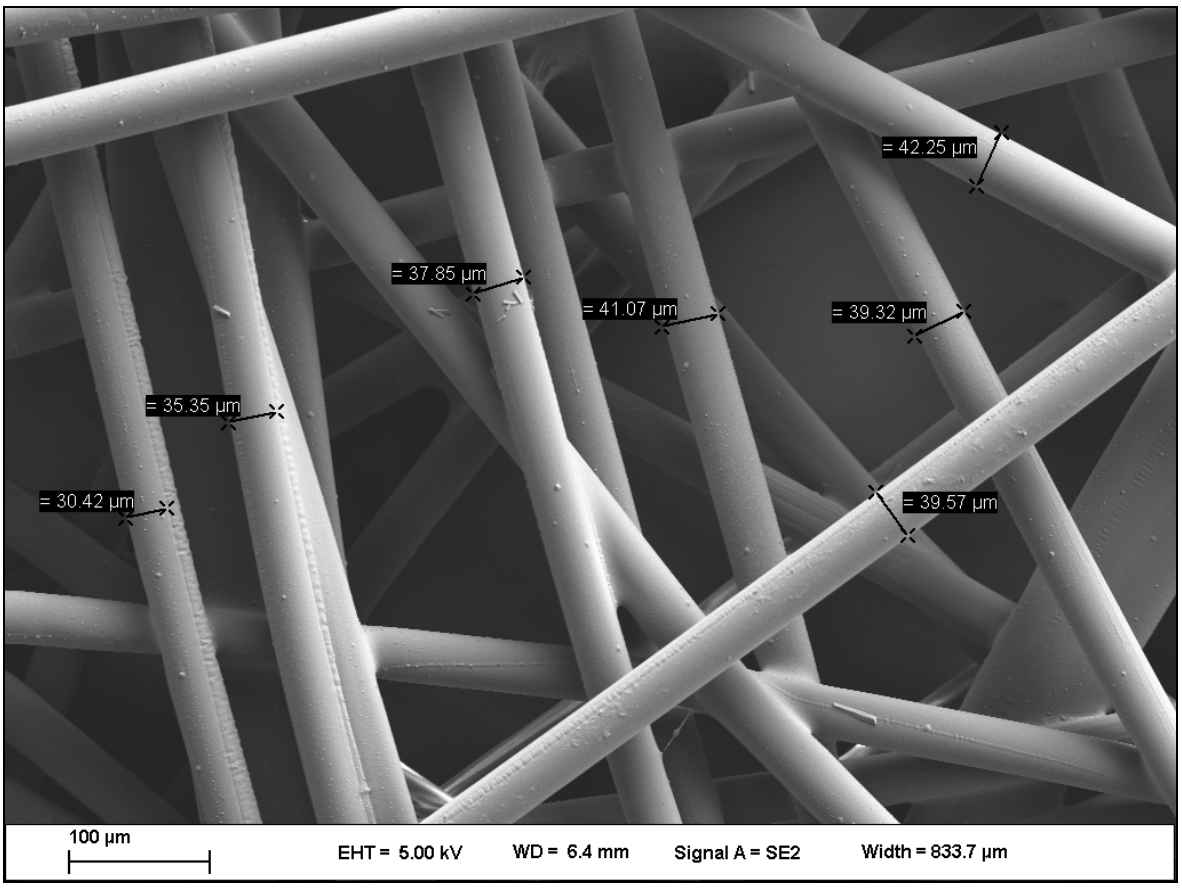

Figure 8. S2 proposed substitute scrim material with low pressure drop with respect to S1

2.1.3.3 Filter Material 1 (FM1)

As mentioned previously, FM1 has been studied extensively. Its performance can be found in the following references: Dellinger et al. (2009, 2012), Hubbard et al. (2012a, 2012b, 2013, 2014), and Sanchez et al. (2013). Scanning electron microscope (SEM) images of FM1 are shown in Figure 9 and Figure 10 where filter fibers have been used to capture ISO and NaCl test particles, respectively. The mean fiber diameter for FM1 lies in the range of 1-3 µm.

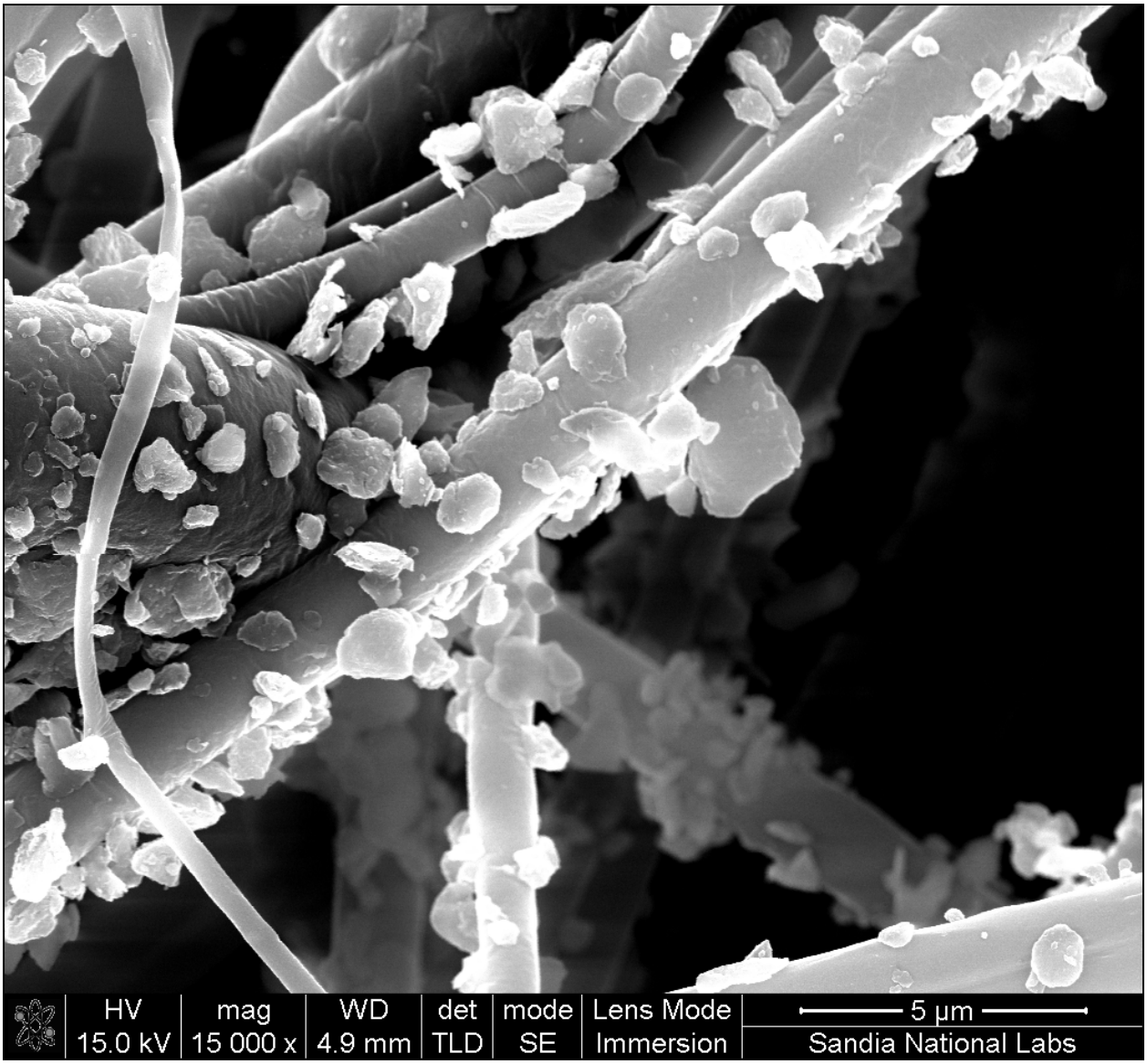

Figure 9. FM1 filter fibers coated in ISO test dust after a laboratory scale collection efficiency measurement

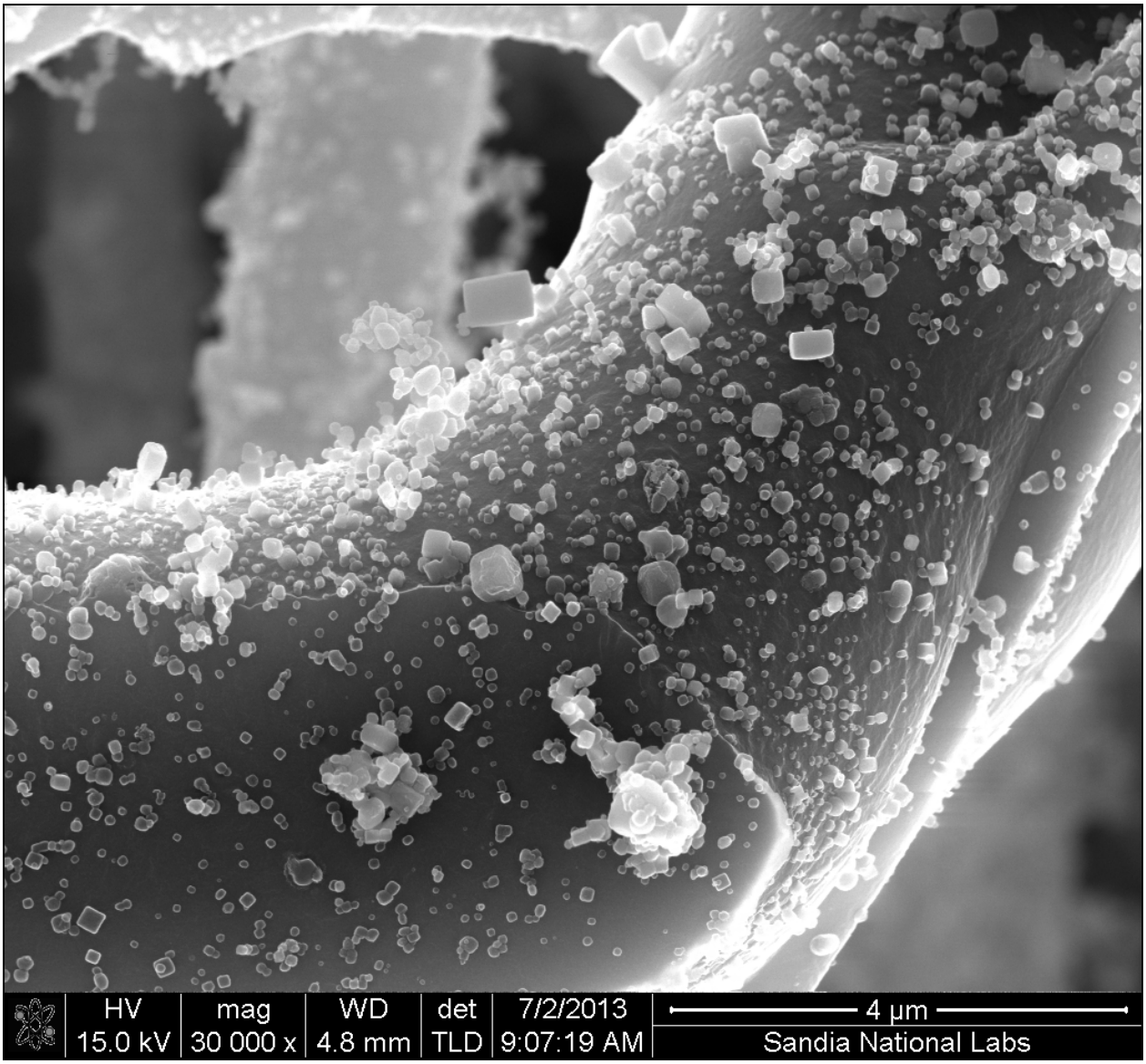

Figure 10. FM1 filter fibers coated in sodium chloride aerosol after a laboratory scale collection efficiency measurement

2.1.3.4 Filter Material 2 (FM2)

FM2 is manufactured by the same company as FM1 but the basis weight and fiber diameter ("C" for coarse fiber) give it higher air permeability. Thompson et al. (2002) provide no data for a single layer of FM2 but state that it did not meet the performance requirement of 80% efficiency at 0.2 micrometers. Thompson et al. (2002) and Valmari et al. (2000) mention the use of dioctyl-phthalate (DOP) aerosol to challenge filters. DOP is an oil droplet based technique where the challenge aerosol is liquid rather than solid. Recent SNL test data showed a single layer FM2 efficiency of approximately 90% at 5 m/s and an air pressure of 0.8 atmospheres for 200 nm particles. SNL data with solid NaCl particles contradicted data from the reports of Thompson et al. (2002) and Valmari et al. (2000). We hypothesized that DOP aerosol was less affected by particle-fiber electrostatic forces and may not have been representative of atmospheric aerosols collected by the RASA. SNL therefore proposed to reexamine FM2 to see if its performance was satisfactory for the RASA.

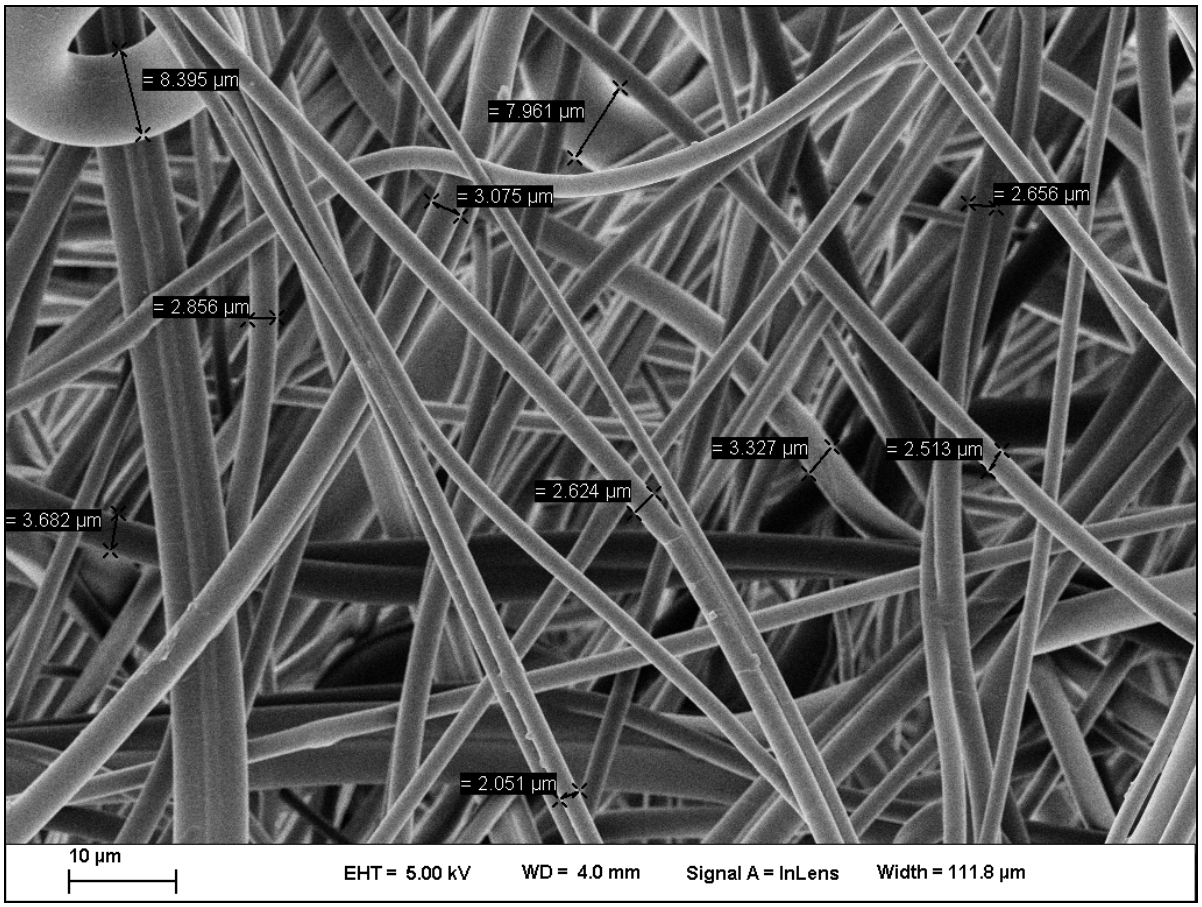

Figure 11. FM2 filter material proposed as substitute for FM1

2.1.3.5 Filter Material 3 (FM3)

Other electrostatic materials have been tested by SNL for high volume aerosol sampling. The manufacturer specification sheet for FM3 stated this non-woven electrostatic material has a collection efficiency of 87% at 0.1 micrometers. The specification sheet also gave a bipolar charge density of 50 nC/cm^2. The work of Sanchez et al. (2013) calculated the fiber charge density for FM1 as 12 nC/cm^2. Thus, we expected the electrostatic capture mechanisms to be slightly enhanced for FM3 with respect to FM1. The fibers were rectangular, approximately 10 micrometers by 40 micrometers, made of polypropylene. The filter mat came in flat sheets much like the FM1 material. SNL suggested that FM3 could be a suitable RASA filtration media due to its high air permeability and reported collection efficiency.

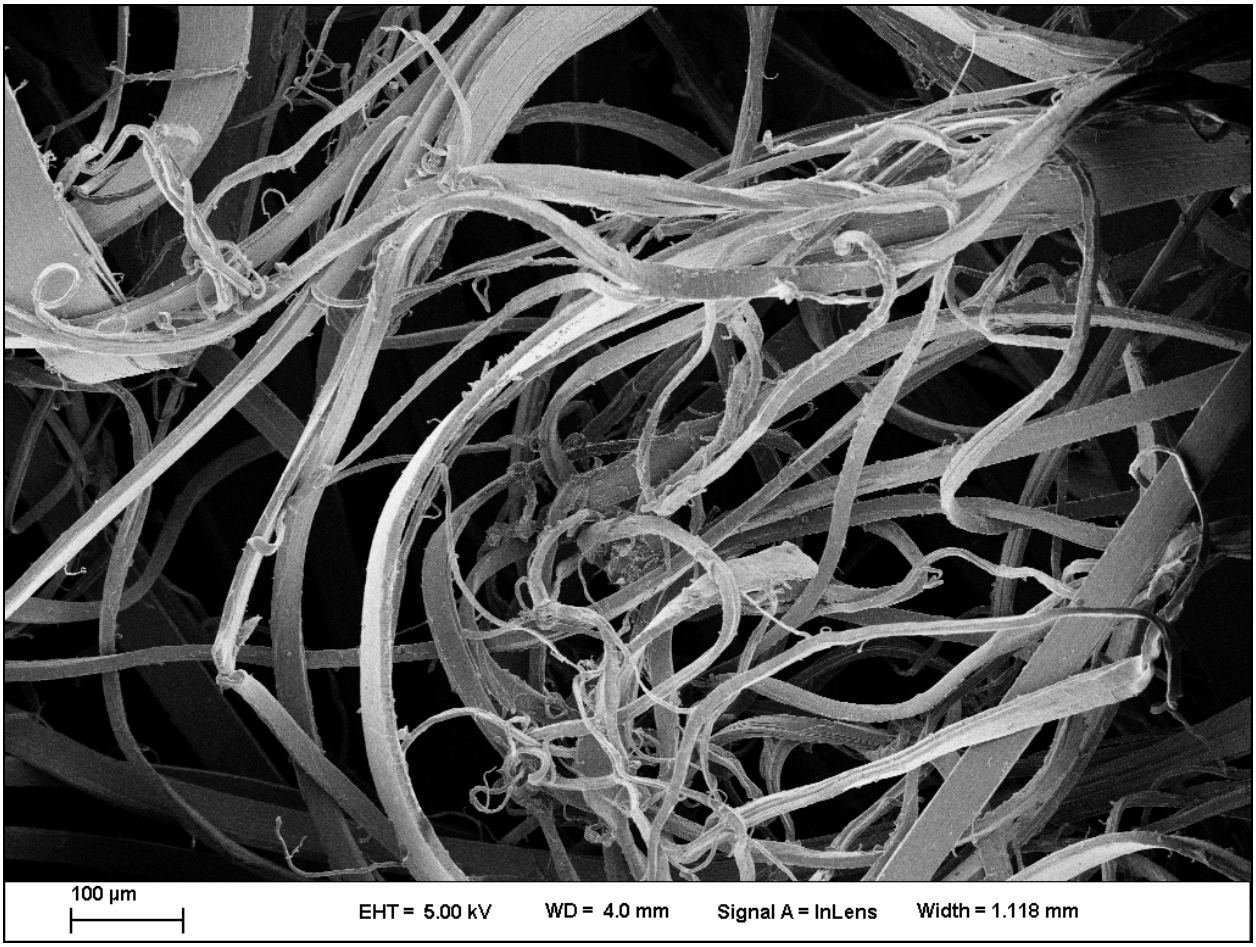

Figure 12. FM3 filter material proposed as substitute for FM1

2.2 Calculations

2.2.1 Particle Diameter Conversion

The SMPS and APS particle sizing instruments utilize different fundamental principles to size aerosol particles: electrical mobility, and aerodynamic time of flight, respectively. The SMPS size segregates particles in an electric field and then counts nanoparticles after water has been condensed on to their surfaces to the point they scatter sufficient light to be detected. The aerodynamic particle sizer accelerates particles in a nozzle and utilizes two sequential laser beams to determine the time of flight for particles having passed through the nozzle. Thus, the diameters given by each instrument are not directly comparable to those given by the other instrument. Electrical mobility diameters (d_m) given by the SMPS were converted to aerodynamic diameters (d_a) to make an accurate comparison of filter efficiency across the entire spectrum of particle sizes (30 nm to 5 μm). DeCarlo et al. review particle sizing principles and particle size equivalents (2004). The volume equivalent diameter, d_{ve}, is given by

$$d_{ve} = d_m \frac{C_c(d_{ve})}{C_c(d_m)} \cdot \frac{1}{\chi} \tag{1}$$

where χ is the particle shape factor and C_c is the particle slip correction factor use to incorporate the effects of non-continuum fluid drag on nanoparticles. The slip correction factor is easily calculated and is outlined in other seminal references on aerosol physics (Hinds 1999; Baron and Willeke 2001). The aerodynamic diameter, d_a, can then be calculated with the true particle density, ρ_p, and unit density $\rho_0 = 1000\ \text{kg/m}^3$.

$$d_a = d_{ve}\sqrt{\frac{1}{\chi}\frac{\rho_p}{\rho_o}\frac{C_c(d_{ve})}{C_c(d_a)}} \tag{2}$$

Spencer et al. give the shape factor and true density of atomized sodium chloride particles as $\chi = 1.11$ and $\rho_p = 2040\ \text{kg/m}^3$ (2007). Equations (1) and (2) were solved in MATLAB software to determine the volume equivalent and aerodynamic diameters from electrical mobility diameters given by the SMPS. The APS measures ISO test particle size in aerodynamic diameter, thus, no conversion of APS data was required.

2.2.2 Collection Efficiency

Aerosol collection efficiencies were calculated according to

$$\bar{E} = 1 - \frac{\bar{C}_d}{\bar{C}_u}\frac{\bar{P}_u}{\bar{P}_d} \tag{3}$$

where $\bar{C}_u$ was the average of three measurements of upstream aerosol concentration, $\bar{C}_d$ was the average of three measurements of downstream aerosol concentration. The ratio of upstream and downstream air pressures, $\bar{P}_u / \bar{P}_d$, was used to account for downstream flow expansion due to filter pressure drop (Lee and Liu 1982). A major pressure change across the filter causes the aerosol concentration to change even if no particles are removed from the flow.

2.2.3 Neutralizer Dead Volume Correction

Particle-pre-charging was first applied in SNL filter research during this study. A TSI 3088 Advanced Aerosol Neutralizer was placed on the inlet to the aerosol sampling piston used to extract aerosol samples from the filter test bed. In previous testing this was unnecessary since particles had little excess electrostatic charge. However, upon particle-pre-charging the aerosol upstream of the filter, electrostatic losses within the sample piston were possible for highly charged aerosol particles. For this reason we charge neutralized the aerosol particles after they had been extracted from the filter test system prior to measurement with TSI instruments.

The space charge effect is used to describe mutual repulsion of charged aerosol particles. A cloud of unipolar charged aerosol particles will create its own electric field governed by the Poisson equation. Charged aerosols then migrate across the electric field. The sample extraction piston was needed since aerosol instrumentation was not capable of pulling against vacuum present inside the filter test system. The aerosol residence time within the piston was approximately two minutes, an appreciable amount of time for particles to migrate across the electric field and deposit on the interior walls of the extraction piston before they were injected into aerosol measurement instruments. This effect is not likely to occur in the full-scale RASA since airborne particles do not reside within any specific portion of the RASA for more than a few seconds.

To mitigate measurement artifacts, we placed the neutralizer on the inlet of the piston to remove electrostatic charge from the particles prior to being measured in the APS or SMPS. By

doing so, we introduced a dead volume into the aerosol sampling system which resulted in aerosol carryover between upstream and downstream measurements. Essentially, the neutralizer was full of the upstream aerosol when a downstream aerosol was extracted. That increased the downstream aerosol concentration above its true value. Likewise, the downstream aerosol concentration was not zero, and the subsequent upstream aerosol sample was affected by the previous sample. The actual upstream and downstream aerosol concentrations are given below where variable definitions are given in Table 3.

$$\bar{C}_{u,act} = \left(\frac{V_p}{V_p - V_n}\right)\bar{C}_{u,meas} - \left(\frac{V_n}{V_p - V_n}\right)\bar{C}_{d,act} \tag{4}$$

$$\bar{C}_{d,act} = \left(\frac{V_p}{V_p - V_n}\right)\left(\frac{\bar{P}_u}{\bar{P}_d}\right)\bar{C}_{d,meas} - \left(\frac{V_n}{V_p - V_n}\right)\bar{C}_{u,act} \tag{5}$$

Table 3. Variable definitions for neutralizer dead volume corrections

$\bar{C}_{u,act}$	Actual upstream aerosol concentration (calculated)
$\bar{C}_{u,meas}$	Measured upstream aerosol concentration affected by presence of aerosol neutralizer used to eliminate electrostatic charge prior to being aspirated by the sample extraction piston
$\bar{C}_{d,act}$	Actual downstream aerosol concentration (calculated)
$\bar{C}_{d,meas}$	Measured downstream aerosol concentration affected by presence of aerosol neutralizer
V_p	Volume of sample extraction piston (2165 cm^3)
V_n	Volume of aerosol neutralizer (159 cm^3)
$\bar{P}_u$	Average air pressure upstream of the filter
$\bar{P}_d$	Average air pressure downstream of the filter after pressure drop through the filter and resultant flow expansion

The volume of the neutralizer was approximately 8% of the combined internal volumes of the piston and neutralizer. Without this dead volume correction, aerosol collection efficiencies would be systematically biased 5-10% with respect to the true collection efficiency.

2.3 Data

2.3.1 Filter Pressure Drop

The filter pressure drop is an important performance characteristic of the material. Lower air permeability (high pressure drop) materials require more powerful blowers to pull a given air flow rate through the filter. Powerful blowers consume more energy, have higher geometric footprints, and have higher acquisition cost. Low pressure drop materials were therefore desirable. Figure 13 shows the pressure drop of FM1, FM2, FM3, two layers of S2, and two layers of S1. For all data in this report, FM1 was sandwiched between two layers of S1 as it comes from the supplier. FM2 and FM3 were both sandwiched between two layers of S2 for this study. At a filter face velocity of approximately 1.1 m/s (current RASA set point), FM2 had approximately 70% of the pressure drop of FM1. For FM3, the pressure drop at 1.1 m/s was approximately 22% of the pressure drop of FM1. Pressure drop is non-linear at higher filter face velocities but these comparisons are a good illustration of the potential performance enhancements possible through the utilization of FM2 or FM3 in place of FM1.

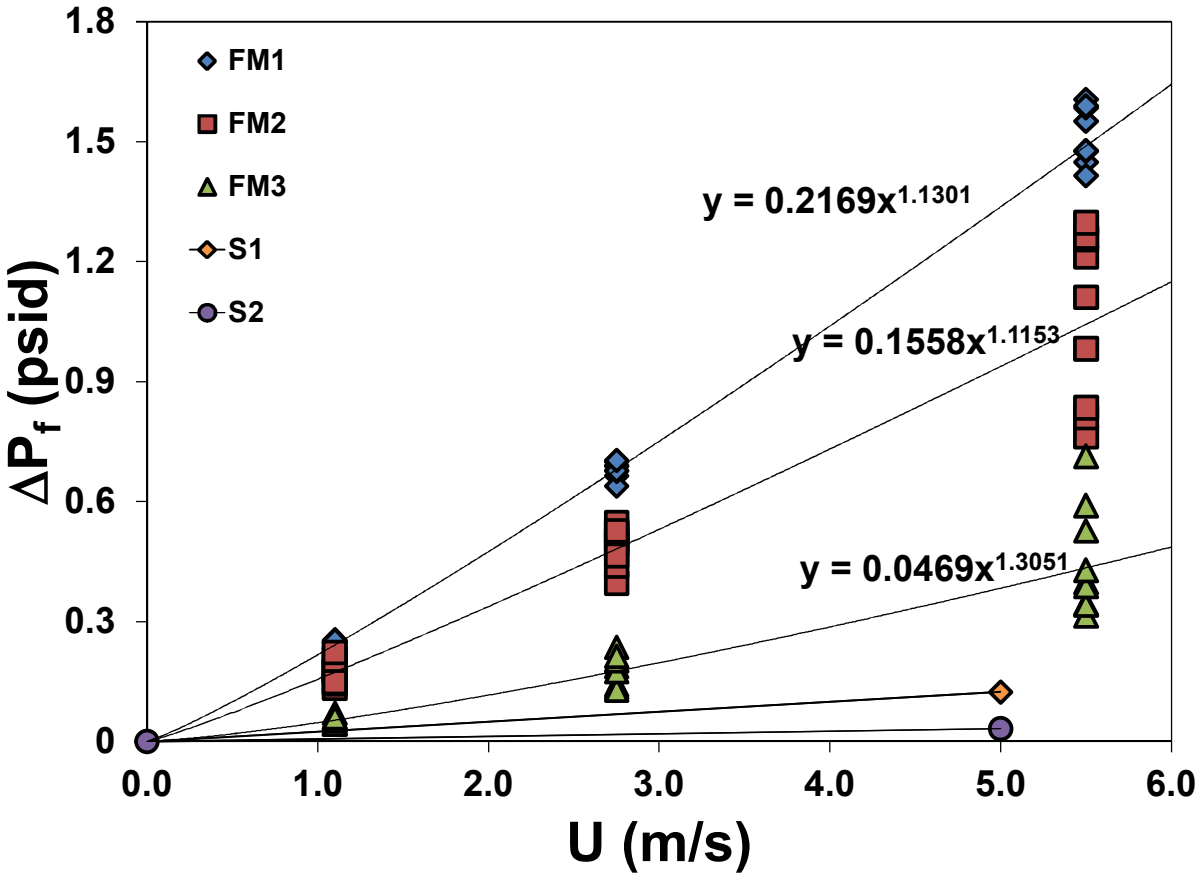

Figure 13. Filter pressure drop (ΔP_d) vs. filter face velocity (U) for FM1, FM2, FM3 and 2 layers of scrim materials S2 and S1. Filter materials FM2, and FM3 were sandwiched between two layers of S2. FM1 was sandwiched between two layers of S1.

2.3.2 Aerosol Collection Efficiency

2.3.2.1 FM1

Although FM1 has been characterized in the past, particle-pre-charging was not employed previously. For this reason, we re-characterized FM1 without particle-pre-charging so its performance with particle-pre-charging could be assessed. Data are given in Figure 14. The aerosol collection efficiency of particles between 10 nm and 100 nm improved 5-20%. There was also modest improvement for micrometer size particles although the aerosol collection efficiencies were already greater than 90-95%. Error bars are included in the figure but cannot be seen because they are smaller than figure symbols. FM1 typically displayed less than 3% standard deviation between three independent aerosol collection efficiency tests. From this figure we concluded particle-pre-charging does offer some improvement to performance with FM1 but these improvements may be marginal in light of engineering changes needed to implement particle-pre-charging in fielded RASAs.

The following nomenclature was used in aerosol collection efficiency figures:

- "qf" implies fibers were electrostatically charged,
- "qp.boltz" implies particles were in a quasi-Boltzmann charge distribution state, neutrally charged, or uncharged,
- "qp.neg" implies particles were charged in a negative corona using the particle-pre-charging apparatus shown in Figure 5,
- "qp.pos" implies particles were charged in a positive corona using the particle-pre-charging apparatus shown in Figure 5,
- "1.1, 2.75, and 5.5 m/s" were filter face velocities, and
- "0.00 and 0.25 mA" were set point currents for the ionizer power supply (voltages were adjusted internally to achieve the specified output current).

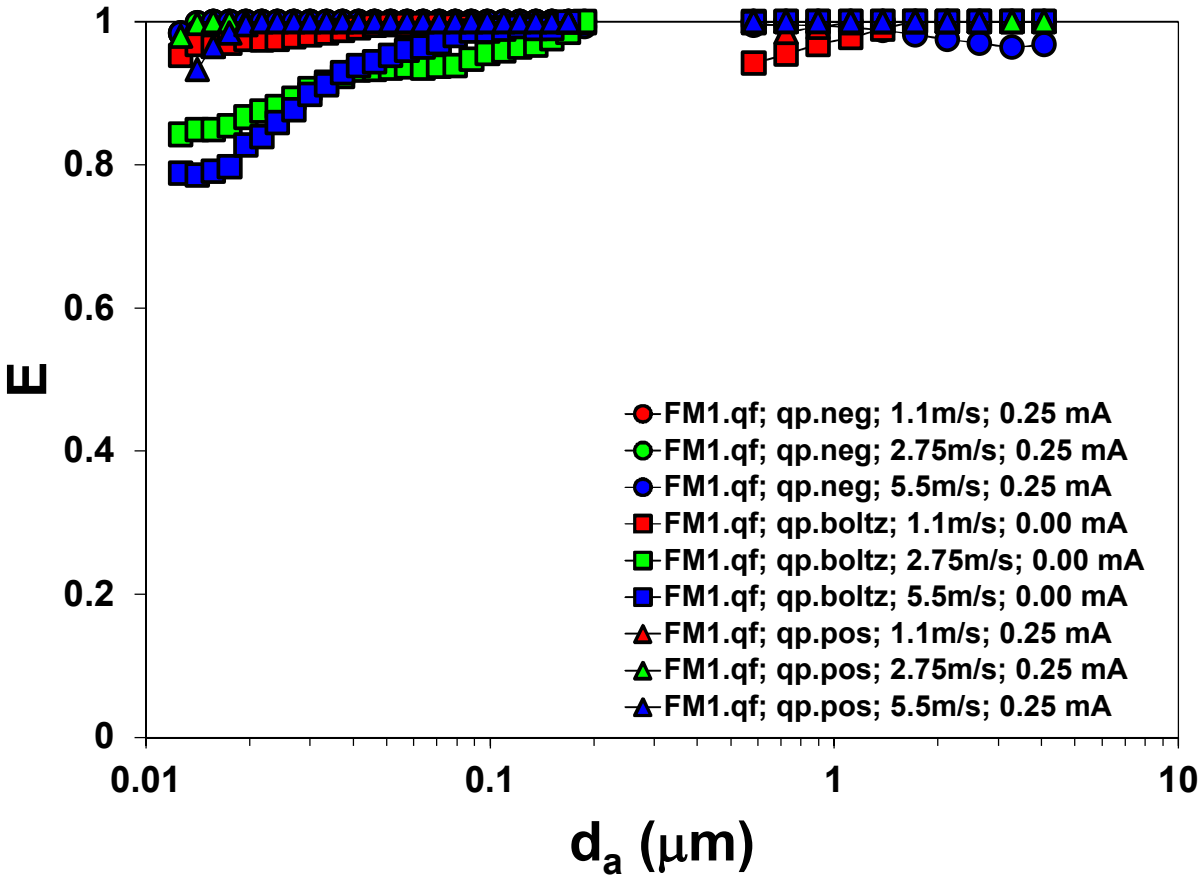

Figure 14. Aerosol collection efficiency (E) plotted against aerodynamic equivalent particle diameter (d_a) for FM1 at filter face velocities of 1.1, 2.75, and 5.5 m/s, and electrostatically charged in negative and positive coronas, and to the Boltzmann charge distribution (neutral or uncharged).

2.3.2.2 FM2

Data for FM2 are shown in Figure 15. For uncharged aerosol particles, aerosol collection efficiency decreased for small particles (< 300 nm) when the filter face velocity increased. Electrostatic capture mechanisms became less dominant with increasing filter face velocity. Performance enhancements obtainable through increased system air flow could be counteracted by lower collection efficiencies. Particle-pre-charging enhanced nanoparticle aerosol collection efficiencies (< 300 nm) to nearly 100%. Aerosol collection efficiencies were lower than RMS requirements at a filter face velocity of 5.5 m/s for particles above 1-2 micrometers in aerodynamic diameter.

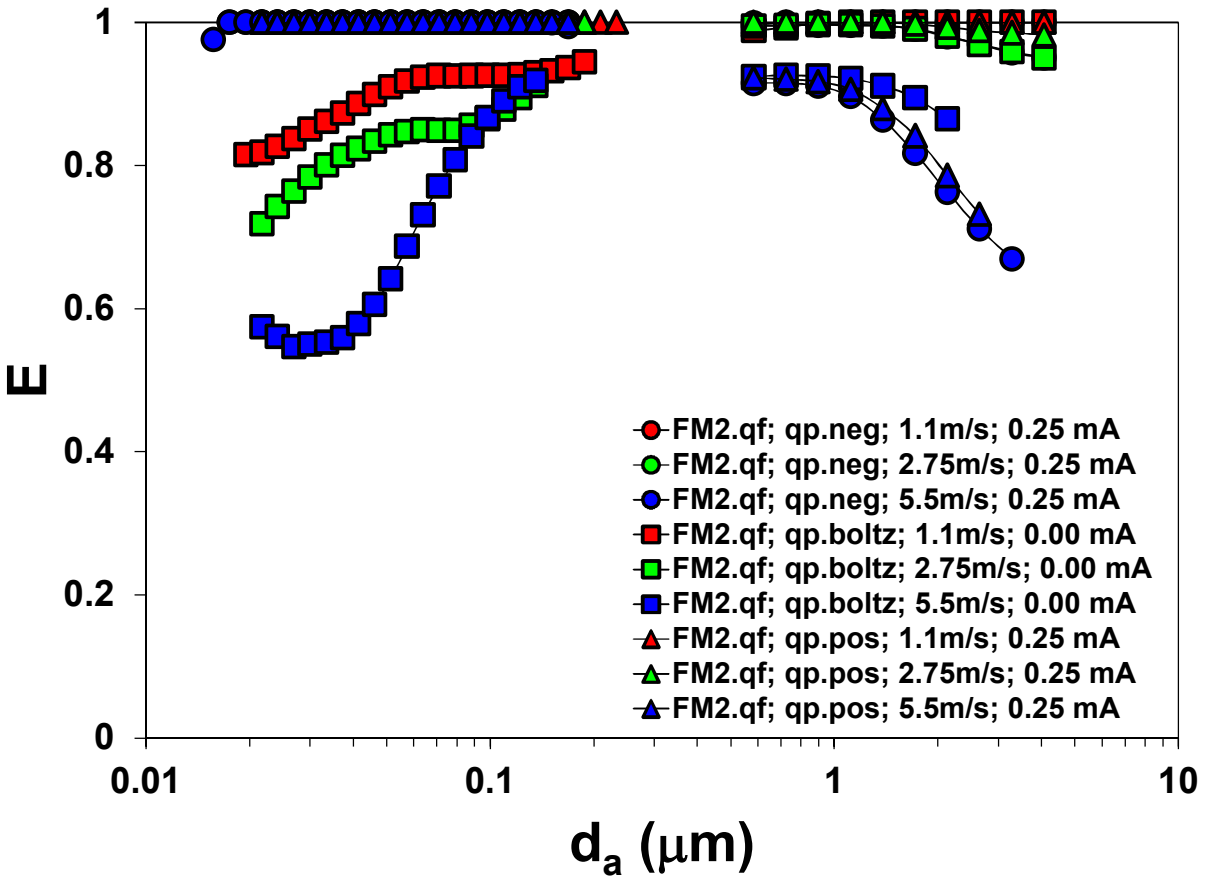

Figure 15. Aerosol collection efficiency (E) plotted against aerodynamic equivalent particle diameter (d_a) for FM2 at filter face velocities of 1.1, 2.75, and 5.5 m/s, and electrostatically charged negatively, positively, and to the Boltzmann charge distribution (neutral).

FM2 configurations with acceptable performance are shown in Figure 16. With FM2, it is possible to operate at 2.75 m/s (2.5 times the current RASA flow) and maintain acceptable performance with or without particle pre-charging. Particle-pre-charging enhances the collection of particles with aerodynamic diameters below about 300 nm.

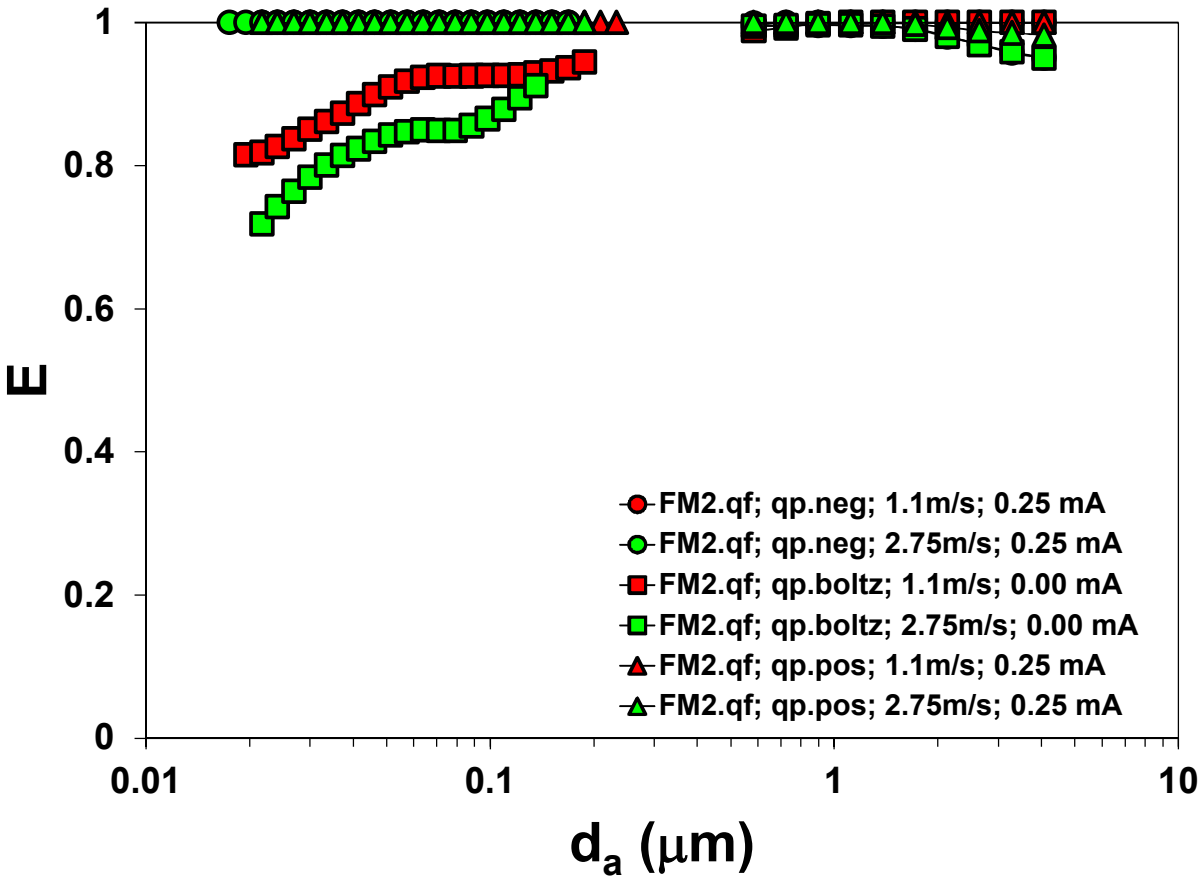

Figure 16. Aerosol collection efficiency (E) plotted against aerodynamic equivalent particle diameter (d_a) for FM2 at filter face velocities and electrostatic charge states that would satisfy CTBT requirements for RASA collections.

2.3.2.3 FM3

FM3 had high air permeability but poor aerosol collection efficiency when particle-pre-charging was not used. Without particle-pre-charging FM3 would not satisfy performance requirements for IMS radionuclide monitoring stations (80% collection efficiency at 200 nm). Figure 17 shows all data collected for FM3. Figure 18 shows down-selected data which meet IMS radionuclide monitoring station performance requirements: 1.1 m/s or 2.75 m/s with particle pre-charging from a negative corona. Collection efficiencies were higher when negative coronas were employed. This will be discussed later in the report *Discussion* section.

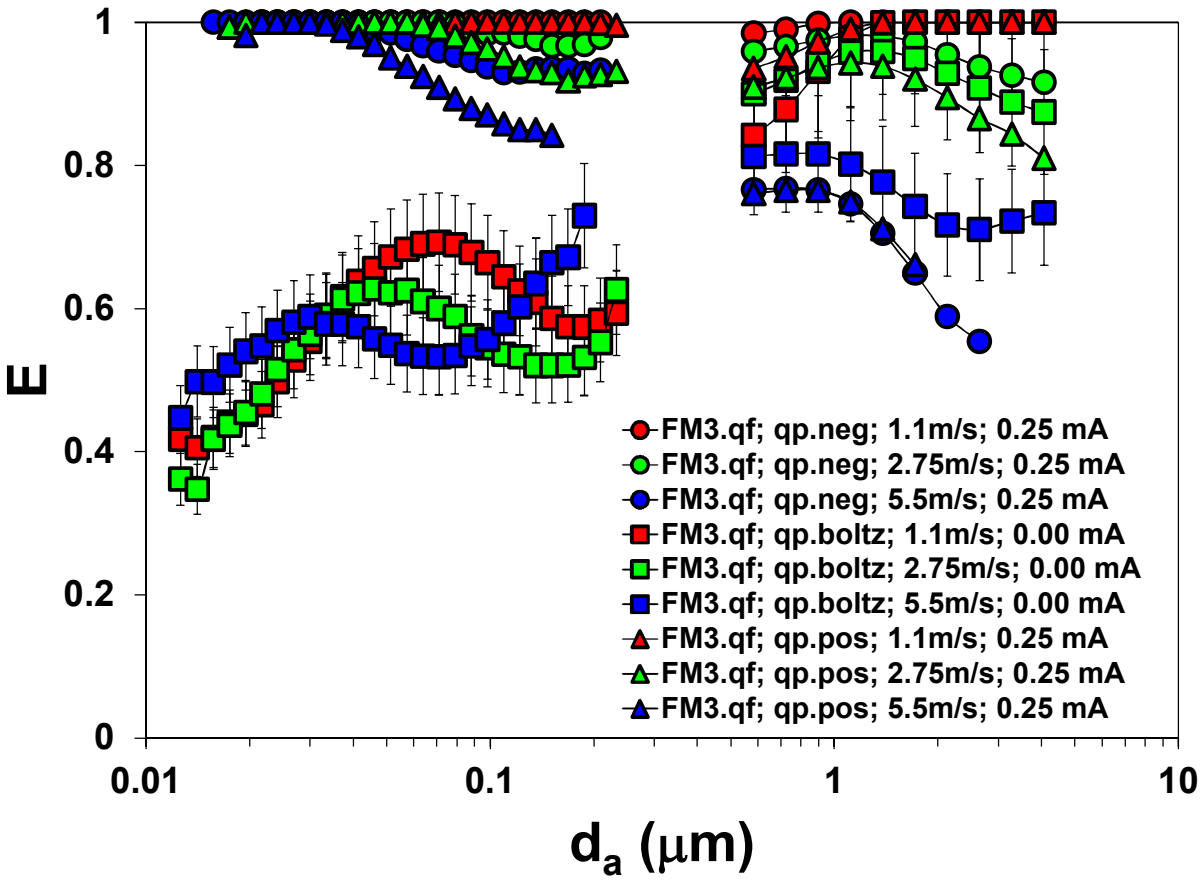

Figure 17. Aerosol collection efficiency (E) plotted against aerodynamic equivalent particle diameter (d_a) for FM3 at filter face velocities of 1.1, 2.75, and 5.5 m/s, and electrostatically charged negatively, positively, and to the Boltzmann charge distribution (neutral).

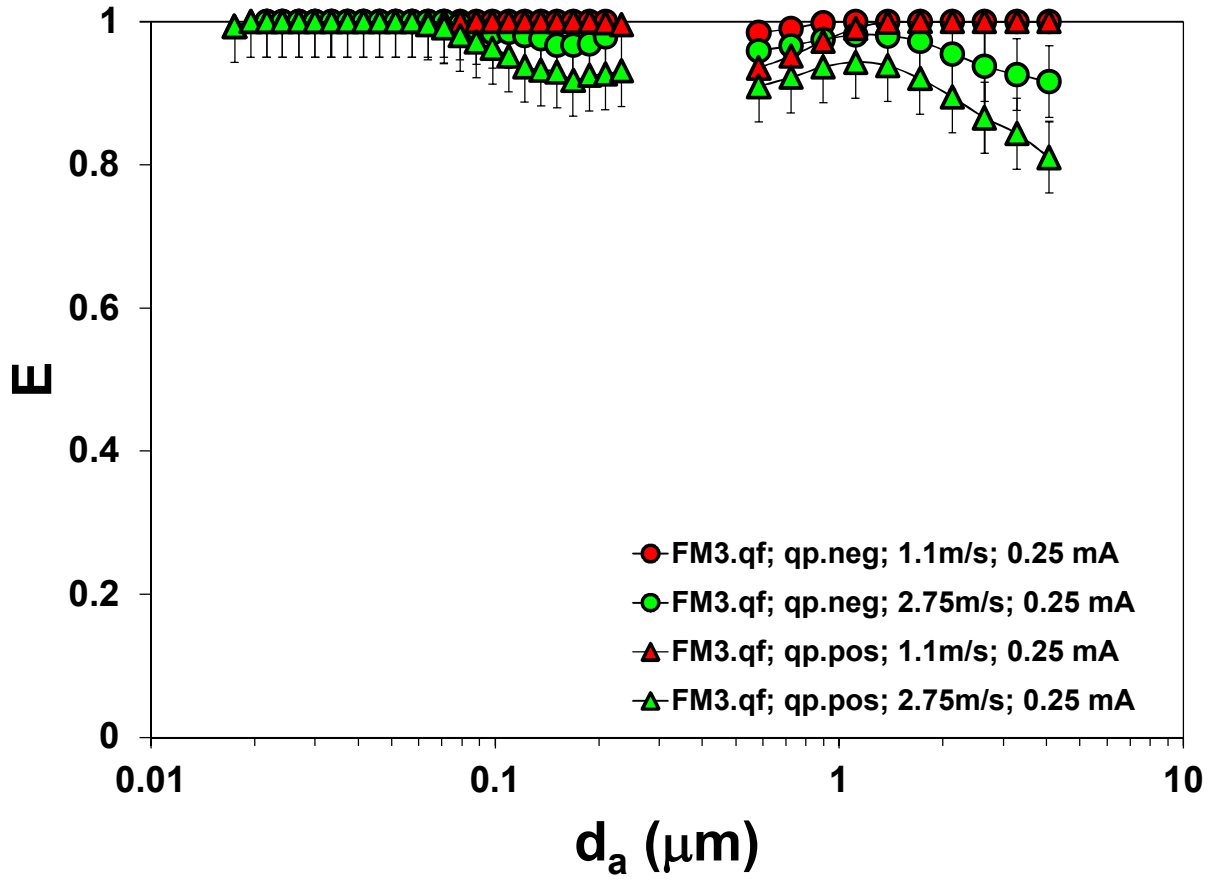

Figure 18. Aerosol collection efficiency (E) plotted against aerodynamic equivalent particle diameter (d_a) for FM3 at filter face velocities and electrostatic charge states that would satisfy CTBT requirements for RASA collections.

3 MID-SCALE FILTRATION TESTING

3.1 Background

Laboratory-scale filtration testing was described above. Challenge aerosols were generated by artificial means so collection efficiency curves could be measured for various filters and air flow rates. Mid-scale filter tests were performed were alternate methods were used to characterize filter performance. Atmospheric aerosol was used to challenge filters and radiometric methods were used to characterize the change in minimum detectable concentration for various filter materials, air flow rates, and particle-pre-charging. Mid-scale tests performed in this study utilize methodologies very similar to RASA performance certification methods specified by CTBTO. Mid-scale tests were informed by laboratory-scale tests, complement laboratory-scale test data, and inform full-scale tests.

CTBTO (2007) provides methods for certification of baseline Ba-140 sensitivities of IMS RASAs. The minimum detectable concentration is given by

$$MDC = \frac{L_D}{T \cdot V \cdot \varepsilon_E \cdot \gamma_i \cdot \xi_i} \cdot K_S \cdot K_W \cdot K_C \qquad (6)$$

where symbol definitions are given in Table 4. For the purposes of SNL mid-scale filtration testing, or quantification of relative MDC, the two most important factors were sampled air volume, V, and lower limit of detection, L_D.

Table 4. Variable definitions for equation (6), Minimum Detectable Concentration (MDC)

MDC	Minimum detectable concentration of ^{140}Ba in Bq/m^3
L_D	LD Lower limit of detection at the 95 % confidence level, L_D = 2.71+ 4.65 sqrt(μ_B)
μ_B	Standard deviation of the background at the energy of interest
T	Acquisition live time (s)
V	Sampled air volume (m^3) at STP
ε_E	Attenuation corrected efficiency (counts per gamma) at the energy of interest
γ_i	Branching ratio of gamma energy (gamma per decay) of the isotope i
ξ_i	Air sampling system global collection efficiency (%) for the isotope i. For Certification, assume a value of 1
K_S	Decay correction during sampling time assuming constant concentrations
K_W	Decay correction between end of sampling and acquisition start (decay time)
K_C	Decay correction during acquisition time

For this study, we were interested in the change in MDC if configuration changes were made to the filter material, air flow rate, or particle-pre-charging method. The relative change in MDC can be calculated with the following:

$$\frac{MDC_1}{MDC_0} = \frac{V_0}{V_1}\left[\frac{2.71 + 4.65\sqrt{\mu_{B1}}}{2.71 + 4.65\sqrt{\mu_{B0}}}\right]. \quad (7)$$

Without additional data, a reasonable assumption was that μ_{B1} / μ_{B0} scaled with V_1 / V_0. In that case, the relative MDC of configuration 1 would approximately 0.6 if the volume ratio was 1/2.5. In this calculation, the ratio of lower limits of detection would be approximately $LD_1 / LD_0 = 1.5$. Thus, the relative change in MDC from a volume change alone is not fully realized due to the change in lower limits of detection (increased background). If volume were the only factor, the relative MDC would be 0.4 by increasing the sample volume by a factor of 2.5. Mid-scale tests were conducted to measure LD_1 / LD_0 and quantify relative MDCs in representative experiments.

3.2 Aerosol Collection

3.2.1 Test Setup

A mid-scale filtration test bed was constructed to verify the relative difference in minimum detectable concentrations for various filter media at different flow rates. These experiments complemented laboratory-scale filtration tests. Ambient air was collected for 24 hours, filters were allowed to decay for 24 hours, and then the filters were counted for 24 hours on high purity germanium detectors. Four separate filters were challenged with the same ambient aerosol during a single test providing a true comparison between the filters. These tests could not be performed with full-scale RASA systems at General Dynamics since four side-by-side RASAs were not available. Our R&D approach for enhancing RASA sensitivity would also require increasing the air flow rate by a factor of 2.5. It was not feasible to make motor and electrical modifications to the full-scale RASA test systems at General Dynamics to acquire higher flow rates. Our R&D approach utilizes particle pre-charging, which could be implemented at GD but would require engineering changes to their existing systems. Performing these types of tests on the full-scale RASA at PNNL was not an option. The current electrical infrastructure of the RASA was not sufficient to provide 2.5 times higher air flow rates. At PNNL, testing would also be limited to single RASA experiments when side-by-side

comparisons were needed. SNL, therefore, designed and constructed a mid-scale filtration test system capable of bridging the gap between laboratory-scale testing and full-scale RASA testing. We called this method mid-scale filtration testing.

Aerosols were sampled from the exterior of the test facility through a 10" flexible duct. The duct was connected to a 14" diameter by 24" long custom fabricated aerosol inlet with a 14"x10" galvanized steel duct reducer. The 14" aerosol sampling inlet was needed to serve as a plenum such that separate filter samples were drawn from the same aerosol. Six ¾" bore-thru Swagelok fittings were welded on to the 14" plenum. These penetrations allowed for insertion of four particle pre-charging probes (SIMCO Ion Five Point Pinner Charging Applicator, model 4004738) and one temperature and relative humidity sensor (Omega Temperature/Humidity transmitter, 4-20 mA output, model HX86). One ¼" bore-through Swagelok fitting was welded on to the 14" plenum such that ¼" stainless steel tubing could be inserted into the plenum for aerosol sampling. The stainless steel tubing was bent at 90 degrees such that the inlet to the sampling probe was parallel to the air flow. This ensured aerosol samples were representative of the ambient aerosol and no sampling biases were introduced. The particle pre-charging probes were operated with a SIMCO Ion Chargemaster VCM Power Supply (VCM30-Bipolar) capable of positive or negative polarity coronas. Each probe was limited to approximately 250 µA output current. This corresponded to a VCM voltage of approximately 25-30 kV.

The aerosol was split into four separate air streams at the downstream end of the plenum. Each air stream passed through two inch tubing and two 90 degree bends. The air stream was then filtered with a 2.5" diameter filter specimen where only the inner 2" diameter was exposed to aerosol. Each filter specimen was held in place with a custom fabricated filter holder similar to the fixture used in laboratory-scale filter testing. Another ¼" stainless steel sampling probe was inserted upstream of each filter holder so aerosol measurements could be made throughout the duration of a mid-scale filter test. Saunders 2" diaphragm valves (050-56-21-A-11R-AA) were used to regulate the air flow through each leg of the system. These valves were identical to the valves used on the laboratory-scale test system. Lesker HEPA filter housings (PFI849KF40) were placed downstream of the diaphragm valves to capture any particulate not captured by the filters under test. This was important since laminar flow elements were used to measure the flow in each leg of the system (Merriam Laminar Flow Element 0-20 acfm, Z50MW20-150). Laminar flow elements are designed such that the air passes through a group of small capillaries.

The pressure drop across each laminar flow element was proportional to the air flow and was measured with Omega 0-10" H2O Differential Pressure Transmitter (PX653-10D5V). After the laminar flow elements, all four flow paths were merged into a single tube and connected to a 10 horsepower Travaini Rotary Vane Vacuum Pump (model PVL8300-M460) with a considerable flow capacity of 150 acfm.

A National Instruments CompactDAQ Chassis (model cDAQ-9188XT) and National Instruments Universal Analog Input modules (model 9219) were used to acquire sensor data from each of the laminar flow element differential pressure gages and the temperature/relative humidity probe. A Keithley Triple Channel DC Power Supply (model 2230-30-1) was used to supply power to each of the sensors. Data Acquisition software was written in MATLAB where a graphical user interface allowed system operators to set sensor calibration constants and set the air flows in each leg of the system.

Aerosol Measurements were made using portable instrumentation similar to the APS and SMPS. A TSI Advanced Aerosol Neutralizer (model 3088) was again placed upstream of the aerosol instruments to ensure particle charging did not bias measurements. A TSI Optical Particle Sizer (model 3330, OPS) was used to characterize particles ranging from 0.3 μm to 10 μm in 16 size channels. This instrument operates on the basis of light scattering where larger particles scatter more light. The OPS has a wide concentration range from 0 to 3,000 particles per cm^3. A TSI Nanoscan Scanning Mobility Particle Sizer (model 3910, nSMPS) was used to measure particles in the size range between 10 nm and 420 nm. The nSMPS has 13 size channels and has a working aerosol concentration range between 100-1,000,000 particles per cm^3. The nSMPS size segregates particles based on electrical mobility and uses a condensation chamber to grow particles through the condensation of isopropanol vapors onto the particle to the point at which they effectively scatter light and can be counted with lasers and optics. During 24 hour collections, one minute aerosol samples were taken from upstream of the control filter resulting in 1440 aerosol size distributions from each of the two instruments. Images of the mid-scale test filtration system are shown in Figure 19 through Figure 28.

Figure 19. 10" diameter sampling duct use to draw in ambient air to the mid-scale filter test system

Figure 19 shows the 10" sampling duct used to draw in ambient air to the mid-scale filter test system. The inlet faced north and was elevated above ground level by approximately 3 feet. The filter test system could not be placed outdoors so an inlet duct was necessary. The mid-scale filter test system was located at Sandia National Laboratories, Building 6540/Sp07.

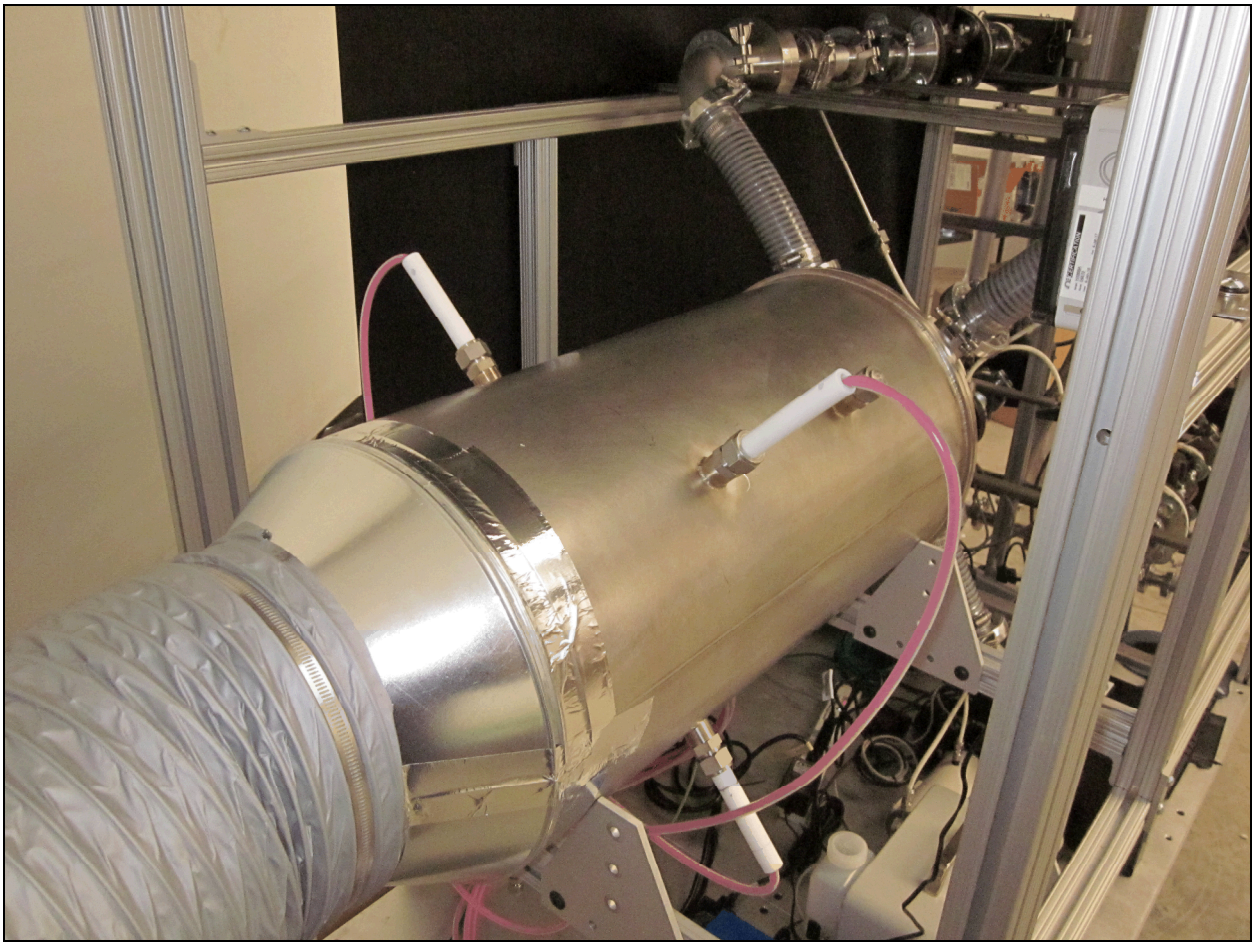

Figure 20. Sampling plenum used to pre-charge aerosol particles with unipolar ions and measure ambient aerosol concentration prior to distribution of aerosol into four separate filter sections

Figure 20 shows the aerosol sampling plenum which was stainless steel rolled into a 14" outer diameter tube. A 14"x10" duct reducer was used to mate the aerosol sampling plenum with the flexible ducting. Four ionizers were held in place at 90 degree separation with bored-thru Swagelok fittings and Teflon ferrules. For experiments where particle pre-charging was employed, the aerosol plenum was used to provide uniform charging and flow to each of the four filter specimens. The aerosol sampling plenum was electrically grounded.

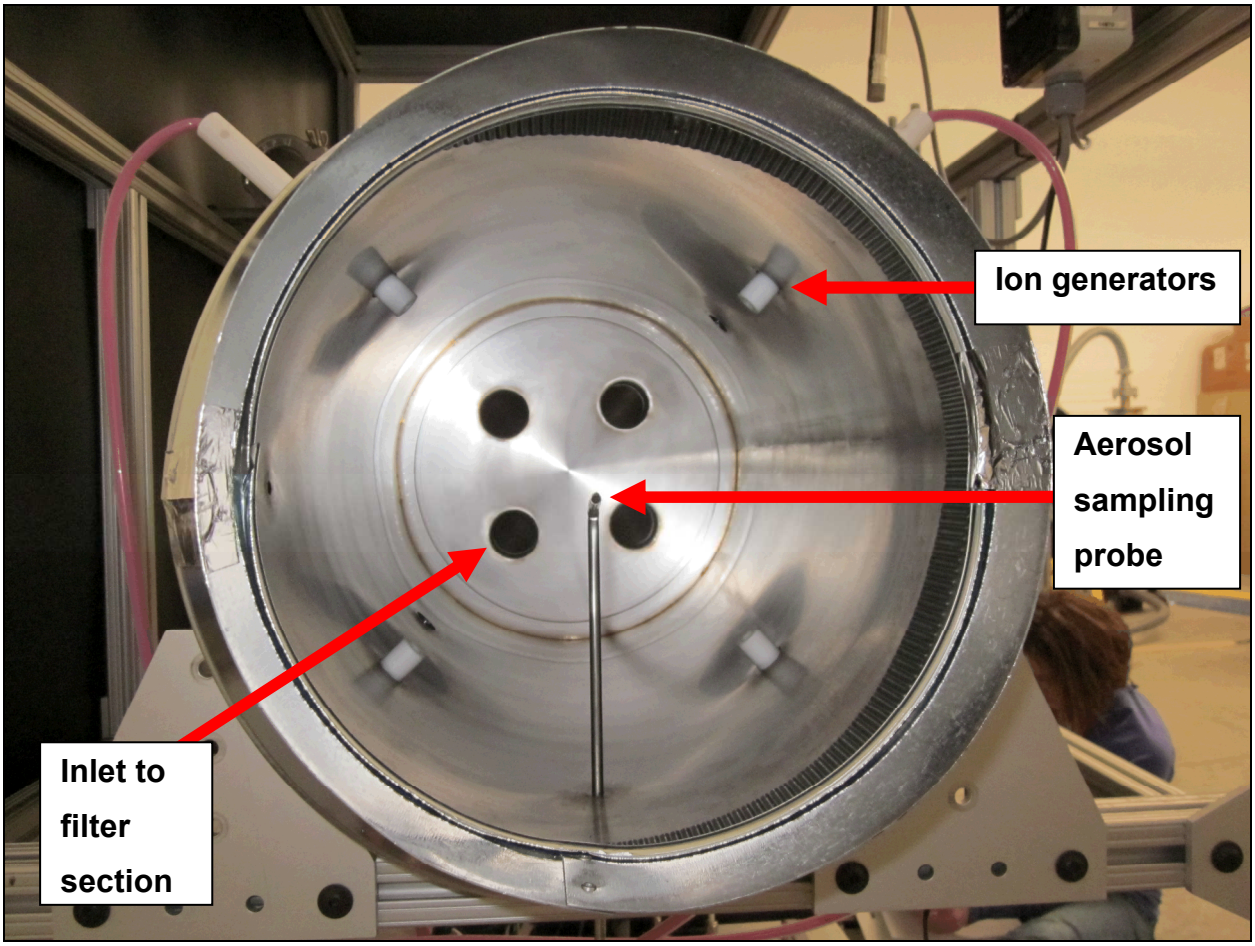

Figure 21. Interior of aerosol sampling plenum

Figure 21 shows the interior of the aerosol sampling plenum. The tips of four ion generators can be seen at 45°, 135°, 225°, and 315°. A ¼" aerosol sampling tube was placed in the aerosol sampling plenum for equipment verification testing. It was not used during experiments. The entrances to the four, independent, filter flow paths are seen at the rear of the aerosol sampling plenum. Two inch stainless steel tube fittings were welded on to a 14" flange to make the connections from the aerosol sampling plenum to the filter flow paths.

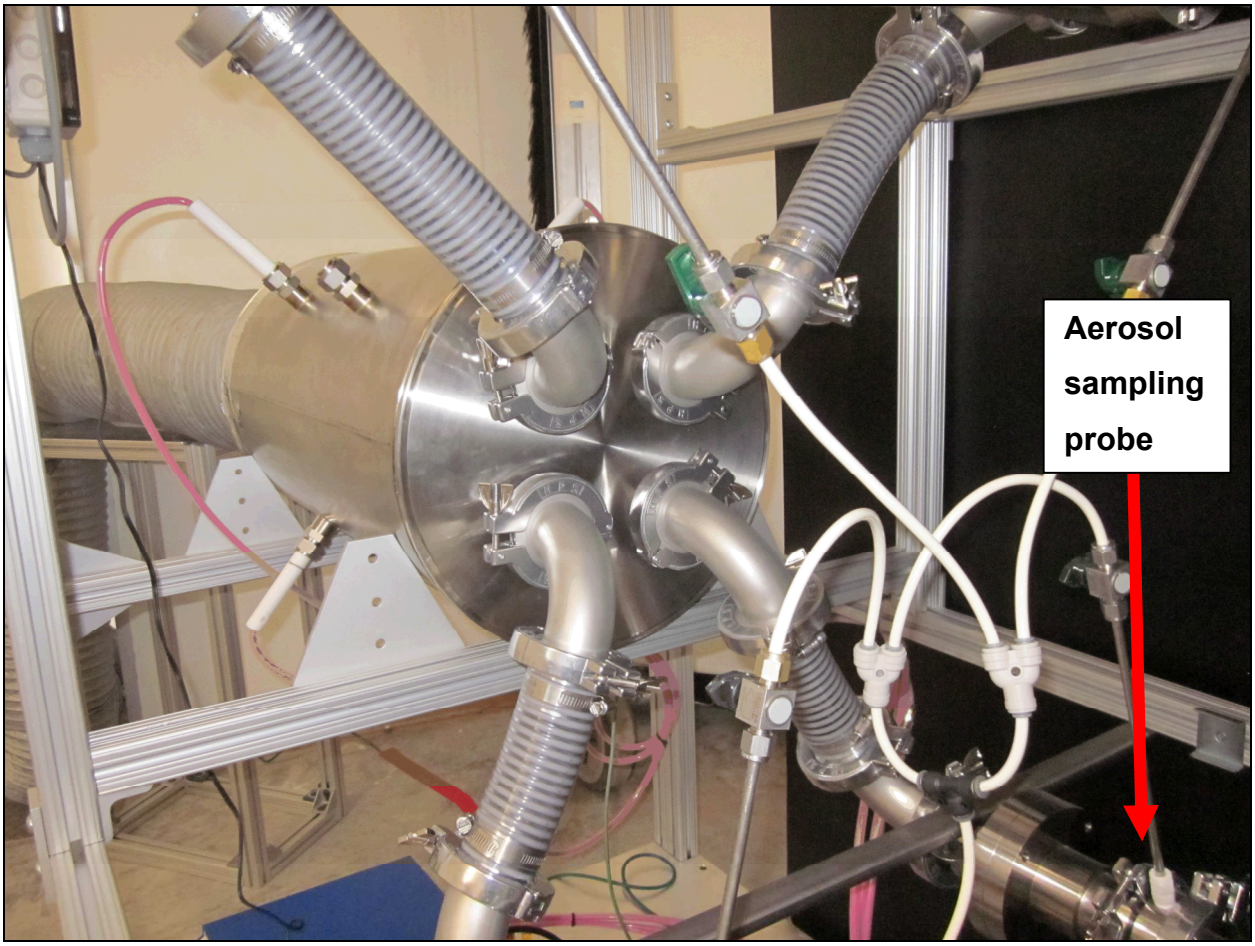

Figure 22. Exit of aerosol sampling plenum into four separate filter sampling sections of equal particle-air concentration

Figure 22 shows the rear of the aerosol sampling plenum with four independent filter flow paths. Kwik-flanges were used to assemble the majority of the mid-scale filter test system. Each filter flow path had a ¼" aerosol sampling probe upstream of the filter. This allowed for aerosol concentrations to be measured in each of the filter flow paths during experiments to verify an even distribution of aerosols was present in each flow path. Each aerosol sampling probe could be closed off from the TSI instrumentation with a ¼" ball valve (green handle in image). All four aerosol sampling lines were then merged into a single line that fed into the aerosol measurement instruments. Identical lengths of anti-static tubing were used along with exactly the same fittings so aerosol sampling losses were identical for each flow path.

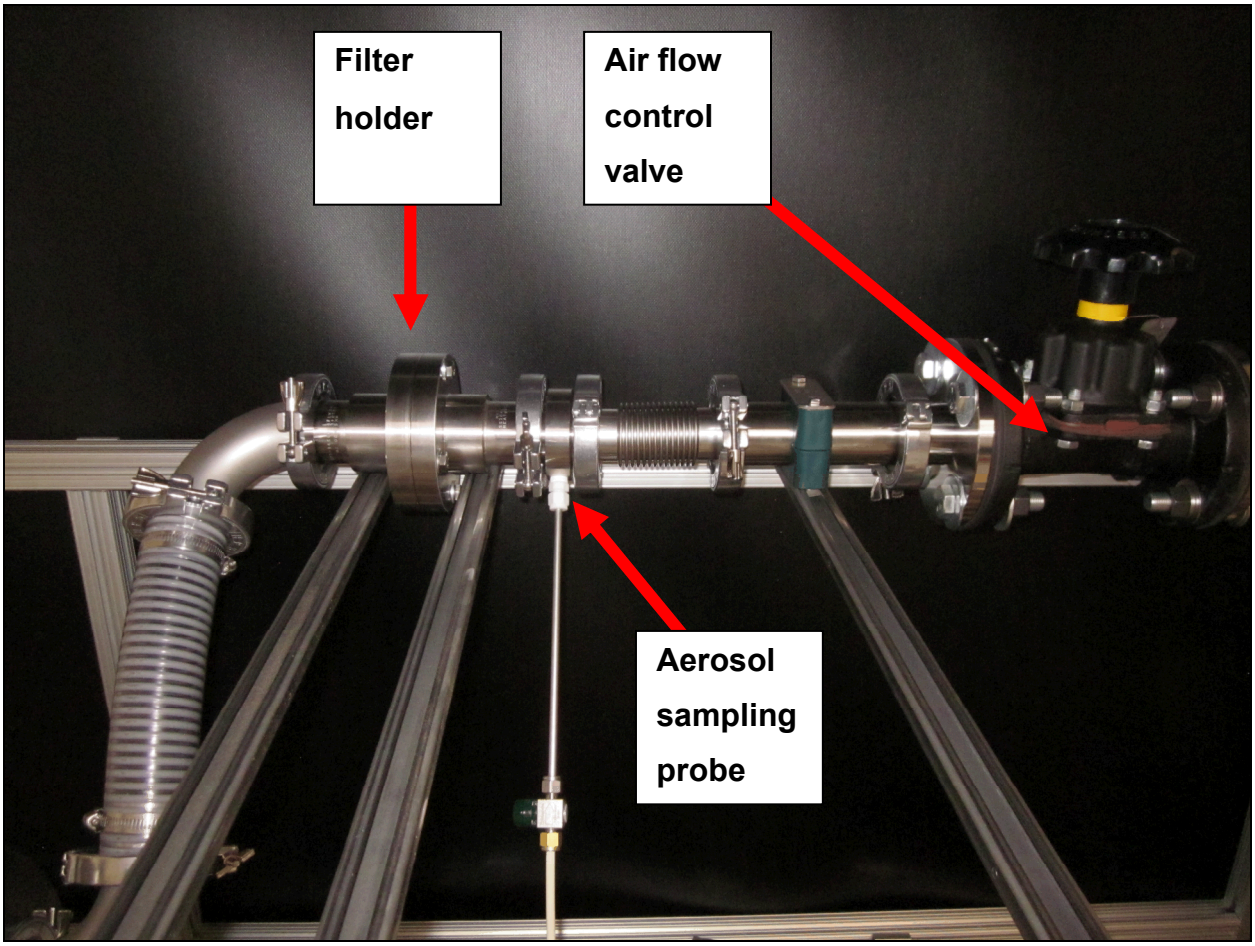

Figure 23. Individual filter sampling section with upstream aerosol sampling probe and diaphragm control valve

Figure 23 shows a single filter flow path. Aerosol sampling probes were downstream of the filter holder for mid-scale test apparatus performance verification. For experiments, the aerosol sampling probes were located upstream of the filter holder. A bellows type fitting was used to enable filter holders to be removed easily. 2" diaphragm valves were used to regulate the air flow in each filter flow path independently.

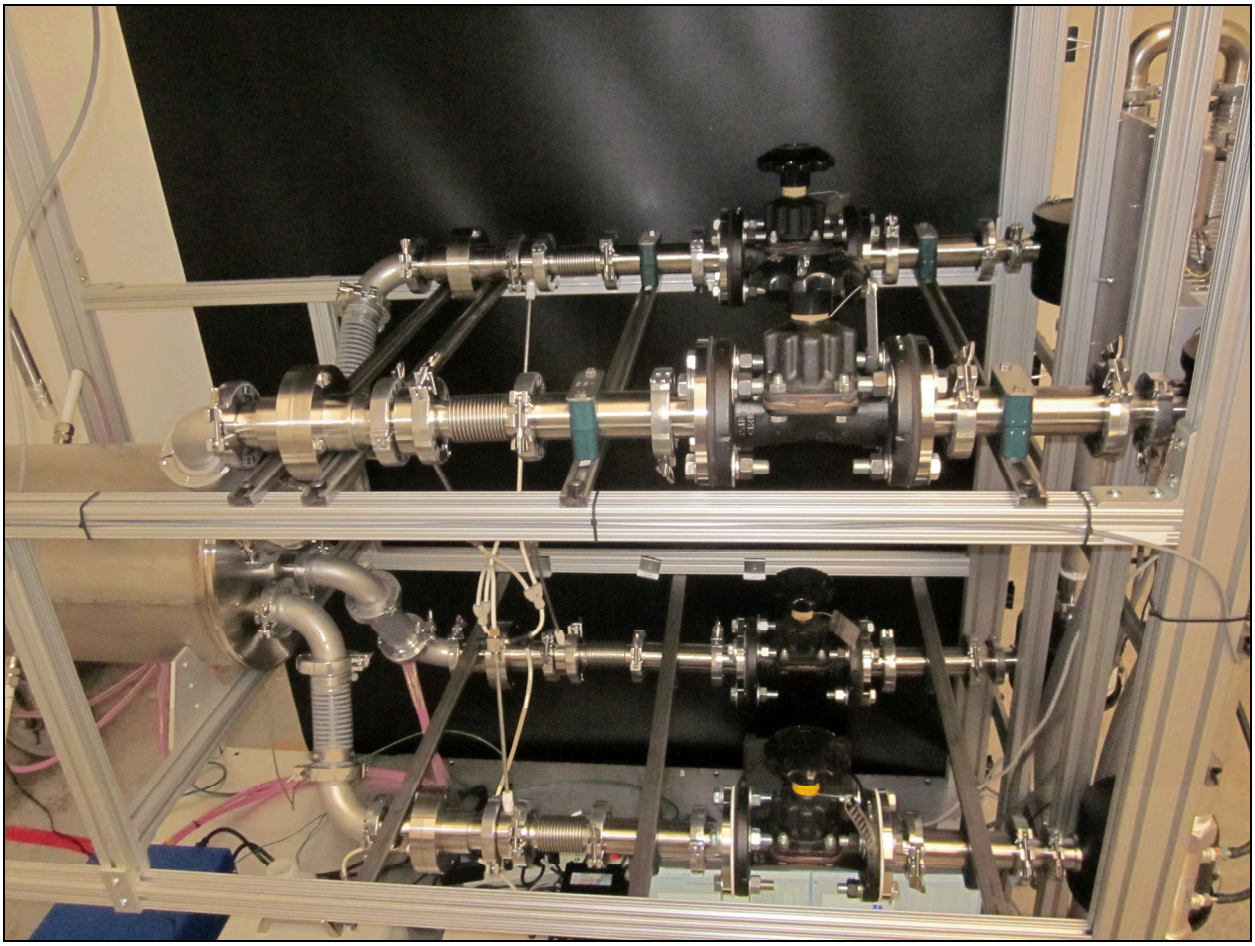

Figure 24. Mid-scale test system side-view showing aerosol sampling plenum and four separate filter sampling sections

Figure 24 shows all four filter flow paths. The system was designed so that each flow path was as close to the others as possible: bends, lengths of tubing, etc. Tubing was mounted to struts with pipe clamps (green). The entire system was mounted on a 3'x3'x6' aluminum extrusion test stand on casters.

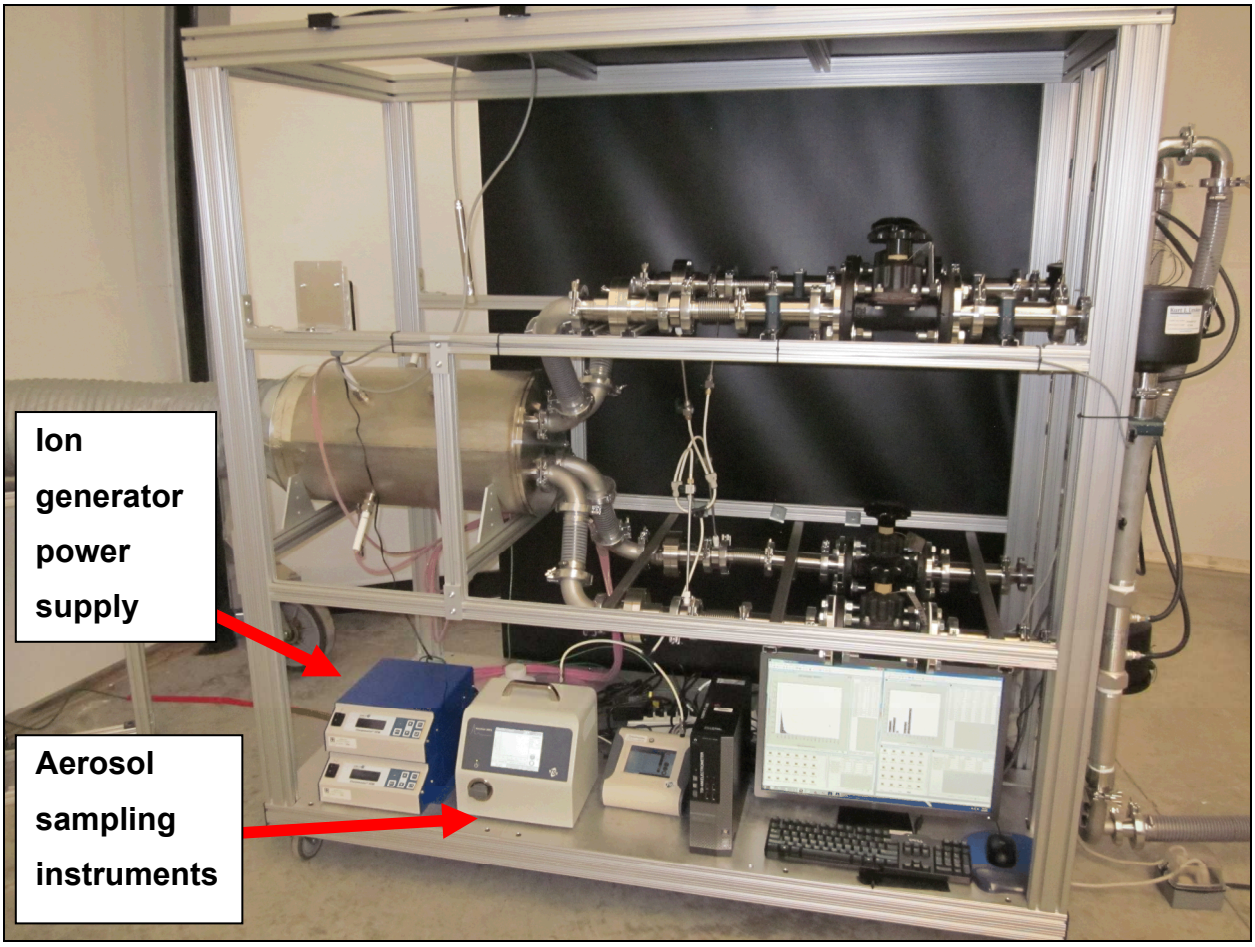

Figure 25. Mid-scale test system side-view showing aerosol sampling plenum, four separate filter sampling sections, aerosol instrumentation, data acquisition system, and power supply for ion generators

Figure 25 shows the aerosol instruments (TSI Optical Particle Sizer and TSI Nano-Scanning Mobility Particle Sizer), instrument control computer, and ion generator power supply. Figure 26 shows the vacuum plenum for the system. Air flows were HEPA filtered before being metered with laminar flow elements (LFE). If particulate passed through the filters-under-test, particulate was removed to prevent contamination of the LFEs (inaccurate measurements). All four filter flows were pulled with a single Travaini vacuum pump. Thus, all four filter flow paths terminated in the same vacuum header.

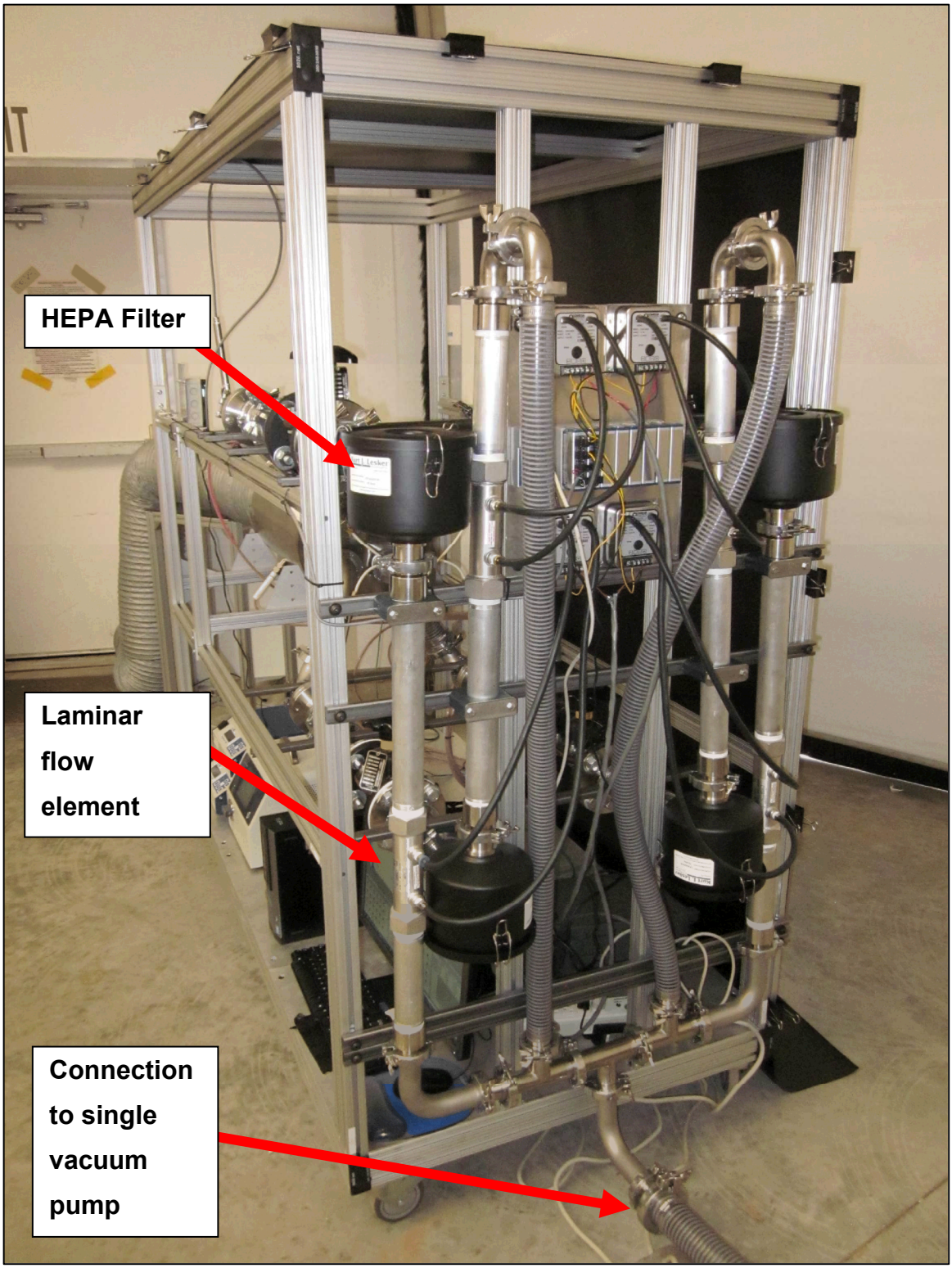

Figure 26. Mid-scale test system rear-view showing air exhaust (vacuum) plenum, laminar flow elements used to measure air flow, and HEPA filters used to clean the air stream prior to entry into the laminar flow element.

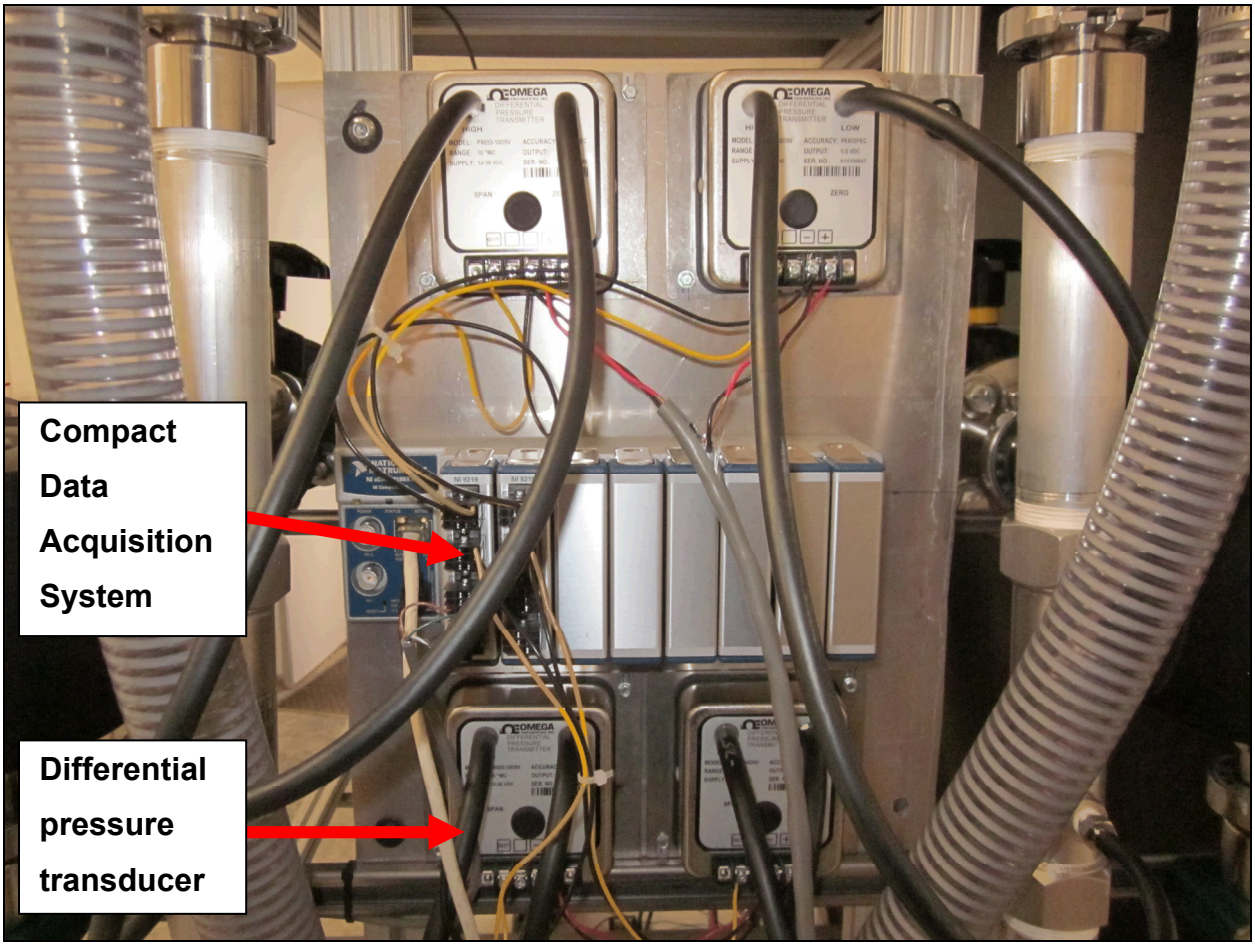

Figure 27. Data acquisition system and differential pressure transducers used to measure air flow rates in each of the filter sampling sections

Figure 27 shows the data acquisition system for the mid-scale test apparatus. Laminar Flow Elements create a pressure drop that is proportional to the flow through the LFE. Differential pressure transducers were used to measure the pressure drop across each LFE. A National Instruments Compact Data Acquisition system and Universal Analog Input cards were used to measure the voltage response from each differential pressure transducer. MATLAB software was developed to read, convert, display, and log flow data for each flow path. MATLAB software also logged temperature and relative humidity data. Flows were set independently for each flow path in a single experiment and metered throughout the 24 hour sampling period.

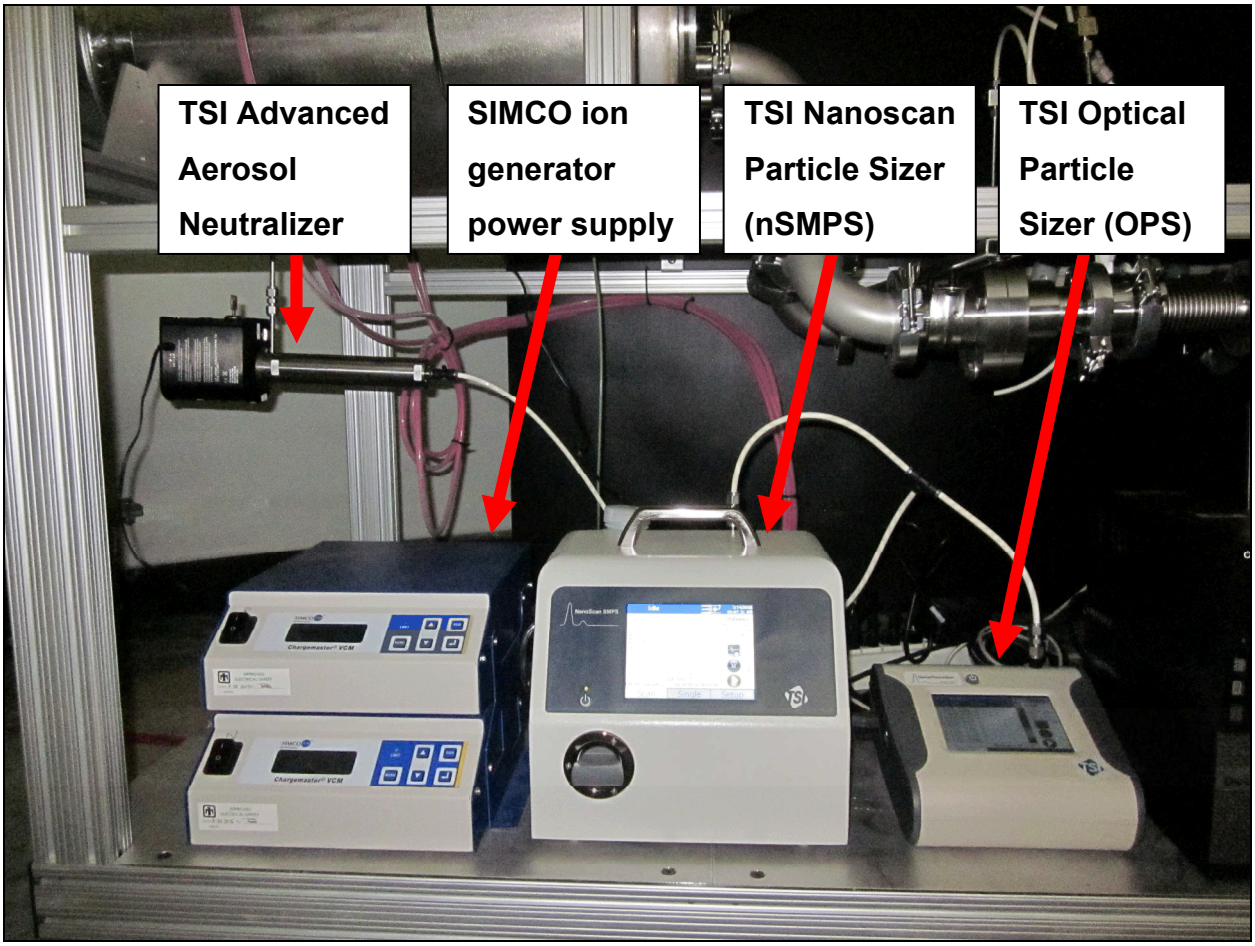

Figure 28. Aerosol instrumentation used to size and count aerosol particles in air stream and ion generator power supply used to pre-charge aerosol particles

Figure 28 shows the aerosol measurement instruments used to log particle size and number concentrations for ambient aerosol. Aerosols were electrostatically charge neutralized before entering the aerosol measurement instruments. This was particularly necessary when particle-pre-charging was employed. The TSI Advanced Aerosol Neutralizer can be seen in the figure. The TSI nSMPS and OPS can also be seen.

3.2.2 Mid-scale test system performance validation

One of the key assumptions of mid-scale filtration testing was that each aerosol filter specimen was exposed to the same aerosol throughout the 24 hour sampling period. To test the validity of this assumption, aerosol samples were taken from each flow path, upstream of filter specimens, at the beginning of each experiment. Five aerosol samples were taken sequentially in a single filter flow path so they could be averaged. The aerosol sampling line was then switched over to the next filter flow path. The start of the next set of aerosol samples was delayed by two minutes to clear out any residual aerosol from the previous set of samples. For all four flow paths, this resulted in an approximate time period of 7 minutes for an individual flow path, and 30 minutes for the entire system. The springtime is particularly windy in Albuquerque and the majority of tests began from 0800 to 1200 when the wind picks up considerably. For several experiments, the aerosol concentrations in all four legs were within a few percent, giving good confidence that there were no flow effects that would have resulted in unequal aerosol concentrations in each filter flow path. For the other tests, differences of up to 10-20% were observed. We attributed this to temporal variability in wind and aerosol concentration. In other words, we suspect the wind and aerosol concentration varied over a timescale of 10 minutes, or so, and made it appear there were unequal aerosol concentrations in the four independent filter flow paths. We think this was an artifact of having to sample each leg sequentially over a time period of 30 minutes. Aerosol concentrations would have been equal for all four filter flow paths had we been able to sample aerosols simultaneously from all four filter flow paths. We concluded that the assumption of equal aerosol concentrations in all four filter flow paths was justifiable through mid-scale test bed verification data. Table 5 shows the beginning sample time and date, the initial and final air flow rate, and total volume of air collected for each filter sample. We did not control air flows in real-time, thus, some drift occurred over 24 hours. A drop in air flow in one path often resulted in an increase in flow in another. This was attributable to the use of a single vacuum source to pull all filter flows. Three pre-trials were conducted for the normalization of HPGe detectors (0,00, and 000). Twelve trials were conducted to quantify the relative change in MDC for different filter and flow configurations (1-12).

3.2.3 Data

Table 5. Beginning and end air flow rates (Q) for each filter sample and trial

	Trial	0	00	000	1	3
Date	units	3/14/16 8:53 AM	3/15/16 9:59 AM	3/21/16 7:47 AM	3/22/16 9:12 AM	3/23/16 11:09 AM
$Q_{start,1}$	(ft^3 min^{-1})	3.74	3.81	3.86	3.76	3.83
$Q_{end,1}$	(ft^3 min^{-1})	3.55	3.68	3.70	3.92	3.83
V_1	(ft^3)	5247.9	5394.5	5443.6	5529.6	5515.2
$Q_{start,2}$	(ft^3 min^{-1})	3.77	3.83	3.85	9.59	9.55
$Q_{end,2}$	(ft^3 min^{-1})	3.59	3.73	3.76	6.98	9.12
V2	(ft^3)	5298.5	5441.5	5478.2	11930.4	13442.4
V_2/V_1	(-)	1.01	1.01	1.01	2.16	2.44
$Q_{start,3}$	(ft^3 min^{-1})	3.76	3.80	3.86	3.75	3.83
$Q_{end,3}$	(ft^3 min^{-1})	3.60	3.71	3.71	4.63	3.93
V_3	(ft^3)	5301.4	5407.7	5451.1	6033.6	5587.2
V_3/V_1	(-)	1.01	1.00	1.00	1.09	1.01
$Q_{start,4}$	(ft^3 min^{-1})	3.77	3.83	3.86	3.78	3.83
$Q_{end,4}$	(ft^3 min^{-1})	3.73	3.71	3.72	4.73	3.96
V4	(ft^3)	5398.6	5428.3	5455.2	6127.2	5608.8
V_4/V_1	(-)	1.03	1.01	1.00	1.11	1.02

	Trial	2	4	5	7	9
Date	units	3/28/16 8:07 AM	3/29/16 9:49 AM	3/30/16 11:11 AM	4/4/16 8:48 AM	4/5/16 10:03 AM
$Q_{start,1}$	(ft^3 min^{-1})	3.79	3.89	3.83	3.82	3.82
$Q_{end,1}$	(ft^3 min^{-1})	3.93	4.25	3.78	3.66	3.95
V_1	(ft^3)	5558.4	5860.8	5479.2	5385.6	5594.4
$Q_{start,2}$	(ft^3 min^{-1})	9.61	9.63	9.57	9.60	9.64
$Q_{end,2}$	(ft^3 min^{-1})	9.65	9.15	9.25	9.04	9.52
V2	(ft^3)	13867.2	13521.6	13550.4	13420.8	13795.2
V_2/V_1	(-)	2.49	2.31	2.47	2.49	2.47
$Q_{start,3}$	(ft^3 min^{-1})	9.55	9.55	3.87	3.88	3.82
$Q_{end,3}$	(ft^3 min^{-1})	9.47	8.83	3.81	3.76	4.00
V_3	(ft^3)	13694.4	13233.6	5529.6	5500.8	5630.4
V_3/V_1	(-)	2.46	2.26	1.01	1.02	1.01
$Q_{start,4}$	(ft^3 min^{-1})	3.79	3.85	3.87	3.86	3.85
$Q_{end,4}$	(ft^3 min^{-1})	3.99	4.26	3.83	3.72	3.98
V4	(ft^3)	5601.6	5839.2	5544.0	5457.6	5637.6
V_4/V_1	(-)	1.01	1.00	1.01	1.01	1.01

	Trial	6	8	10	11	12
Date	units	4/6/16 11:26 AM	4/11/16 7:58 AM	4/12/16 9:14 AM	4/13/16 10:51 AM	4/18/16 9:23 AM
$Q_{start,1}$	($ft^3\ min^{-1}$)	3.86	3.84	3.82	3.87	3.83
$Q_{end,1}$	($ft^3\ min^{-1}$)	4.12	3.87	3.88	3.80	3.82
V_1	(ft^3)	5745.6	5551.2	5544.0	5522.4	5508.0
$Q_{start,2}$	($ft^3\ min^{-1}$)	9.68	9.61	9.63	9.69	9.67
$Q_{end,2}$	($ft^3\ min^{-1}$)	10.27	9.37	9.66	9.66	9.66
V2	(ft^3)	14364.0	13665.6	13888.8	13932.0	13917.6
V_2/V_1	(-)	2.50	2.46	2.51	2.52	2.53
$Q_{start,3}$	($ft^3\ min^{-1}$)	9.68	9.61	9.63	9.68	3.82
$Q_{end,3}$	($ft^3\ min^{-1}$)	10.41	9.68	9.75	9.66	3.87
V_3	(ft^3)	14464.8	13888.8	13953.6	13924.8	5536.8
V_3/V_1	(-)	2.52	2.50	2.52	2.52	1.01
$Q_{start,4}$	($ft^3\ min^{-1}$)	3.82	3.87	3.83	3.84	3.85
$Q_{end,4}$	($ft^3\ min^{-1}$)	4.08	3.95	3.92	3.81	3.86
V4	(ft^3)	5688.0	5630.4	5580.0	5508.0	5551.2
V_4/V_1	(-)	0.99	1.01	1.01	1.00	1.01

Table 6 provides a set of test configurations used in trials 1-12. Each filter flow path was configured for a specific filter media, air flow rate, and particle pre-charging condition. Table 7 gives the specific configurations used in each trial. Note that all legs were exposed to the same particle charge condition: uncharged or charged. Every trial had a control filter that was fixed to a specific flow path for repeatability. For uncharged particles, configuration 1 was the control. This was equivalent to the current RASA configuration otherwise (filter media and air flow rate). For particle-pre-charging, configuration 2 was the control filter. Except for particle pre-charging, configuration 2 was equivalent to the RASA field configuration (air flow rate and filter media). Six data points were collected for each configuration of interest (3-8) where relative MDC measurements were always made with respect to the control filter. Table 7 shows how each trial consisted of specific flow configurations.

Table 6. Test Configuration Details

Mid-Scale Test Configurations	1 (control)	2 (control)	3	4	5	6	7	8
Filter material	FM1	FM1	FM2	FM2	FM2	FM2	FM3	FM3
Particle pre-charging (off/on)	off	on	off	on	off	on	on	on
Filter face velocity (m/s)	1.1	1.1	1.1	1.1	2.75	2.75	1.1	2.75
ΔP_f (psid)	0.33	0.33	0.20	0.20	0.53	0.53	0.06	0.23
$\Delta p_f/\Delta pf_0$ (-)	1.00	1.00	0.60	0.60	1.57	1.57	0.19	0.69
Q/Q_0 (-)	1.0	1.0	1.0	1.0	2.5	2.5	1.0	2.5

Table 7. Trial numbers and filter configurations where "x" represents a single filter sample being included in the trial

	Trial											
Configuration	**1**	**2**	**3**	**4**	**5**	**6**	**7**	**8**	**9**	**10**	**11**	**12**
1	x	x	x	x								
2					x	x	x	x	x	x	x	x
3	xx	x	xx	x								
4					x		x		x		x	xx
5	x	xx	x	xx								
6					x	x	x	x	x	x		
7					x	x	x	x	x	x		
8						x		x		x	xx	x

Particle size distributions from 10 nanometers to 10 micrometers are shown for trials 1-6 on page 65, and trials 7-12 on page 66. One distribution is shown for every three hours of data although data is available every one minute. The nSMPS instrument sizes particles based on electrical mobility. The OPS instrument sizes particles optically (i.e., light scatter). The conversion between electrical mobility diameter and optical diameter was not calculated since precise comparisons between OPS and nSMPS were not needed. Data are plotted against particle diameter, d_p, and reasonable agreement is observed at the crossover point. Total particle concentrations from the nSMPS instrument are shown on pages 67 and 68, for trials 1-6 and 7-12, respectively. Total particle concentrations from the OPS are shown on pages 69 and 70, for trials 1-6 and 7-12, respectively.

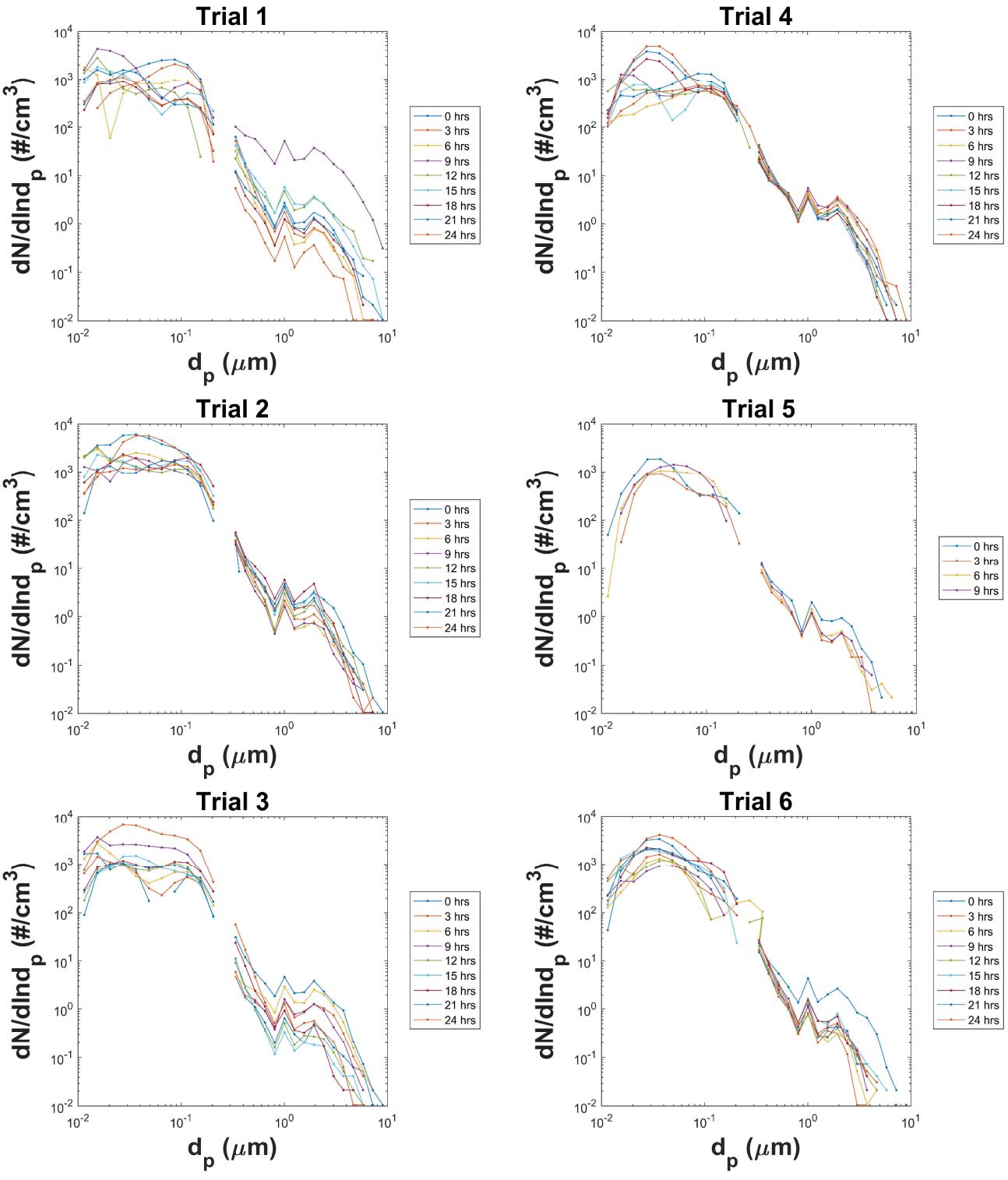
Trial 1
Trial 4
Trial 2
Trial 5
Trial 3
Trial 6
dN/dlnd$_p$ (#/cm^3)
d$_p$ (μm)
0 hrs
3 hrs
6 hrs
9 hrs
12 hrs
15 hrs
18 hrs
21 hrs
24 hrs

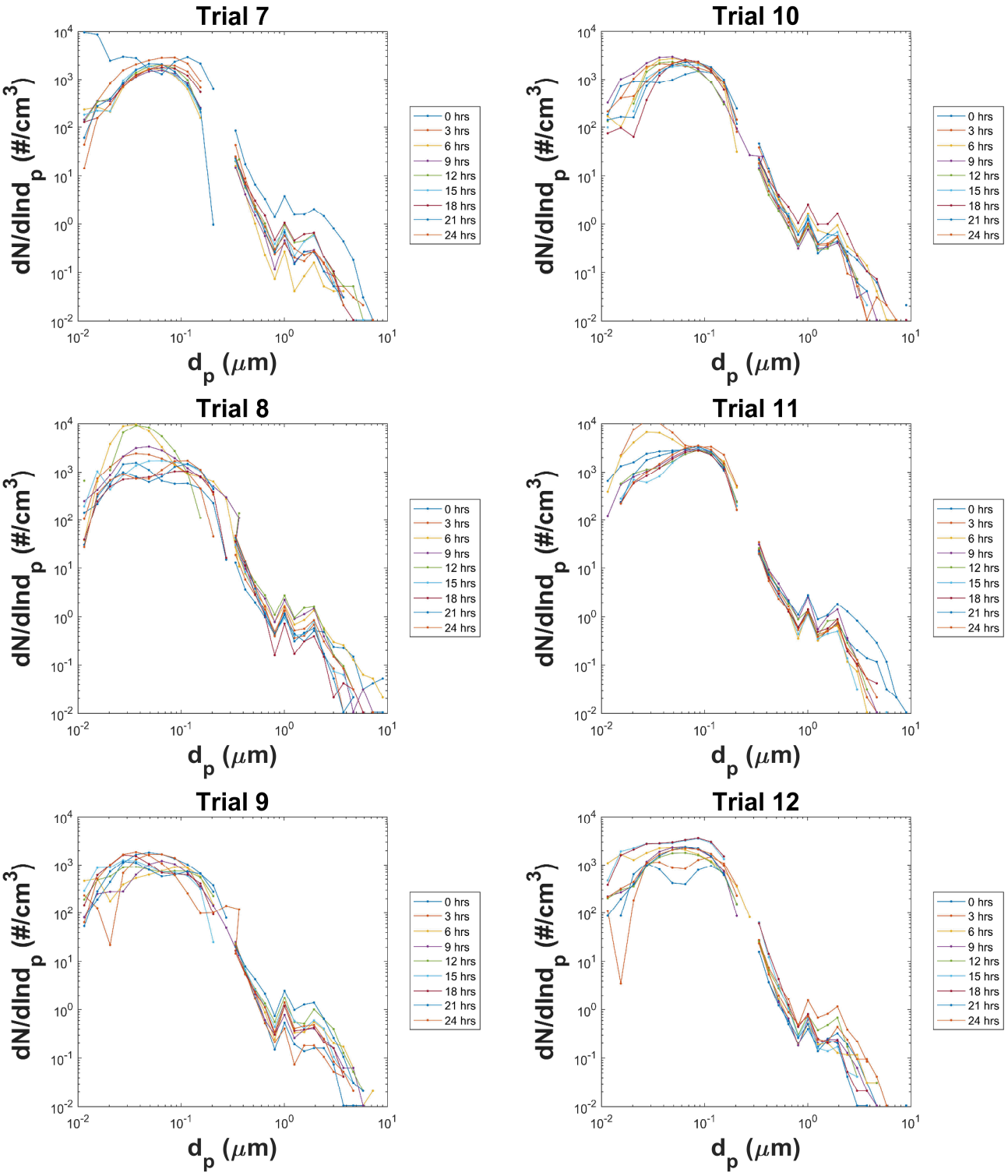
Trial 7
Trial 10
Trial 8
Trial 11
Trial 9
Trial 12
dN/dlnd$_p$ (#/cm^3)
d$_p$ (μm)
0 hrs
3 hrs
6 hrs
9 hrs
12 hrs
15 hrs
18 hrs
21 hrs
24 hrs

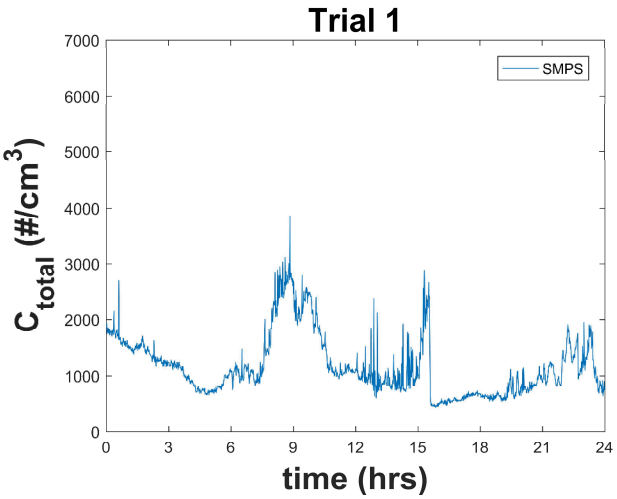
Trial 1
SMPS
C_{total} (#/cm^3)
time (hrs)

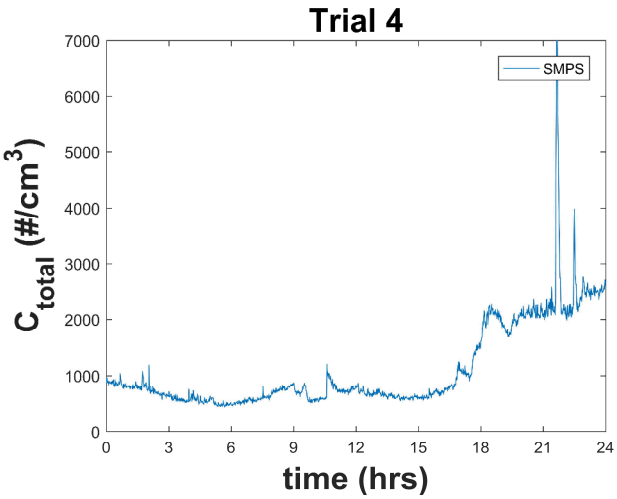
Trial 4
SMPS
C_{total} (#/cm^3)
time (hrs)

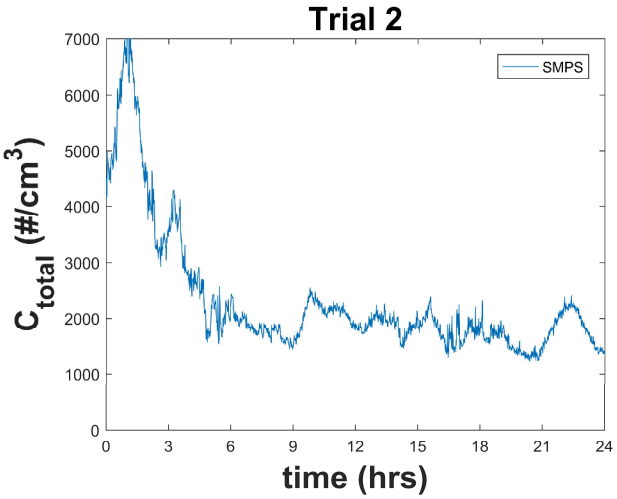
Trial 2
SMPS
C_{total} (#/cm^3)
time (hrs)

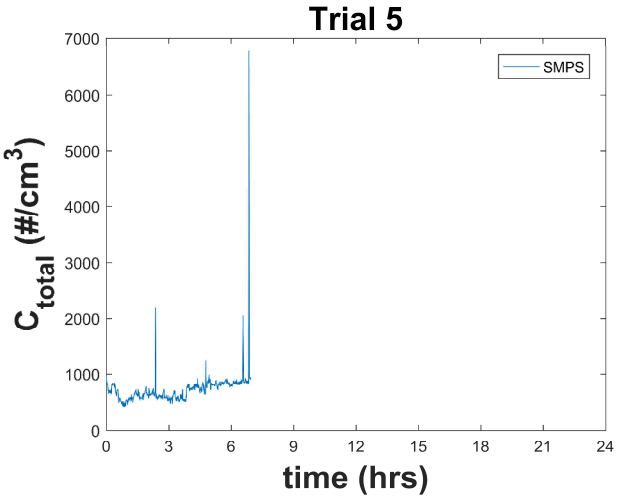
Trial 5
SMPS
C_{total} (#/cm^3)
time (hrs)

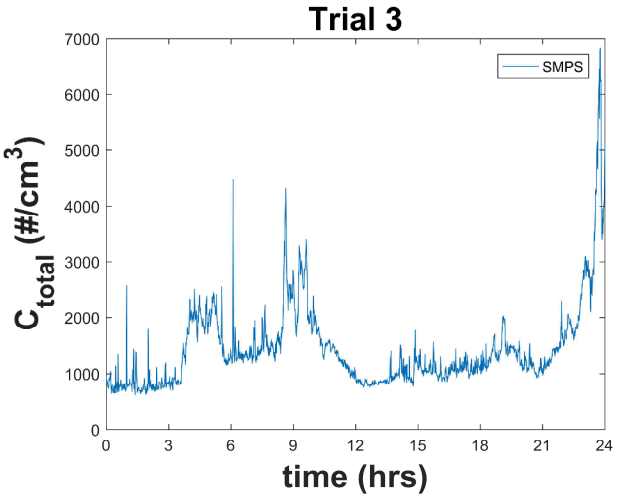
Trial 3
SMPS
C_{total} (#/cm^3)
time (hrs)

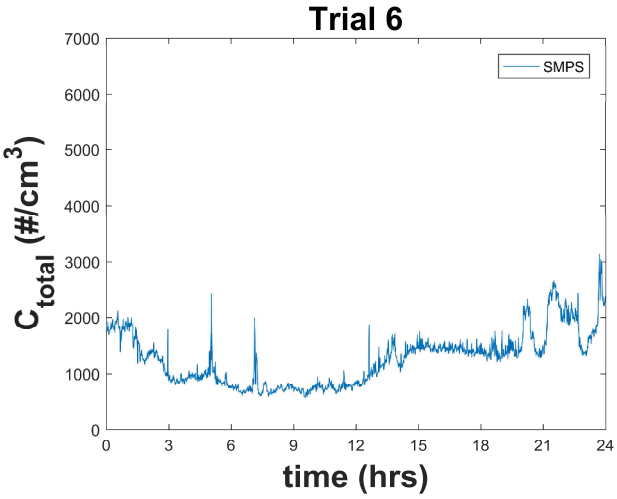
Trial 6
SMPS
C_{total} (#/cm^3)
time (hrs)

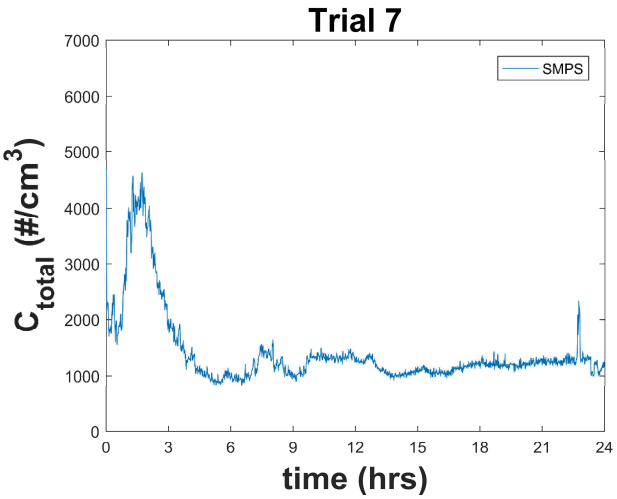
Trial 7
SMPS
C_{total} (#/cm^3)
time (hrs)

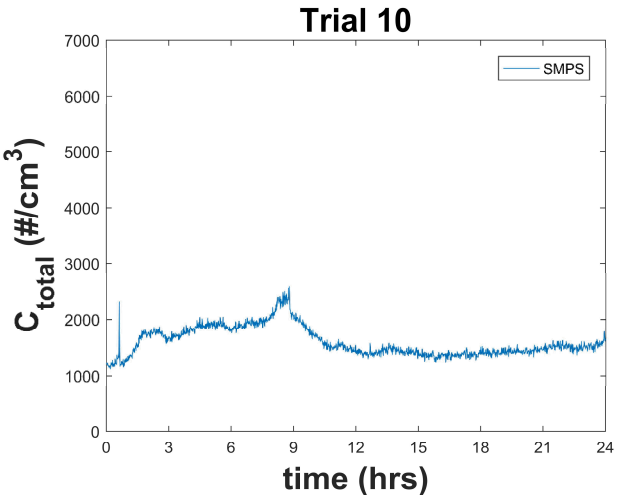
Trial 10
SMPS
C_{total} (#/cm^3)
time (hrs)

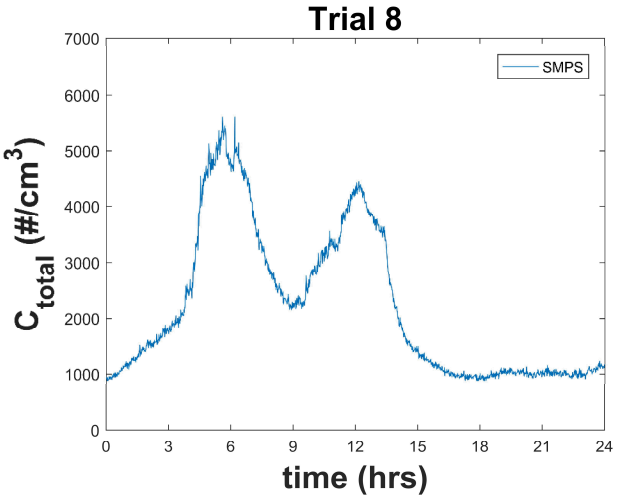
Trial 8
SMPS
C_{total} (#/cm^3)
time (hrs)

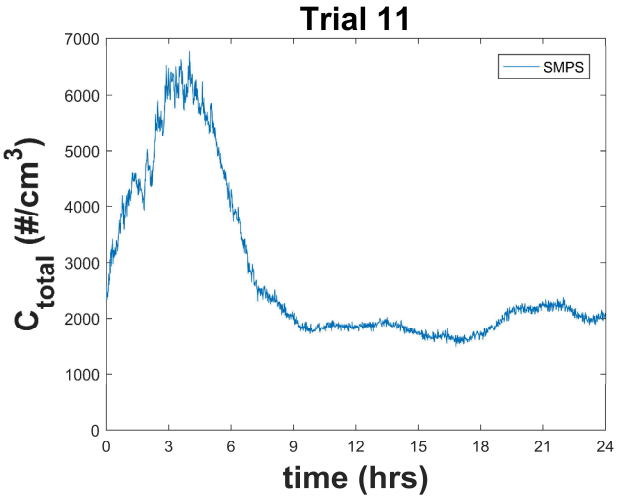
Trial 11
SMPS
C_{total} (#/cm^3)
time (hrs)

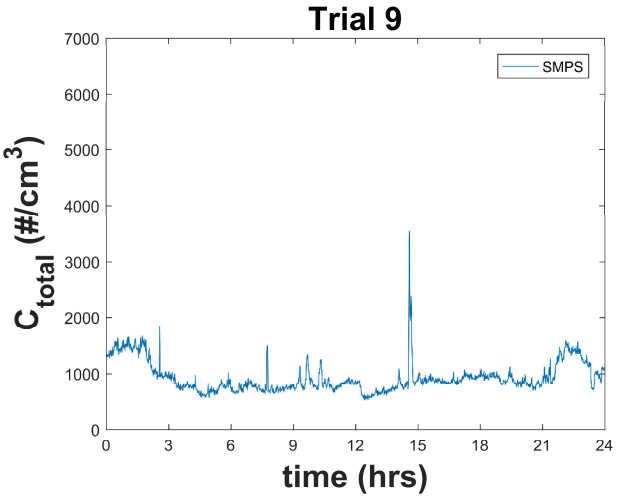
Trial 9
SMPS
C_{total} (#/cm^3)
time (hrs)

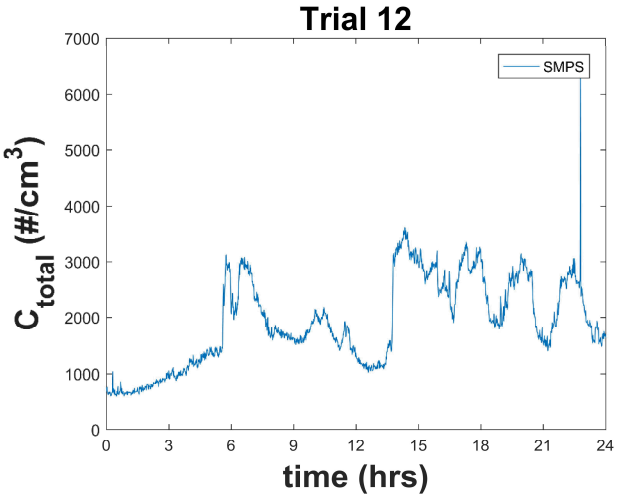
Trial 12
SMPS
C_{total} (#/cm^3)
time (hrs)

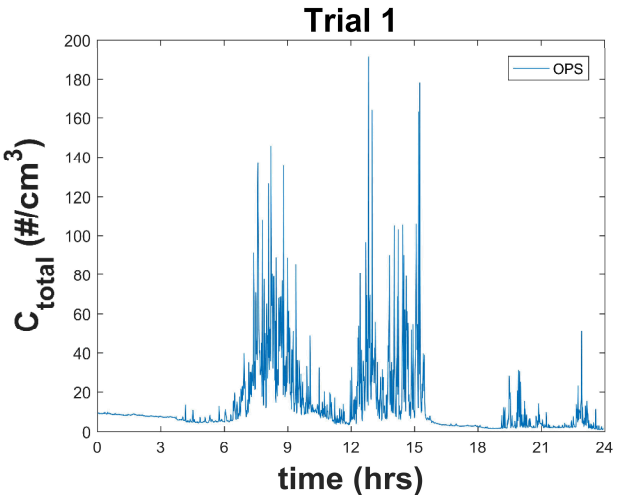
Trial 1
OPS
C_{total} (#/cm^3)
time (hrs)

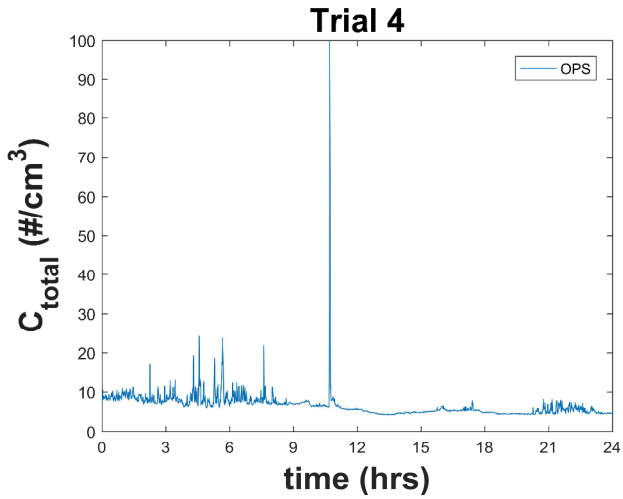
Trial 4
OPS
C_{total} (#/cm^3)
time (hrs)

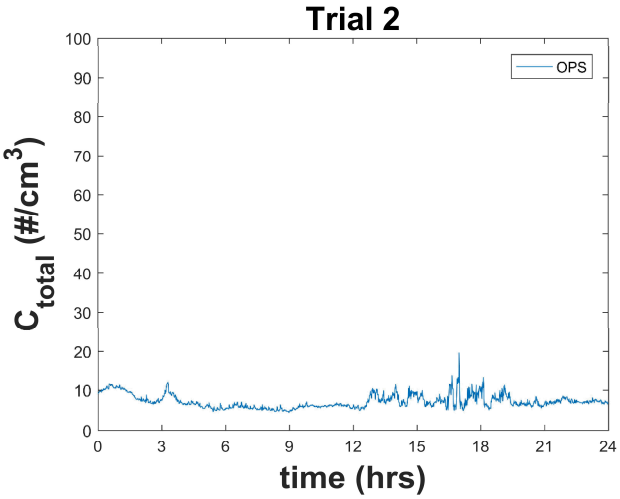
Trial 2
OPS
C_{total} (#/cm^3)
time (hrs)

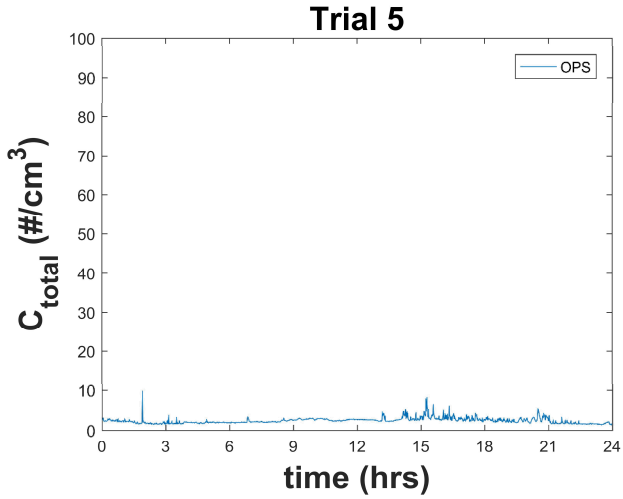
Trial 5
OPS
C_{total} (#/cm^3)
time (hrs)

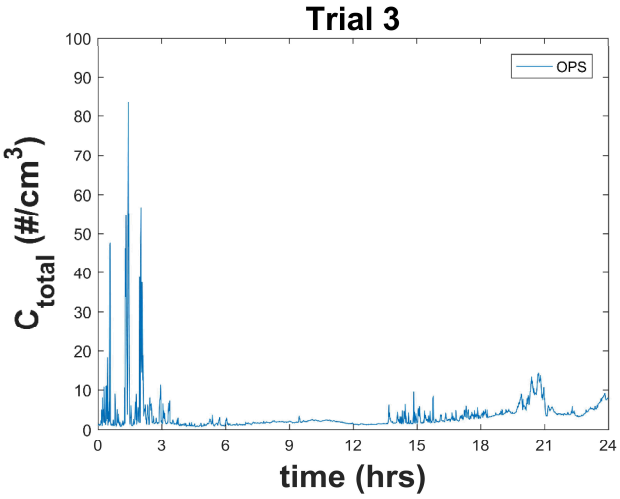
Trial 3
OPS
C_{total} (#/cm^3)
time (hrs)

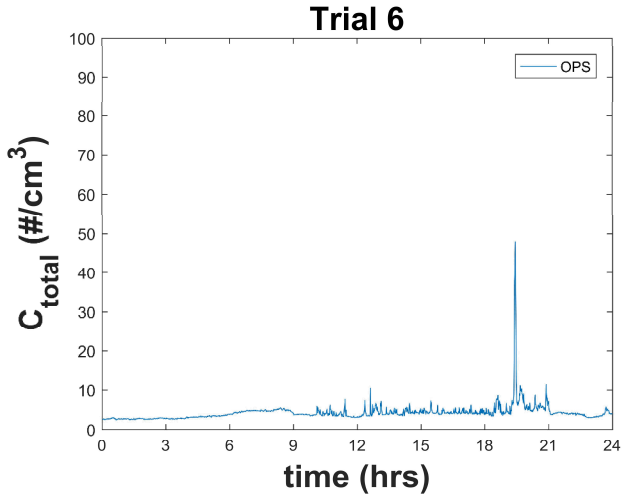
Trial 6
OPS
C_{total} (#/cm^3)
time (hrs)

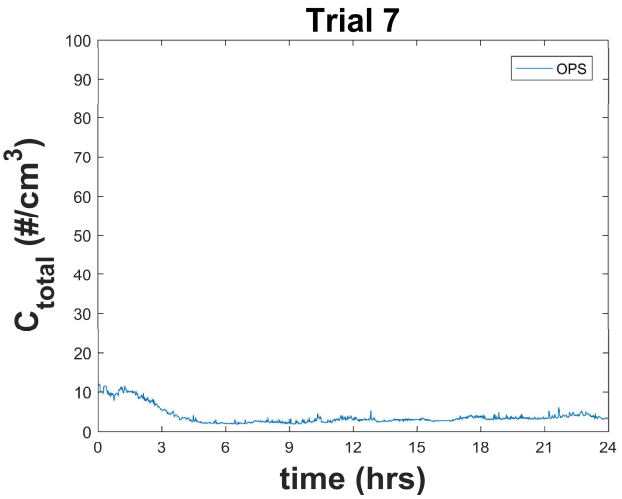
Trial 7
OPS
C_{total} (#/cm^3)
time (hrs)

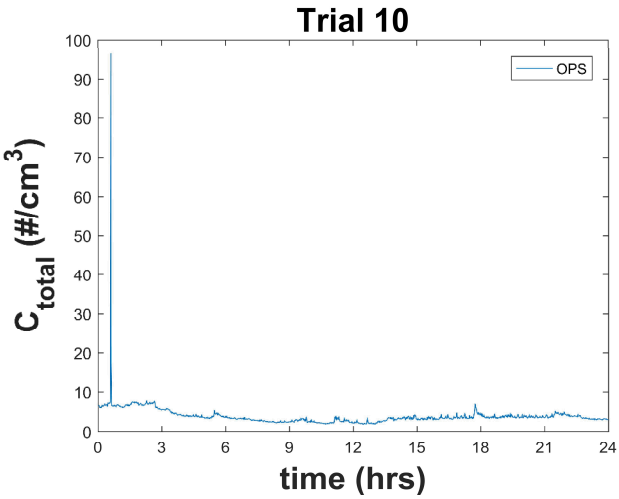
Trial 10
OPS
C_{total} (#/cm^3)
time (hrs)

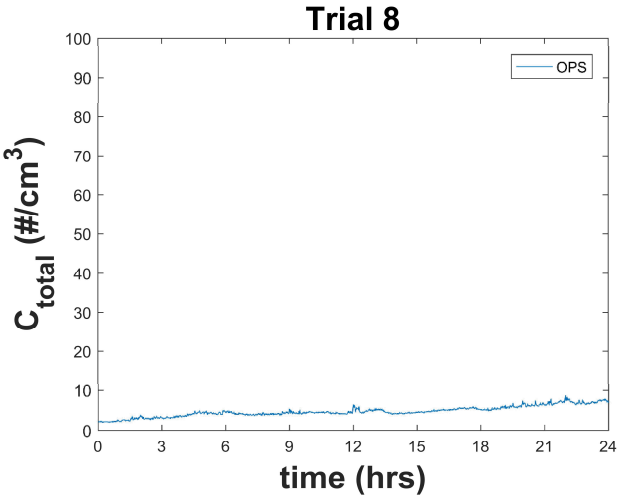
Trial 8
OPS
C_{total} (#/cm^3)
time (hrs)

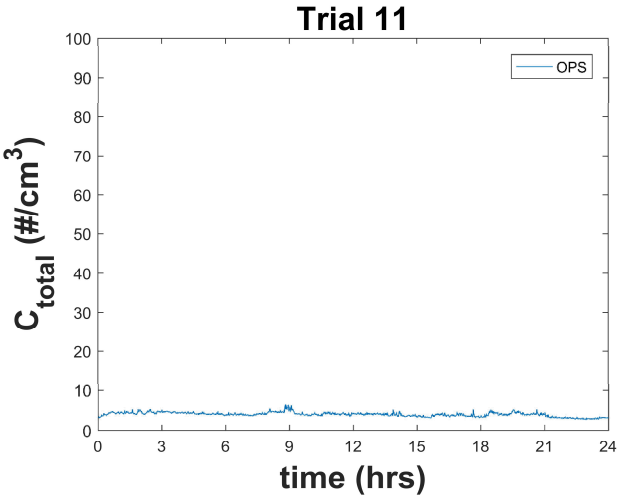
Trial 11
OPS
C_{total} (#/cm^3)
time (hrs)

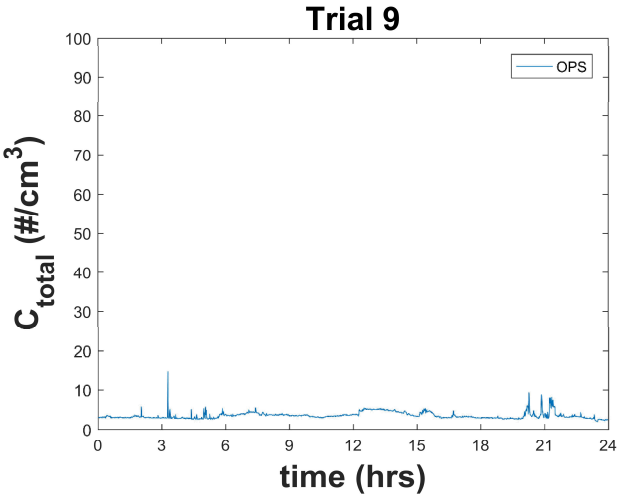
Trial 9
OPS
C_{total} (#/cm^3)
time (hrs)

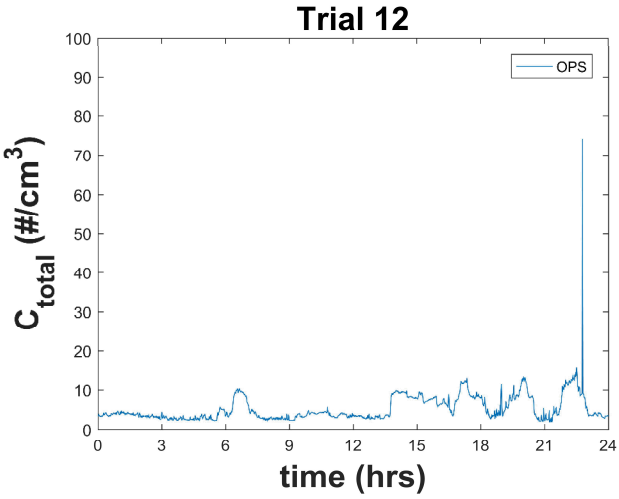
Trial 12
OPS
C_{total} (#/cm^3)
time (hrs)

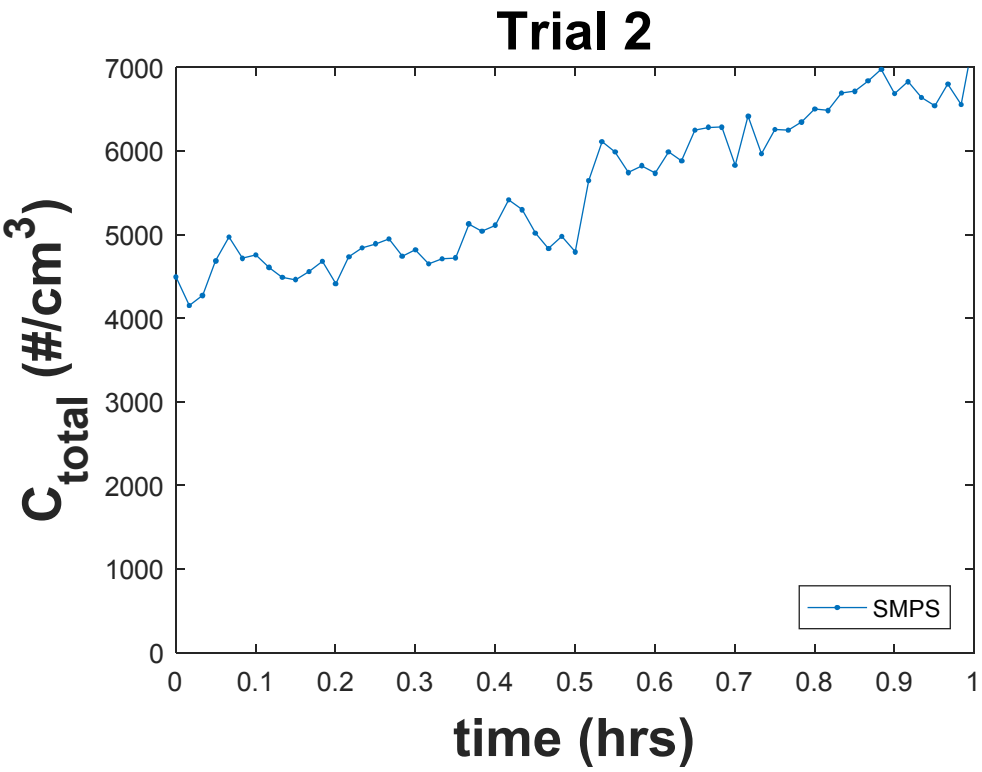

Figure 29. nSMPS total concentration (cm^{-3}) as a function of sampling time during the first hour of sampling. The total concentration varies 10-20% over time intervals of 5-10 minutes.

Temporal variations in aerosol concentration were observed for many of the trials. The first hour of trial 2 was examined more closely in Figure 29. The total concentration from nSMPS measurements was observed to increase from 4000 cm^{-3} to 7000 cm^{-3} over the course of the first hour (1100-1200). Smaller fluctuations were also observed over time periods of 5-10 minutes. We attributed this to local changes in wind speed with time. This supported our hypothesis that system verifications of equal aerosol concentrations in each filter flow path were complicated by temporal variations in aerosol concentration.

3.3 Radiometric methods

3.3.1 Introduction

The purpose of mid-scale filtration testing was to evaluate the relative MDC of new air filter media with respect to the current RASA system using ambient aerosol and radiometric methods similar to those used for field certification or RASA systems. RASA systems measure the presence of fission products such as Ba-140 that are indicative of nuclear testing. Ba-140's primary gamma emission energy is 537 keV with a 24.4% yield. The sensitivity of detecting these fission products is crucial to the successful operation of the radionuclide monitoring station and efforts were made to improve this sensitivity for enhanced nuclear treaty verification.

New filter media may allow for higher air flow rates thereby increasing the sample size for a 24-hour collection period. While an increased sample size will drive down the minimum detectable concentration, the increased air volume also leads to collecting more naturally occurring radioactive material (NORM) which increases the background and has the opposite effect on baseline sensitivity. Gamma spectroscopy of several replicate trials of several different configurations were used to determine if this increase in background had a significant effect on the overall Minimum Detectable Concentration (MDC) improvement.

Table 8 gives several radionuclides of interest for nuclear treaty monitoring, their half-lives, primary energies, and yields. Ba-140 is the most commonly referenced radionuclide for CTBT and is used to specify the baseline sensitivity (10-30 μBq m^{-3}) for RASA systems.

Table 8. Radionuclides of interest for treaty monitoring

Nuclide	Half Life (D)	Primary Energy (keV)	Primary yield (%)
Tc-99m	0.2504	140.51	89.06
I-131	8.04	364.4	81.2
La-140	1.678	1596.2	95.4
Ba-140	12.75	537.26	24.39

3.3.2 Theory

Several parameters were held constant for a given filter specimen. These controlled variables included the air flowing through the filter, the collection period, the hold period, and the count period. What could not be held constant was the detector system on which samples were analyzed since four samples had to be characterized simultaneously. All samples had to be counted at the exact same time for the effects of radionuclide decay to be ignored. Four detector systems were used for the analysis of the air filters.

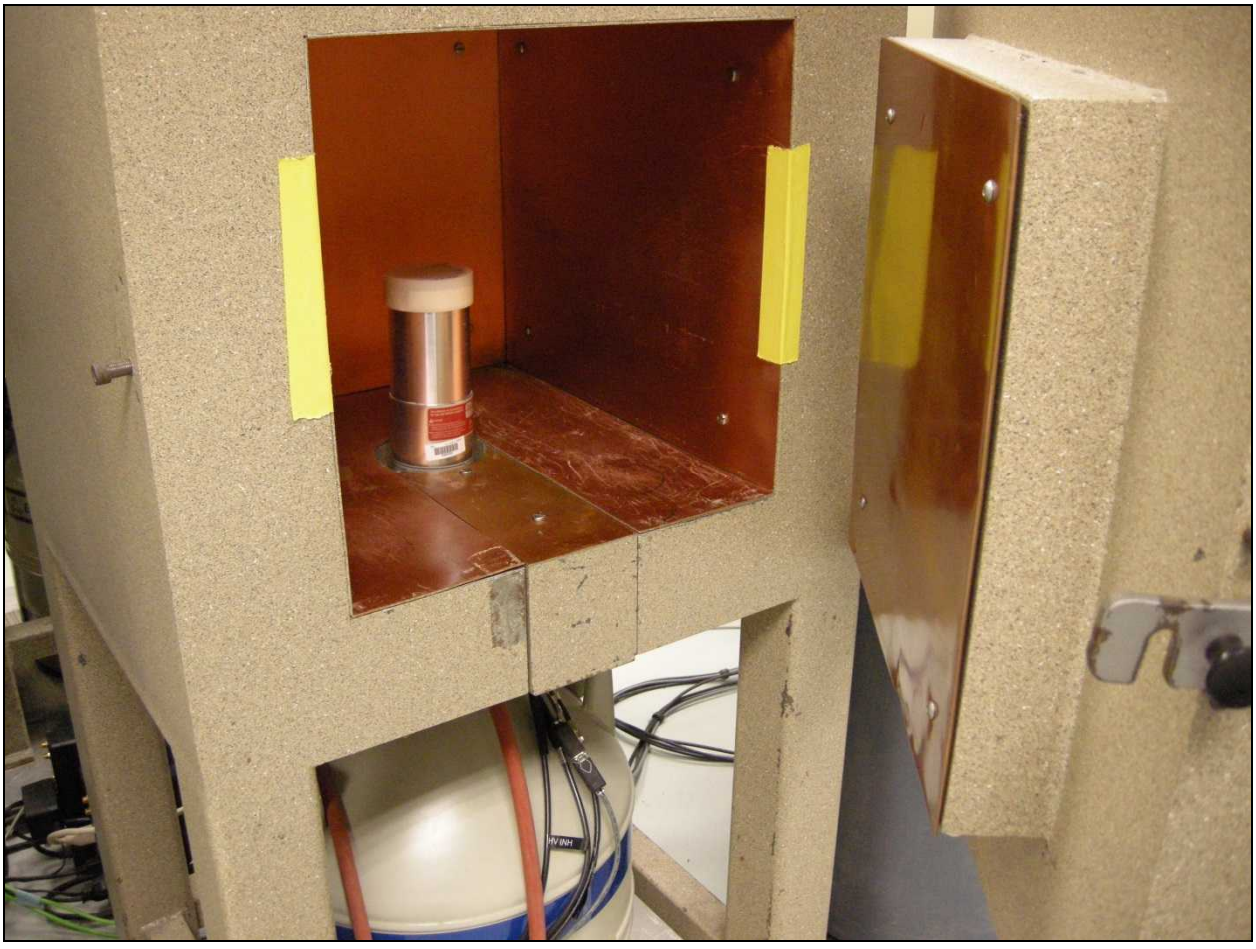

Figure 30: High-Purity Germanium (HPGe) Gamma Spectrometer. Low-background graded shield, liquid nitrogen cooled

Four laboratory-grade High-Purity Germanium (HPGe) gamma spectrometers were used to analyze each trial of four filter configurations. One such detector is shown in Figure 30. While each detector is slightly different in size, shape, and efficiency, each has a similar low-

background shield. The differences in detector efficiencies required a correction be made to the data prior to comparison of the minimum detectable activities (MDAs). The correction factors were determined by collecting four identical air samples that were counted on all four detectors at the same time. This data was used to normalize the efficiency to the detector that the control filter was counted on. Relative efficiencies for each detector are given in Table 9.

Table 9: HPGe Detector Relative Efficiencies

Detector ID	% Relative Efficiency
LAB01	28
LAB02	42
LAB05	36
LAB06	50

Table 10 lists the detector normalization factors determined in method testing for several radionuclides of interest in treaty monitoring.

Table 10. Correction factors for each detector and each radionuclide of interest. The correction factor is ratio of LAB01 MDA to the MDA of each detector for the given nuclide.

Nuclide	LAB01	LAB02	LAB05	LAB06
Tc-99m	1.00	1.27	1.14	1.08
I-131	1.00	1.45	1.12	0.89
Ba-140	1.00	1.50	1.21	1.19
La-140	1.00	1.59	1.47	1.42

To correct for the differences in efficiency of these detectors, mid-scale filtration data were normalized to one detector: the detector that was used to count the control filter run with each trial (herby referred to as the "control detector"). This normalization factor was the ratio of the Minimum Detectable Activity (MDA) achieved for a source in the same geometry at a given energy to that of the control detector. This method was tested by analyzing the same calibration standard on each detector for the same period of time. The MDA was calculated for the same Region of Interest (ROI) in each measurement (Table 11) and multiplied by the correction factor to achieve a normalized MDA (Table 12). The normalized MDAs were equal which

demonstrates that the correction factor adequately corrects for the difference in detectors used in the experiment.

Table 11. Minimum Detectable Activity for a 60 min count of a 2" air filter on contact (units are arbitrary)

Nuclide	LAB01	LAB02	LAB05	LAB06
Tc-99m	0.605	0.467	0.534	0.554
I-131	1.35	0.92	1.19	1.48
Ba-140	6.23	4.07	5.2	5.29
La-140	1.54	1.11	0.981	1.23

Table 12. Normalized MDAs for a 60 min count of a 2" air filter on contact (units are arbitrary)

Nuclide	LAB01	LAB02	LAB05	LAB06
Tc-99m	0.61	0.59	0.61	0.60
I-131	1.35	1.34	1.34	1.32
Ba-140	6.23	6.11	6.31	6.29
La-140	1.54	1.77	1.44	1.75

The spectral continuum background for each filter varied due to the difference in collection volume. This background continuum was a function of, among other things, the naturally occurring radioactive material (NORM) present on the filter that emitted gamma rays with energies higher than that of the nuclide of concern (such as Pb-212). The filter volume and this increased background were competitors in determining the MDA. To quantify the overall improvement to the MDC for each experimental configuration without the effect of the differences in the detector systems, the MDA was normalized. Each normalized MDA was compared to the control filter to yield the relative difference in MDA and subsequently, the relative change in MDC due to changes in air flow rate, filter material, and particle-pre-charging.

An illustration of gamma spectroscopy data is shown in Figure 30. A 24-hour background spectrum of a pristine filter (not exposed to aerosol flow) is shown in blue. A 24-hour spectrum of trial 1, configuration 2, is shown in black. The Pb-212 peak due to NORM in the air collected is highlighted. Pb-212 is a radon daughter that contributes to the background spectrum. Note that while there is some Pb-212 in the background spectrum (blue line, from the

environment the detector is in) the peak area of this is much smaller than what is observed in the collected air (black line). This NORM in the air is the primary contributor to the continuum in the Region of Interest (ROI) which causes the Ba-140 sensitivity to be non-zero. For treaty verification, the signature of Ba-140 must be observed over the background spectrum. The Tc-99m ROI is shown in the figure. This region of interest is where a peak would show up if there were Tc-99m in the sample. Note a very small peak in this ROI is due to a minor contributor in the natural background. The number of counts in this ROI drives the Minimum Detectable Activity and subsequently the Minimum Detectable Concentration. Since the nearest large peak in the air spectrum (Pb-212) is nearly 100 keV away from the ROI, even large changes in the peak area will have a small effect on the number of counts in the ROI. Thus, collecting more air, in effect increasing the NORM collected, had a minimal effect on the detection sensitivity for Tc-99m. The same argument can be made for the other radionuclides of interest (I-131, La-140, Ba-140).

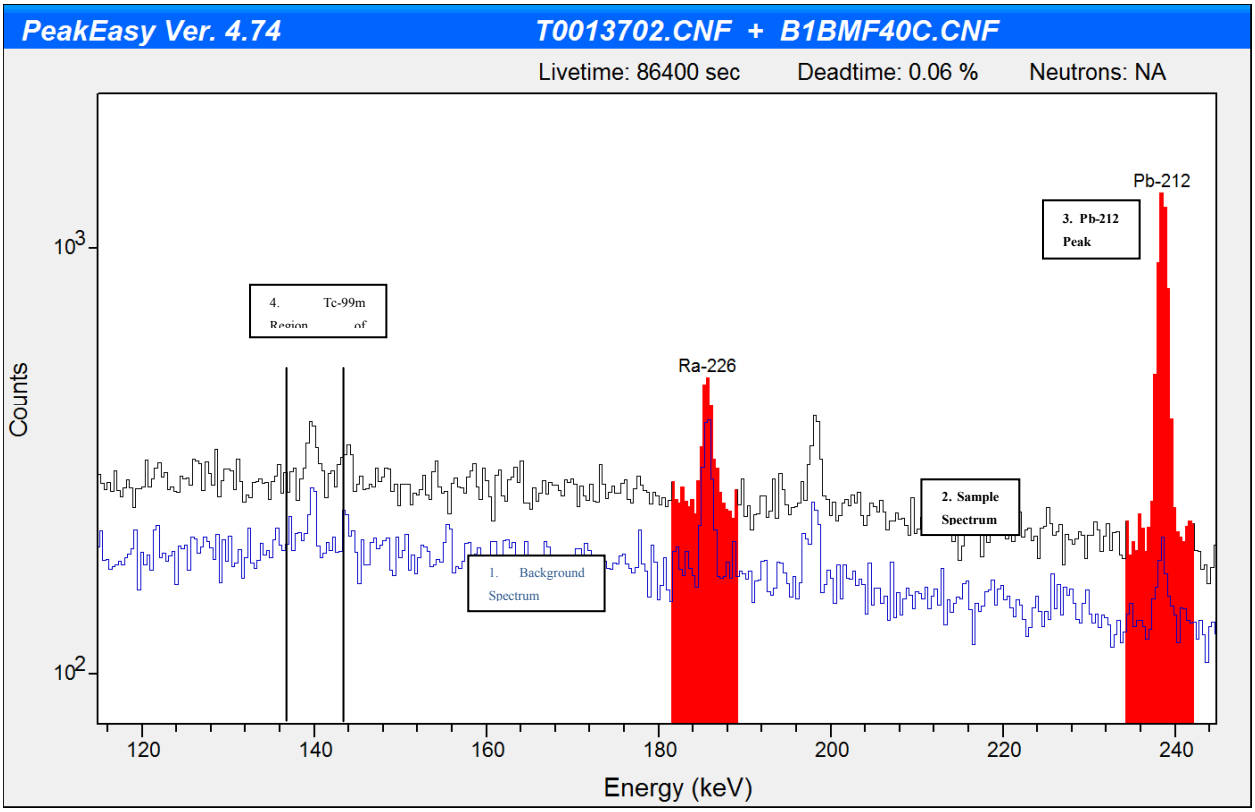

Figure 31: Gamma Spectrum for Trial 1, Configuration 3 (in black) compared to a background spectrum (in blue)

3.3.3 Experiment and Data Reduction Methods

Filter configurations were experimentally compared by running 24-hour collections side-by-side with the mid-scale filter test apparatus. The filters were then given a 24-hour decay time before counting in the laboratory. The radiochemistry laboratory at SNL does not have detectors identical enough to simply count the filters at the same time and compare the results directly. Thus, corrections were made to account for the difference in efficiencies between the detectors as described in the Theory section above.

The normalization factor for the MDAs was determined by analyzing the same source for the same period of time on all four detectors, calculating the detector's MDA and taking the ratio of the i^{th} detector to the basis detector. In this experiment, this was achieved by collecting identical control air filters (configuration 1) on all four filter flow paths, holding these four controls for an equal amount of time, and counting on all four detectors simultaneously. This was the purpose of trial 000. Trials 0 and 00 were used to establish laboratory methods. Since this correction factor is for the gamma detector systems, it can be utilized for all 12 trials, regardless of any changes in experimental variables. The correction factor was determined as follows:

$$F_i = \frac{MDA_B}{MDA_i} \tag{8}$$

where MDA_B was the MDA of the Basis Detector, MDA_i was the MDA of the i^{th} Detector, and F_i was the normalization factor for the i^{th} Detector.

MDA is a function of the number of continuum counts in the ROI. Since all other sources of error were held constant, the only uncertainty considered to be important was due to counting statistics. In this analysis the uncertainty in the measurement of the MDA was assumed to be equal to the square-root of the number of counts in the ROI used to determine the MDA. The relative uncertainty in the MDA was equal to the square root of the number of counts divided by the number of counts. The result of combining the relative uncertainties for the MDA of the basis detector and the MDA of the i^{th} detector in quadrature is given in (9):

$$\frac{\sigma_{F_i}}{F_i} = \sqrt{\frac{1}{N_B} + \frac{1}{N_i}} \tag{9}$$

where N_B is the counts in the ROI from the Basis Detector, N_i is the counts in the ROI from the Basis of the i[th] Detector, and σ_{F_i} is the uncertainty in the normalization factor for the i[th] Detector.

Each trial consisted of four air filters. The air filter counted on detector LAB01 was always the control filter (Configuration 1 or 2). To get the MDA of the i[th] detector in a form that could be compared to the control, (9) was used to get the normalized MDA for the i[th] detector - $\overline{MDA}_i$:

$$\overline{MDA}_i = F_i \cdot MDA_i \ . \tag{10}$$

The uncertainty in this value was calculated by (9).

$$\overline{\sigma}_i = \overline{MDA}_i \sqrt{\left(\frac{\sigma_{F_i}}{F_i}\right)^2 + \frac{1}{N_i}} \tag{11}$$

To determine the relative difference in MDA (RD_i) for the i[th] detector, the normalized MDA's were compared to the control (10).

$$RD_i = \frac{MDA_i - MDA_c}{MDA_c} \cdot 100 \tag{12}$$

The RD_i was the percent change in MDA of the experimental configuration relative to the control. Equation (12) was a function of the control MDA and the experiment MDA. Since the control MDA term was in both the numerator and the denominator. To account for the effect of "compensating errors" the general law of propagation of uncertainties was used to derive the equation for the uncertainty in RD_i rather than a stepwise propagation that misses these compensating effects. Applying the law to (11) yielded (13), the absolute uncertainty in the relative difference (σ_{RD_i}).

$$\sigma_{RD_i} = \frac{\overline{MDA}_i}{MDA_c} \sqrt{\left(\frac{\sigma_c}{MDA_c}\right)^2 + \left(\frac{\overline{\sigma}_i}{\overline{MDA}_i}\right)^2} \tag{13}$$

3.3.4 Experiment Plan

There were six different non-control filter configurations for three filter media. One of the test filters must have particle charging (FM3) according to results from small-scale testing that showed it did not perform adequately without particle pre-charging. Particle pre-charging was not required for FM2 although benefits were found in lab-scale testing. There were two

controls: Configuration 1 without particle charging using the current RASA media and Configuration 2 with particle charging using the current RASA media. Aside from the media and the particle charging, the filter face velocity was independently varied. This lead to eight total configurations, the details of which can be found in Table 6.

The configurations were organized into trials each producing four filters to be analyzed, one control and three experimental configurations. The details of the trials can be found in Table 7. Each X represents a filter placed on the mid-scale filtration apparatus. For some trials, two filters in the same configuration were tested in one trial. The experiments without pre-charging were tested in configurations 1, 3 and 5 and took place over 4 trials for a total of 6 replicates of each configuration. The experiments with pre-charging on were tested in configurations 2, 4, 6, 7, and 8 and took place over 8 trials for a total of 6 replicates of each configuration.

The normalization factors were determined by running four identical control configurations on all four filters with subsequent counting on all four detectors. Since the normalization factors apply only to the detector systems, configuration 1 was a suitable normalization filter for both experiments (pre-charging on and off). Therefore, a trial labeled 000 was carried out with all four configurations being configuration 1.

3.4 Data

The sampling apparatus was tested with configuration 1 several times before a set was determined to be suitable for calculating correction factors. The third baseline set, Trial 000, was used to determine the correction factors for both experiments. The data in Figure 32 shows a consistent Pb-212 concentration on each filter demonstrating uniformity across the four filters which was critical in determining a set of consistent baseline filters.

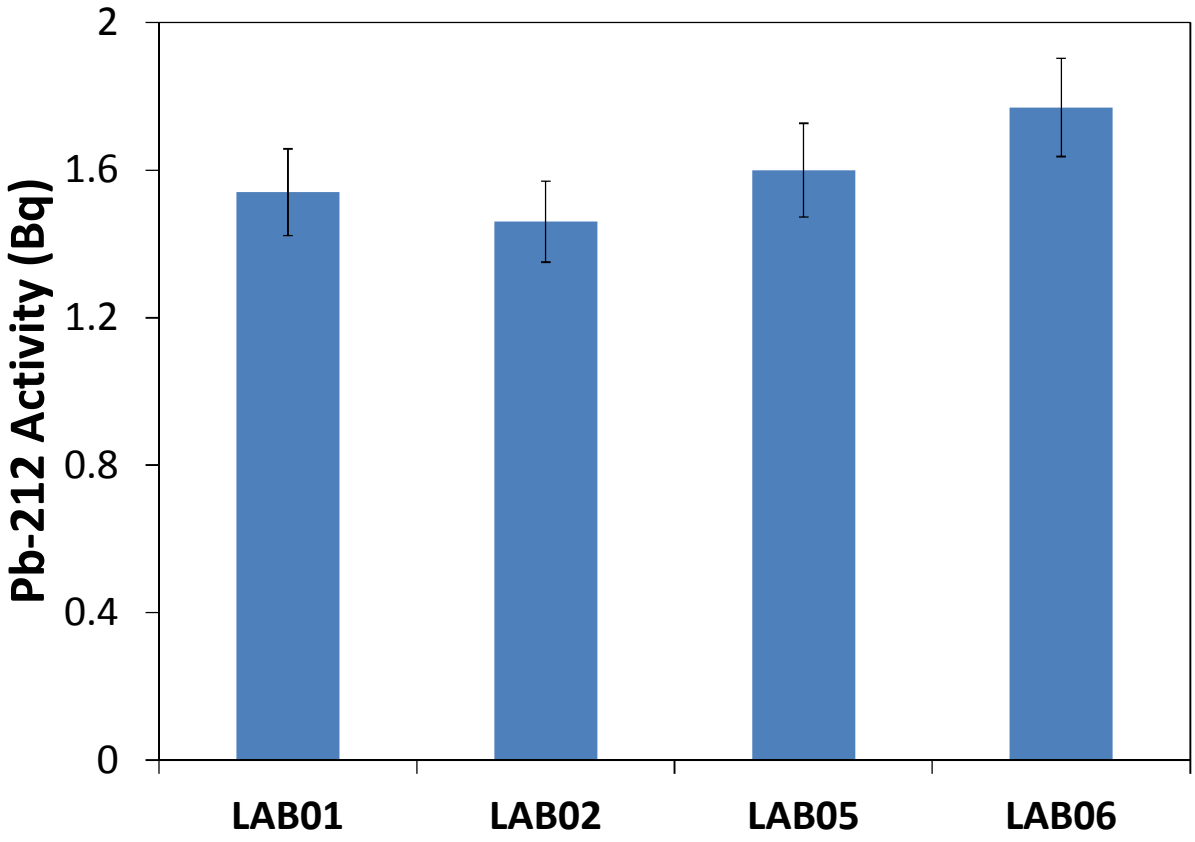

Figure 32: Comparison of Pb-212 Activity on Baseline Trial 000 Filters in Configuration 1

Correction factors were determined from this set by calculating the ratio of the MDA for four radionuclide regions of interest (ROIs) to that of the control detector (LAB01).

Table 13. Detector Correction Factors

Nuclide	LAB01	LAB02	LAB05	LAB06
Tc-99m	1.00	0.76	0.68	0.48
I-131	1.00	0.95	0.69	0.46
Ba-140	1.00	1.00	0.74	0.63
La-140	1.00	1.06	0.74	0.72

The uncertainty in these correction factors were estimated using simple counting statistics and the law of propagation of uncertainty. The relative uncertainty of each correction factor is found in Table 14.

Table 14. Relative Uncertainty in the Detector Correction Factor

Nuclide	LAB01	LAB02	LAB05	LAB06
Tc-99m	3.83%	3.40%	3.67%	3.19%
I-131	5.54%	5.16%	5.42%	4.57%
Ba-140	6.86%	6.42%	6.70%	5.89%
La-140	12.60%	11.59%	11.93%	11.19%

Over the course of roughly a month and a half, the 12 trials were run and each filter was analyzed on the associated detector system. The collected data was in the form of the MDA and the continuum used to determine the MDA (for uncertainty analysis). While the entire dataset was not presented here since it is unwieldy and cumbersome, all data can be found in the Radiation Protection Sample Diagnostics data archive.

3.4.1 Results and Discussion

Once the data was compiled, it became clear that counting statistics played a larger role than expected. Even with significant material on the filters and a long count time the continuum found in the ROIs for the nuclides considered in this study were quite low. They ranged from around 100 to 3500 counts which yielded uncertainties between 10% and 1.7% respectively. When combined in quadrature with other uncertainties (such as the baseline counting uncertainty and the correction factor uncertainty) the total propagated uncertainty became quite large. The radionuclide with the smallest relative uncertainty was Tc-99m since it emits a gamma ray with a lower energy than the others and thus has the largest continuum (counts). While the measurement uncertainty for the other radionuclides may be too large to be considered in this discussion they will indeed follow the trends established for Tc-99m. Again, Tc-99m was used to analyze the relative change in MDC since the other radionuclides of interest were present but with low counts. Our mid-scale system utilized a 2" filter, which had roughly 0.1% of the area (and air flow) of fielded RASA's. Thus, the total counts from mid-scale tests would be approximately 0.1% of the total counts from a full-scale test.

The six replicates for each of the configurations for each filter media were averaged to obtain the average change in MDA for Tc-99m and the standard deviation of the six replicate measurements. Table 15 below relates the air collection parameters to these results. While the uncertainty in the measurement of the MDA change is very large, it is clear that the samples with

2.5 times the air volume of the control filter do show elevated MDAs (although only by a few percent). When compared with the improvement in MDC gained by increasing the air volume by a factor of 2.5, the contribution due to the increased background is negligible. In summary, the collection time, decay time, and count time adequately reduce the background and yield a measurement that can fully realize the improvement by increasing the sample collection volume.

Table 15. Mid-Scale Testing Results Summary

Mid-Scale Test Configurations	1	2	3	4	5	6	7	8
Filter material	FM1	FM1	FM2	FM2	FM2	FM2	FM3	FM3
Particle pre-charging (off/on)	off	on	off	on	off	on	on	on
Filter face velocity (m/s)	1.1	1.1	1.1	1.1	2.75	2.75	1.1	2.75
ΔP_f (psid)	0.33	0.33	0.2	0.2	0.53	0.53	0.06	0.23
$\Delta p_f/\Delta pf_0$ (-)	1	1	0.6	0.6	1.57	1.57	0.19	0.69
Q/Q_0 (-)	1	1	1	1	2.5	2.5	1	2.5
Volume Comparison to Control Filter	CONTROL	CONTROL	1	1	2.5	2.5	1	2.5
Tc-99m Average MDA change (% of control filter) Errors at 1-sigma	CONTROL	CONTROL	2 ± 3 %	7 ± 4 %	1 ± 3 %	4 ± 3 %	3 ± 3 %	6 ± 3 %
Tc-99m Average MDC change (% of control filter) Errors at 1-Sigma	CONTROL	CONTROL	-2 ± 3 %	1 ± 3 %	-55 ± 3 %	-57 ± 1 %	2 ± 4 %	-58 ± 1 %

3.4.2 Summary and Conclusion

A method was developed to determine the improvement to the MDA (and subsequently the MDC) of new filter configurations relative to the existing configuration used in fielded RASA systems. The SNL research team showed that increasing the amount of background introduced by natural radioactive material in the air (NORM) with an increased sample volume did not have a significant effect on the MDA. This meant that when considering the increased volume in the Minimum Detectable Concentration (MDC) calculation, the improvements were fully realized and did not show a significant dependence on the NORM. An MDC of nearly 55-60% lower was achieved in trials where the sample collection volume was increased by a factor of 2.5. The increase in NORM had no measurable effect on these results.

4 DISCUSSION

4.1 Weighted average collection efficiency

Changes to the minimum detectable concentration (MDC) attributed to changes in collection efficiency can be incorporated into equation (6). However, the collection efficiency curves (E vs. d_a) measured in laboratory-scale testing must be collapsed to a single quantity ($\hat{E}$). In this study, we formulated average weighted collection efficiencies for MDC calculations where the weighting function was derived from the particle size distribution of atmospheric aerosol. We proposed to use the surface area weighted particle size distribution rather than the number particle size distribution. The most plausible pathway for radionuclide aerosol emission from underground nuclear tests is the emission of volatile gases which then condense on background aerosols through transmutation. The background aerosols containing trace radionuclide signatures are then collected by the RASA.

The tri-modal lognormal particle size distribution used to represent atmospheric aerosols is given by the following:

$$\frac{dN}{d\ln(d_p)} = \frac{n_1}{\sqrt{2\pi}\ln(\sigma_{g1})}\exp\left[\frac{-\left[\ln(d_p)-\ln(d_{g1})\right]^2}{2\left[\ln(\sigma_{g1})\right]^2}\right] + \frac{n_2}{\sqrt{2\pi}\ln(\sigma_{g2})}\exp\left[\frac{-\left[\ln(d_p)-\ln(d_{g2})\right]^2}{2\left[\ln(\sigma_{g2})\right]^2}\right] + \frac{n_3}{\sqrt{2\pi}\ln(\sigma_{g3})}\exp\left[\frac{-\left[\ln(d_p)-\ln(d_{g3})\right]^2}{2\left[\ln(\sigma_{g3})\right]^2}\right] \quad . \tag{14}$$

For equation (14), variables are defined in Table 16.

Table 16. Variable definitions for equation (14), tri-modal, lognormal, aerosol particle size distribution

$\frac{dN}{d\ln(d_p)}$	The differential form of aerosol number concentration (dN) where $\ln(d_p)$ is the dependent variable. Units are in particles per cm^3.
$n_1,\ n_2,\ n_3$	The total number concentration of particles for each mode of the aerosol distribution. Mathematically, the integral of (14) from $-\infty < \ln(d_p) < \infty$ gives the sum of number concentrations for each mode $n_1 + n_2 + n_3$. Number concentrations are typically expressed as particles per cm^3.
d_p	Particle diameter is the independent variable in the tri-modal lognormal size distribution. For mathematical purposes, the variable transformation $\ln(d_p)$ is often used. Particle size is normalized to remove any units prior to taking the natural logarithm. As expected, $\ln(d_p)$ is unitless.
$\sigma_{g1},\ \sigma_{g2},\ \sigma_{g3}$	The geometric standard deviation of the lognormal distributions for each particle size mode.
$d_{g1},\ d_{g2},\ d_{g3}$	The geometric mean diameter of the lognormal distribution for each particle size mode.

Whitby and Sverdrup (1980) presented 8 sets of parameters describing common atmospheric aerosols. There are three size modes typical of atmospheric aerosols: the nucleation mode containing particles which have formed from gas phase precursors, the accumulation mode consisting of particles which have formed from agglomerated nucleated particles and persist in the atmosphere for long periods of time, and the coarse mode containing dust and other particles that have been re-entrained from the ground. The 8 parameter sets provided by Whitby and Sverdup represent everything ranging from coastal, inland, urban, and pristine conditions. For this work, we selected the average. However, for certain locations, other particle size distributions may be more appropriate and could be analyzed on an ad hoc basis. Atmospheric aerosol size distribution parameters are given below.

Table 17. Tri-modal, lognormal, atmospheric particle size distribution parameters from Whitby and Sverdup (1980)

Parameter	Value	Units	Parameter	Value	Units	Parameter	Value	Units
d_{g1}	29	(nm)	σ_{g1}	1.66	(-)	n_1	2.04e4	(#/cm^3)
d_{g2}	290	(nm)	σ_{g2}	2.02	(-)	n_2	1.68e3	(#/cm^3)
d_{g3}	6.3	(μm)	σ_{g3}	2.26	(-)	n_3	0.2	(#/cm^3)

The surface area particle size distribution, $dS / d\ln(d_p)$, is formed from the moment of the number particle size distribution:

$$\frac{dS}{d\ln(d_p)} = \frac{dN}{d\ln(d_p)} \pi d_p^{\,2} \ . \tag{15}$$

The units of $dS / d\ln(d_p)$ are often expressed as square micrometers of particle surface area per cubic centimeter of air (μm^2/cm^3). We suggest that this is the most important characteristic of the particle size distribution since volatile gases released from underground nuclear explosions are likely to condense onto the surface of atmospheric aerosol particles. Another moment can be formed from the number particle size distribution to give particle mass per unit volume of air. The mass size distribution would become important if volatile gases vented from underground nuclear explosions were nucleating to form large particulates of solid radionuclide decay products. The number particle size distribution for the parameters in Table 17 are shown in Figure 33. The three modes (nucleation, accumulation, and coarse) are observable.

The cumulative number distribution can be calculated from integrals of (14) as follows:

$$F_N(d_p) = \frac{\int_0^{d_p} \frac{dN}{d\ln(d_p)} d\ln(d_p)}{\int_0^{\infty} \frac{dN}{d\ln(d_p)} d\ln(d_p)} = \int_0^{d_p} \frac{d(N/N_T)}{d\ln(d_p)} d\ln(d_p) \ . \tag{16}$$

The cumulative number distribution for average atmospheric aerosol is shown in Figure 34. This curve is interpreted as the percent of total atmospheric particles, based on number, which reside in particles below size d_p. By number, nearly all atmospheric particles are less than about 200 nm.

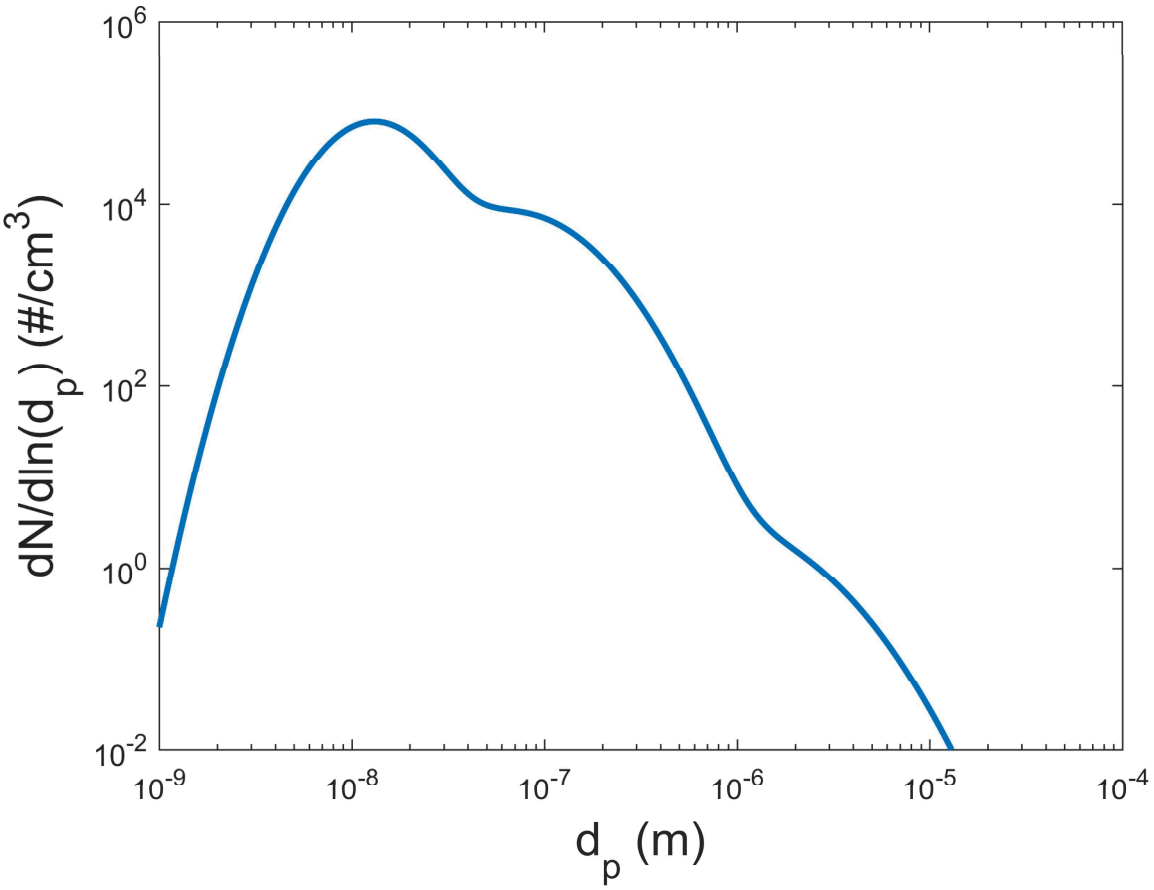

Figure 33. Aerosol number distribution plotted against particle size for "standard" atmospheric aerosol parameters taken from Whitby and Sverdrup (1980).

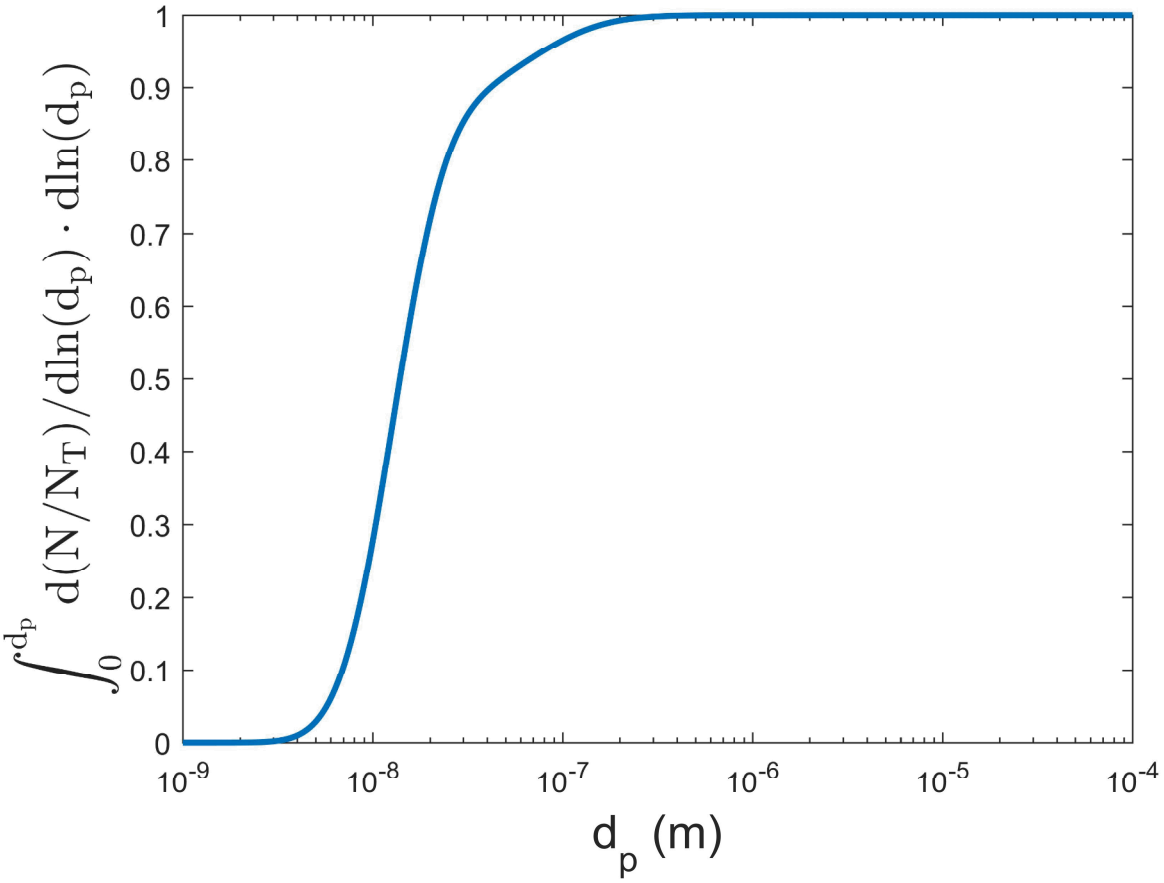

Figure 34. Cumulative aerosol number distribution plotted against particle size for "standard" atmospheric aerosol parameters taken from Whitby and Sverdrup (1980). Ordinate (y-axis) values can be interpreted as the percent of the total number of particles in the aerosol distribution with sizes less than the abscissa value (d_p). Greater than 95% of the particles, by number, have particle diameters less than 100 nm.

The surface area distribution of average atmospheric aerosol is shown in Figure 35. The shape of the $dS/d\ln(d_p)$ curve is different from the $dN/d\ln(d_p)$ because it is the second moment of $dN/d\ln(d_p)$ where the surface area of larger particles grows to the second power of particle diameter. The cumulative surface area distribution is shown in Figure 36. Very little particle surface area resides with particles smaller than 10 nm, and nearly all particle surface area resides with particles smaller than 10 µm.

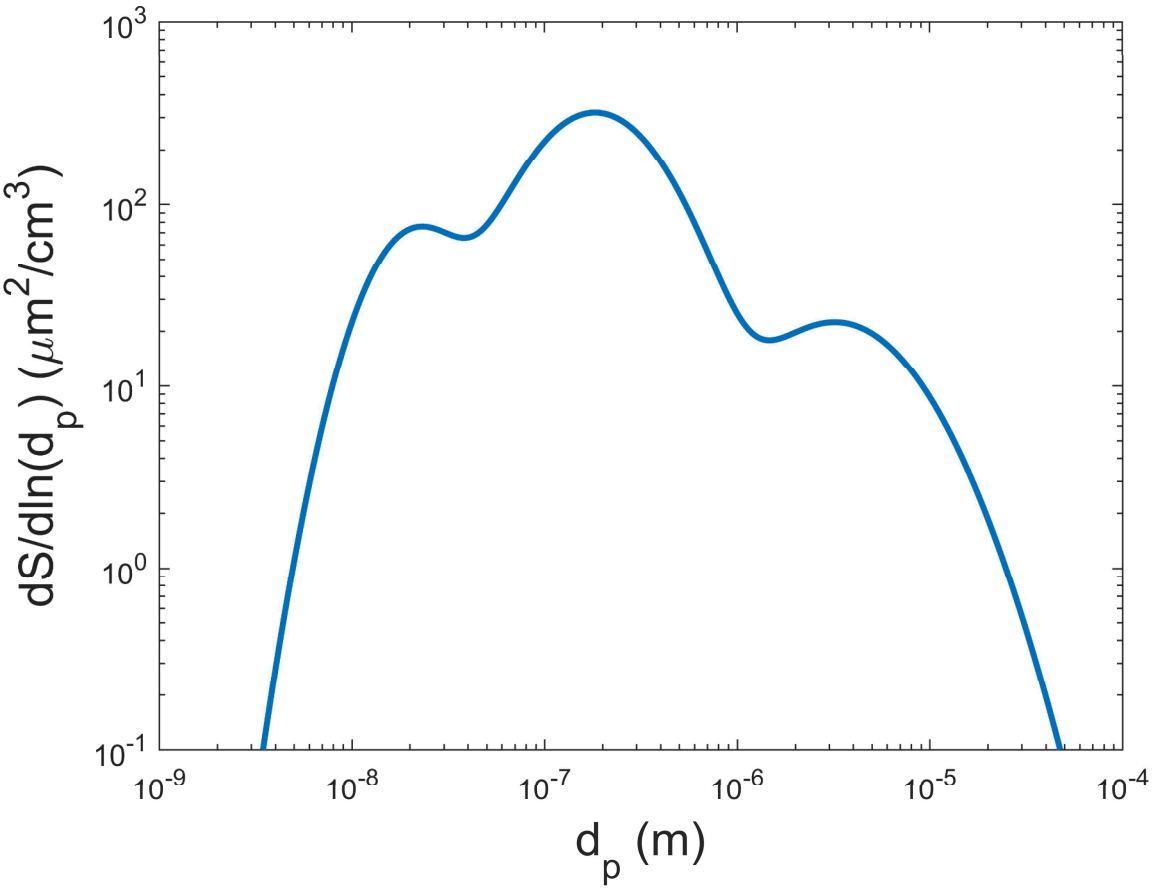

Figure 35. Aerosol surface area distribution plotted against particle size for "standard" atmospheric aerosol parameters taken from Whitby and Sverdrup (1980).

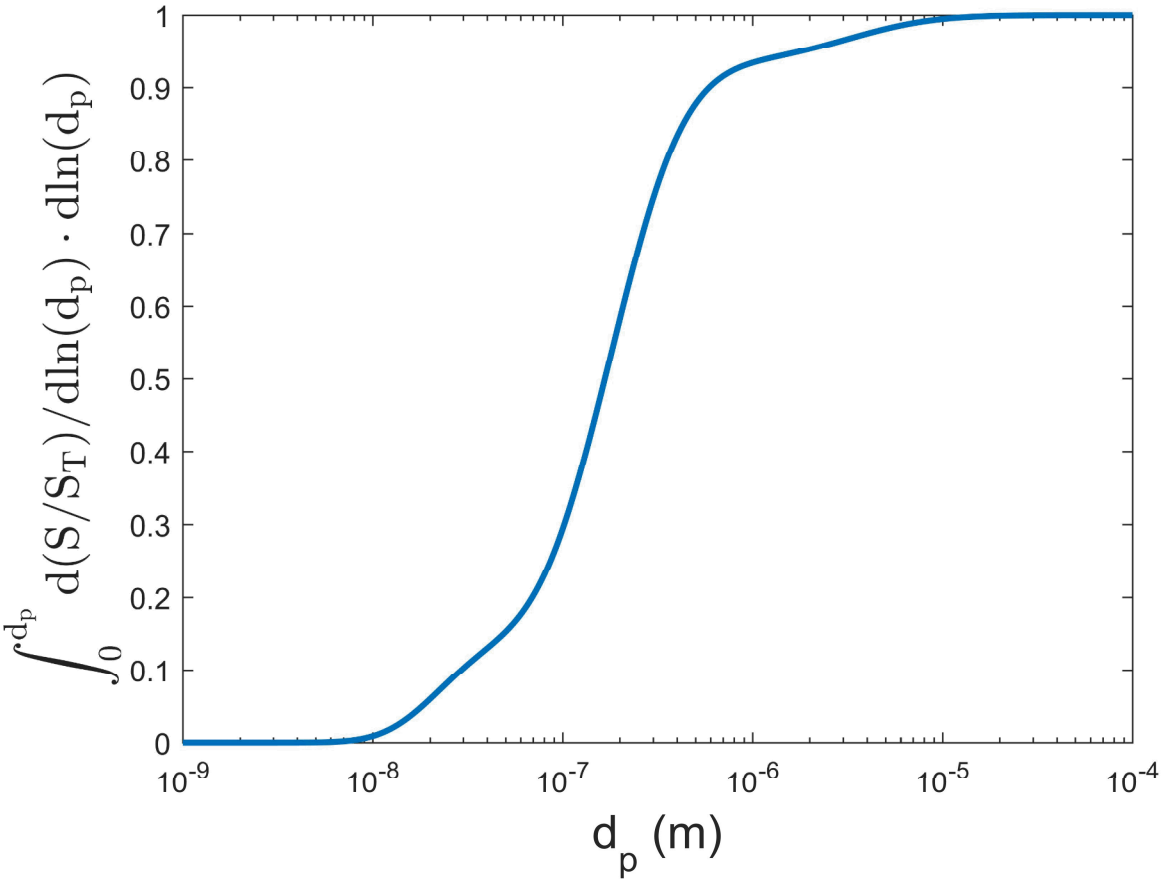

Figure 36. Cumulative aerosol surface area distribution plotted against particle size for "standard" atmospheric aerosol parameters taken from Whitby and Sverdrup (1980). Ordinate (y-axis) values can be interpreted as the percent of the total surface area of particles in the aerosol distribution with sizes less than the abscissa value (d_p).

The weighting function, $w_s(d_p)$, needed to calculate an average weighted aerosol collection efficiency can be formulated from $dS / d\ln(d_p)$. The total surface area concentration for the model aerosol is given by

$$S_T = \int_0^\infty \frac{dS}{d\ln(d_p)} d\ln(d_p) \quad . \tag{17}$$

The weighting function is then given by

$$w_s(\ln(d_p)) = \frac{d(S/S_T)}{d\ln(d_p)} \quad . \tag{18}$$

The integral of equation (17) is equal to one. The weighting functions of the number and surface area size distributions are shown in Figure 37. It is apparent that the weighting functions for the surface area and number distributions are significantly different. By number, Aitken mode particles are the most prevalent in the atmosphere. However, due to the influence of the second moment of particle diameter, the surface area weighting function shifts to larger particles. If one were to focus on particle number rather than surface area, the average weighted aerosol collection efficiency would be primarily influenced by the collection efficiency curve between 10 nm and 100 nm. Since we focus on particle surface area, the average weighted aerosol collection efficiency is influenced by the range of aerosol collection efficiencies between particle diameters of 10 nm and approximately 10 μm.

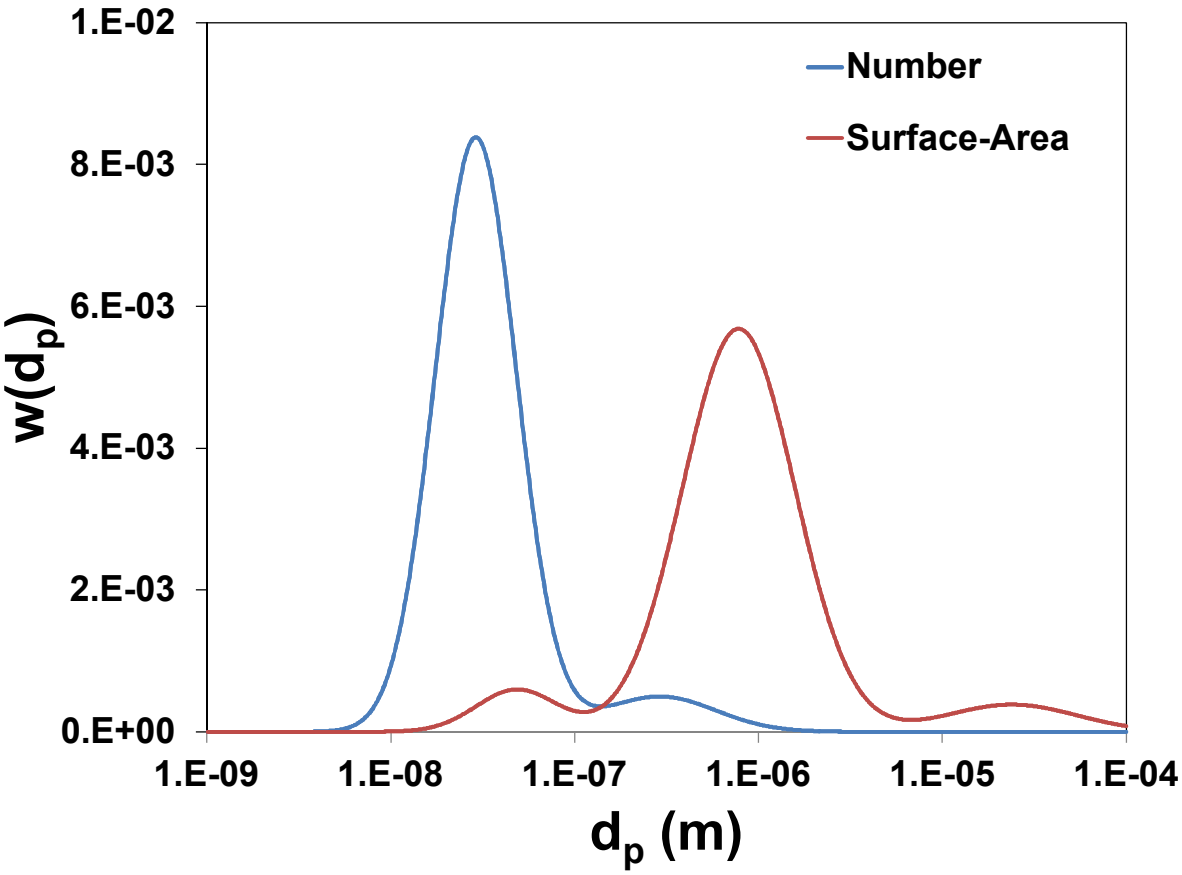

Figure 37. Mathematical weighting function for aerosol collection efficiency based on atmospheric aerosol number and surface area distributions.

The weighted average aerosol collection efficiencies for laboratory-scale filtration tests are given below. These averages were calculated according to the following equation:

$$\hat{E} = \int_0^\infty w_s(\ln(d_p))E(\ln(d_p))d\ln(d_p)\,. \qquad (19)$$

Weighted aerosol collection efficiencies are given in Table 18.

Table 18. Weighted aerosol collection efficiencies for FM1, FM2, and FM3 for filter face velocities of 1.1, 2.75, and 5.5 m/s, and particle charge states of negative, positive, and neutral.

		Ê (weighted efficiency)		
Particle charge	U (m/s)	FM1	FM2	FM3
negative corona (qp-)	1.1	1.00	1.00	1.00
	2.75	1.00	1.00	0.98
	5.5	0.99	0.97	0.91
Neutral (qp.boltz)	1.1	0.98	0.94	0.65
	2.75	0.97	0.92	0.64
	5.5	0.98	0.87	0.69
positive corona (qp+)	1.1	1.00	1.00	0.99
	2.75	1.00	1.00	0.94
	5.5	1.00	0.98	0.84

4.2 Electrostatic effects

The effects of space charge on laboratory-scale and mid-scale filtration tests were analyzed to determine if the particle-pre-charging approach is feasible for full-scale RASA radionuclide collectors. This analysis was prompted by an observation in laboratory scale testing. Figure 38 shows the aerosol number concentration as a function of electrical mobility diameter (d_m) for NaCl aerosol generated with the TSI Constant Output Analyzer with multiple electrostatic charge distributions: (1) Boltzmann equilibrium charge distribution (uncharged), (2) positive charge distribution, and (3) negative charge distribution. The positive and negative charge distributions were imparted through the use of the SIMCO Ionizers. The concentration of negatively charged particles was roughly 1/3 of the uncharged distribution. The positively charged aerosol was approximately 60% of the original distribution. We see from laboratory scale experiments that highly charged particles are more efficiently captured by electrostatic filter media. However, if particle-pre-charging results in particle losses, efficiency improvements are offset by inefficiencies in charged particle transport within the system. For particle-pre-charging to be a viable option for the RASA we must understand if particle losses were an artifact of the particle-pre-charging apparatus and if we would expect to see similar losses in fielded RASA systems if particle-pre-charging were employed.

Coronas are generated when free electrons are accelerated in a high electric field, collide with molecules, and eject additional electrons leaving behind positively charged molecules. Those molecules may then migrate toward aerosol particles and attach to form charged aerosol particles. In our experiments, we varied the current control on the ion generators to provide the maximum current possible with these ionizers. The ionizer power supply adjusted the setpoint voltage (limit of ±30 kV) to achieve the desired current (limit of approximately ±0.25 mA). Negative coronas (negative potential) require the surrounding gas to contain species that can absorb free electrons whereas the positive corona does not (Baron and Willeke 2001). For experiments where a negative corona was used, the SIMCO ionizer power supply had typical values of -20 kV and 0.25 mA. These values were within 20% for the positive corona and exhibited variability from day to day. It is difficult to conclude from these data points why the negative corona charged particles would have approximately one half the number concentration of the positive corona charged particles. If one corona polarity required a substantially different field strength to achieve a current of 0.25 mA, that could plausibly effect the aerosol

concentration but that does not appear to be the case. Electrons, negative air ions, and positive air ions have different electrical mobilities: 6.7e-2, 1.6e-4, and 1.4 e-4 m^2 V^{-1} s^{-1}, respectively (Hinds 1999). Ion-particle attachment factors also vary. Thus, it is not clear why the resultant charge state is substantially different for the positive and negative polarity corona but many factors are likely to contribute to the net result. Laboratory-scale filtration tests show that aerosol particles charged in a negative corona are captured more efficiently by FM3. Negatively charged coronas were used in mid-scale filtration testing.

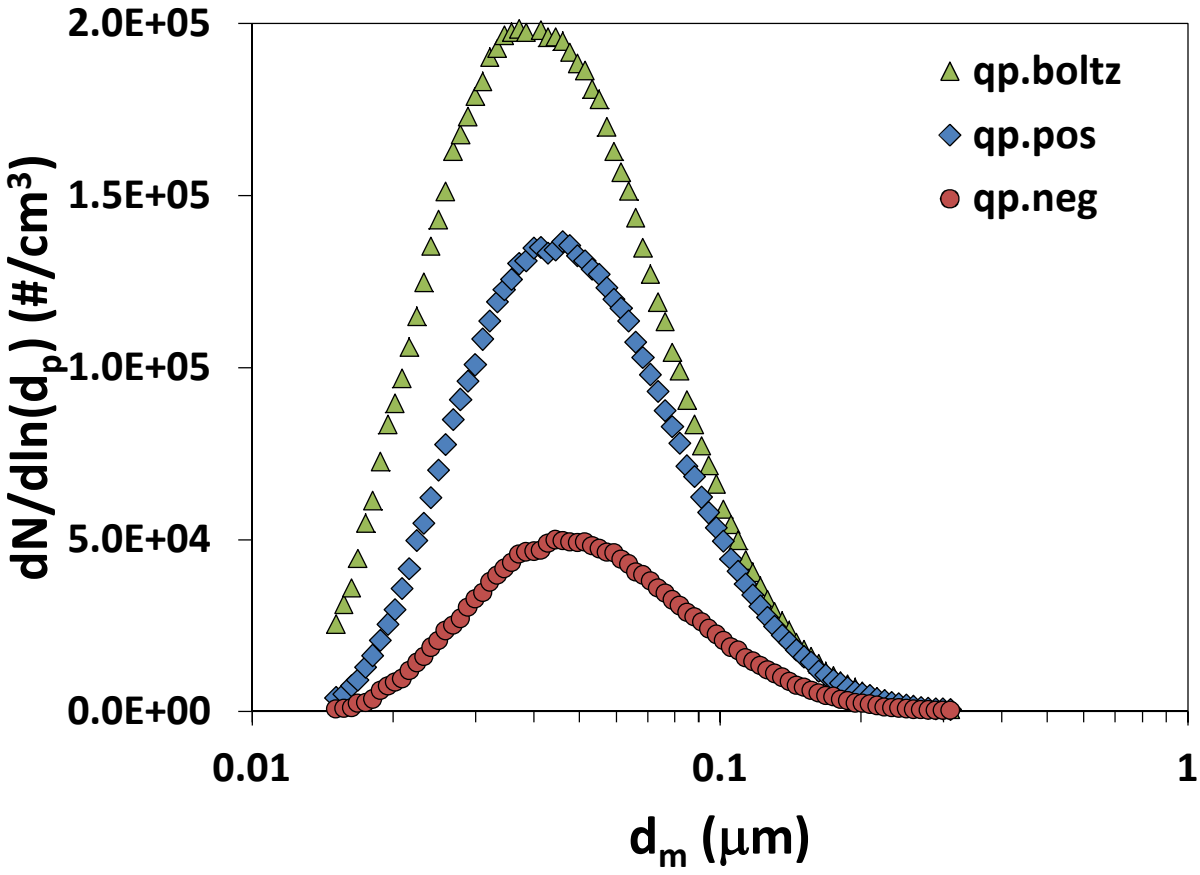

Figure 38. Aerosol number concentration for NaCl test aerosol in laboratory scale system. Data are given for uncharged aerosol, positively charged aerosol, and negatively charged aerosol.

The ratios of charged aerosol concentration with respect to uncharged aerosol concentration were plotted in Figure 39. Smaller particles have higher mobilities so we would expect to see more particle losses for small particles with respect to large particles. The ratio of aerosol concentration should approach the asymptotic limit of one as particle size gets very large.

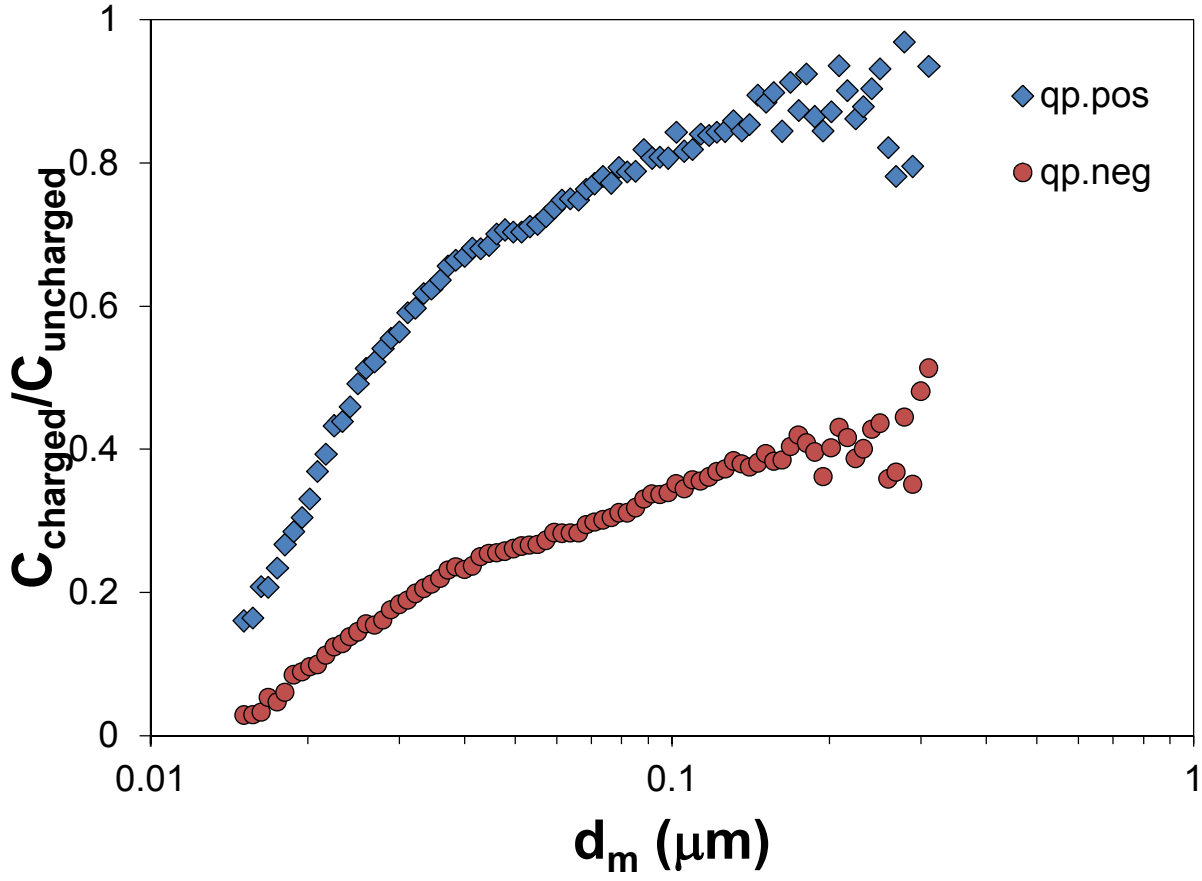

Figure 39. Ratio of charged to uncharged particle concentration for positively, and negatively, charged NaCl test aerosol particles in the laboratory scale test system.

Laboratory-scale data shows there was an effect of particle-pre-charging on aerosol concentration downstream of the ionizer. This effect could be attributed to (1) space charge, (2) high electric fields in the vicinity of the corona ionizers, or (3) sampling losses in ¼" tubing used in laboratory and mid-scale testing but are not used in the RASA.

4.2.1 Space charge effect

A cloud of electrostatically charged aerosol particles creates its own electric field. This is called the space charge effect. Charged aerosol particles within the electric field experience body forces which affect their trajectories. Within an enclosure, charged aerosol particles will drive themselves to the surrounding walls. In the RASA, this would be an unacceptable consequence as it would reduce the overall collection efficiency. The purpose of this analysis is to understand whether space charge is responsible for particle losses observed in laboratory-scale testing and if we think this could be engineered out of a full-scale RASA.

The space charge phenomena is governed by the Poisson equation where the electric potential, φ, is given by

$$\nabla^2\varphi = -\frac{\rho}{\varepsilon_0} \tag{1}$$

where, φ is measured in volts, ε_0 is the permittivity of free space (8.85e-12 C^2/Nm^2), and ρ is the space charge density (C/m^3). For regions without space charge the Poisson equation simplifies to the Laplace equation where boundary conditions determine the electric potential. Boundary conditions can be specified for the Laplace equation as the first or second kind, $\varphi = V$ and $\nabla\varphi = -\sigma / \varepsilon_0$, respectively, where V is a defined voltage (often ground) and σ is surface charge density (Griffiths 1999).

The electric field ($\vec{E}$) is then calculated as the gradient of the scalar potential,

$$\vec{E} = -\nabla\varphi\,. \tag{1}$$

The electric field then specifies the electrostatic body force ($\vec{F}_e$) on each particle,

$$\vec{F}_e = q\vec{E} = ne\vec{E}\,, \tag{2}$$

where q is particle charge (C), or n is the number of units of elementary charge (e =1.6e-19 C). The additional body force alters particle trajectories by changing the overall force balance ($\vec{F}_p$) on each particle as it travels. More particles are driven to the walls of the cylinder and deposit locally.

$$\sum \vec{F}_p = m_p\vec{a}_p\,. \tag{3}$$

4.2.2 Analysis

4.2.2.1 Diffusion charging

Electrostatic particle charging is well documented in the literature (e.g., Hinds 1999; Baron and Willeke 2001). In the presence of ions, aerosol particles will acquire charge through the diffusion of ions to the particle surface. This process can be described by the following:

$$n_{diff}(\tau) = \frac{d_p kT}{2K_E e^2} \cdot \ln\left[1 + \frac{\pi K_E d_p \bar{c}_i e^2 N_i \tau}{2kT}\right] \tag{20}$$

where symbol definitions are given below.

n_{diff}	Number of particle charges acquired through diffusion charging mechanism (unitless)
d_p	Particle diameter (m)
k	Boltzmann constant, $1.38 \cdot 10^{-23}$ (N m K^{-1})
τ	Time (s)
T	Temperature (K)
K_E	Constant of proportionality, $1/4\pi\varepsilon_0 = 9 \cdot 10^9$ (N m^2 C^{-2})
e	Charge on an electron, 1.6e-19 C
$\bar{c}_i$	Mean thermal speed of ions, 240 (m s^{-1})
$N_i t$	Product of ion concentration (m^{-3}) and diffusion charging time (s)

4.2.2.2 Field Charging

In the presence of an electric field, ions are driven to the surface rather than diffuse. The field charging relationship is given by the following:

$$n_{field}(\tau) = \left(\frac{3\varepsilon}{\varepsilon + 2}\right) \cdot \left(\frac{E d_p^{\,2}}{4K_E e}\right) \cdot \left(\frac{\pi K_E e Z_i N_i \tau}{1 + \pi K_E e Z_i N_i \tau}\right) \tag{21}$$

where symbol definitions are given below.

n_{field}	Number of particle charges acquired through electric field charging mechanism (unitless)
ε	Relative permittivity of particle, $\varepsilon = 3.9$ for silicon dioxide
E	Electric field strength (V m^{-1})
Z_i	Ion mobility, 0.00015 (m^2 V^{-1})

4.2.2.3 Charge limit

Diffusion and field charge mechanisms can act additively but particle charge has a theoretical limit where charges will repel themselves if too closely spaced on the surface of a particle. The particle charging limit is given by

$$n_{lim} = \frac{d_p{}^2 E_L}{4 K_E e} \tag{22}$$

where symbol definitions are given below.

n_{lim}	Theoretical limit to number of particle charges acquired (unitless)
E_L	Surface field strength required for spontaneous emission of electrons (9.0e-8 V m^{-1})

4.2.2.4 Analysis

Estimates for parameters which affect particle charging and charged particle transport are given in Table 19 for the laboratory-scale and mid-scale test apparatus as well as ¼" aerosol sampling tubes used to transport aerosols from those setups to the instruments used to measure particle size and aerosol concentration.

Table 19. Estimated and measured parameters used to calculate particle charge for laboratory and mid-scale filtration tests

Experiment	Parameter	Value	Units
Laboratory Scale	Q	1.8e-3	$m^3\ s^{-1}$
	A	1.6e-3	m^2
	$U = Q / A$	1.1	$m\ s^{-1}$
	N_i	1.7e+18	m^{-3}
	$\tau = \Delta x / U$	5.0e-2	s
	$N_i\tau$	8.5e16	$s\ m^{-3}$
	E field	4.4e05	$V\ m^{-1}$
Mid-scale	Q	7.2e-3	$m^3\ s^{-1}$
	A	9.9e-2	m^2
	$U = Q / A$	7.3e-2	$m\ s^{-1}$
	N_i	8.7e17	m^{-3}
	$\tau = \Delta x / U$	0.7	s
	$N_i\tau$	6.1e17	$s\ m^{-3}$
	E field	5.6e4	$V\ m^{-1}$
Aerosol sampling tube	Q	1.7e-5	$m^3\ s^{-1}$
	A	1.1e-5	m^2
	$U = Q / A$	1.5	$m\ s^{-1}$
	N_i	8.7e17	m^{-3}
	$\tau = \Delta x / U$	0.7	s
	$N_i\tau$	6.1e17	$s\ m^{-3}$
	E field	0	$V\ m^{-1}$

Diffusion and field particle charging were estimated for laboratory-scale and mid-scale testing and are shown in Figure 40. Field charging is typically dominant for larger particles (>1 μm) which is seen in the chart.

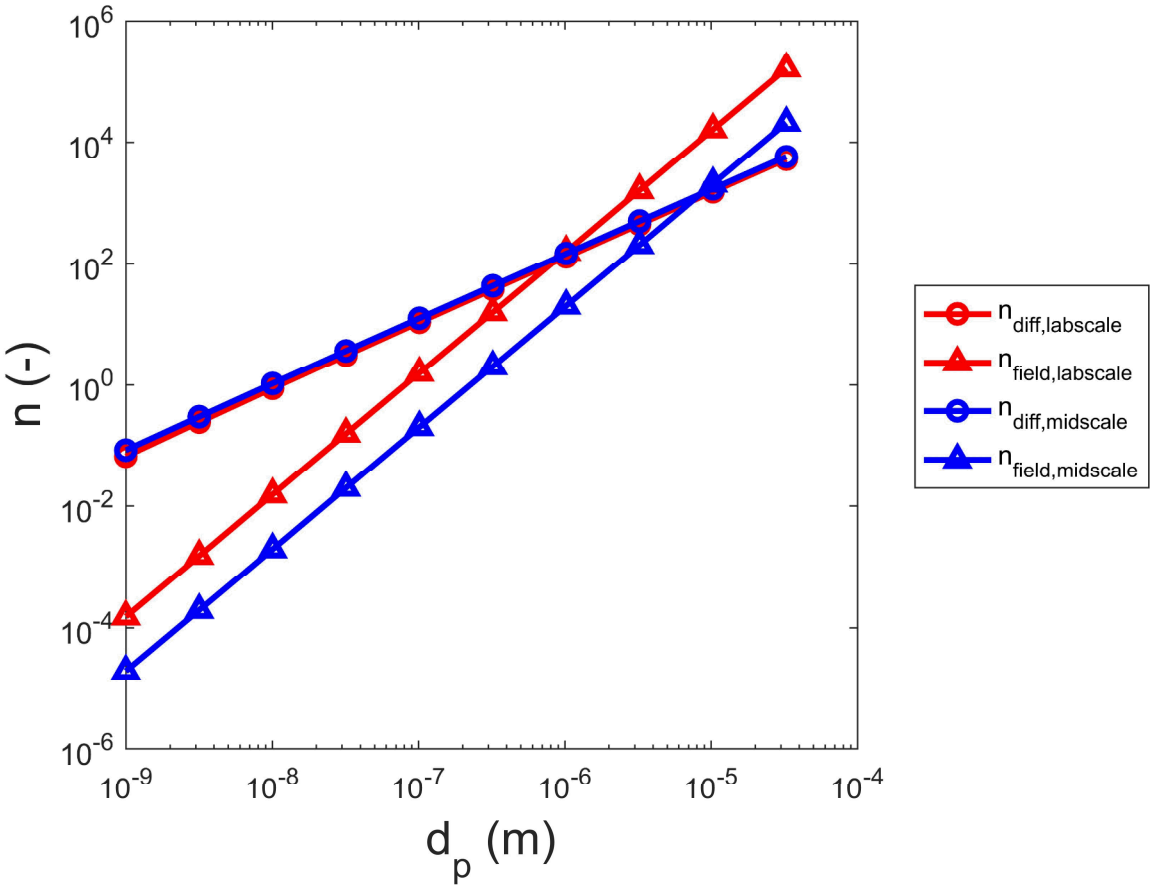

Figure 40. Particle charge associated with diffusion and field charging mechanisms for laboratory scale tests and mid-scale tests

The combined diffusion and field charge levels are compared to the theoretical maximum charge in Figure 41. The estimated charge levels are 1-2 orders of magnitude less than the theoretical limit. However, it would be difficult to engineer a system with the electric field strength and charging parameter $N_i t$ to achieve the theoretical limit without substantial particle losses.

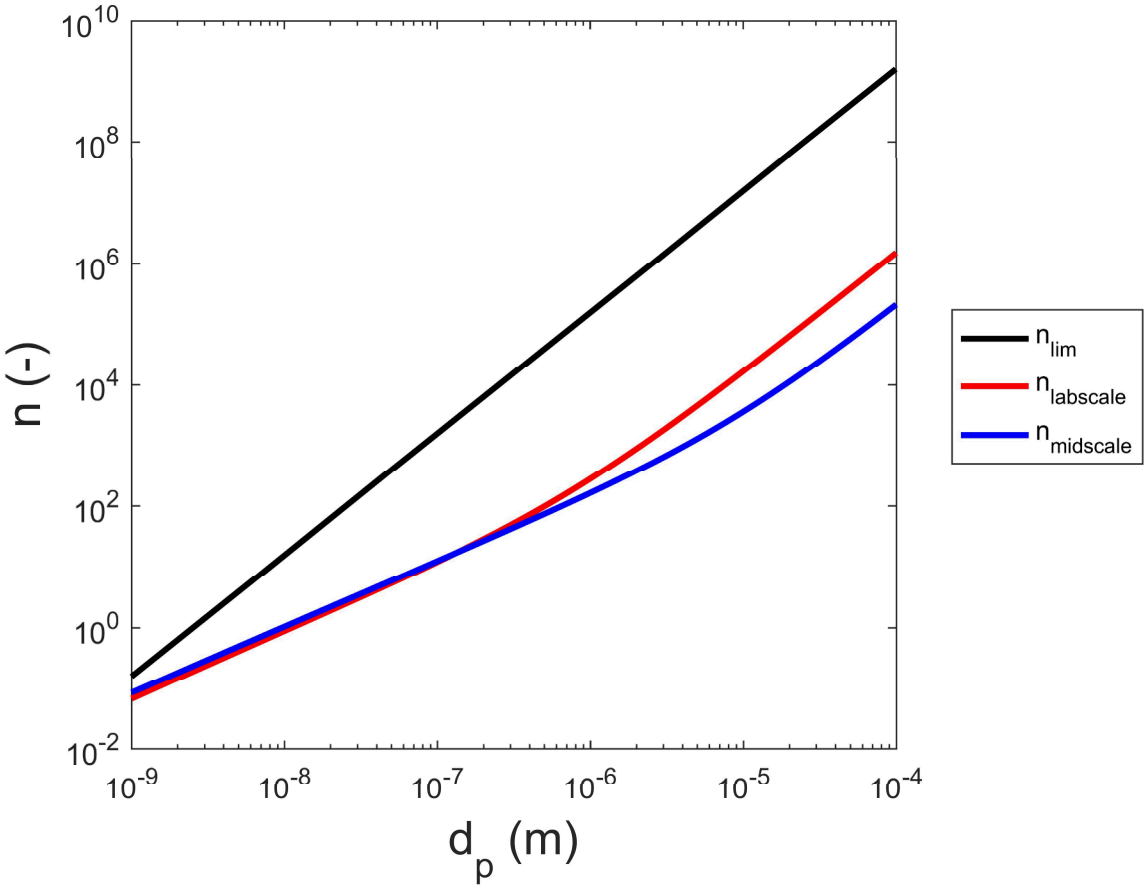

Figure 41. Combined particle charge for laboratory scale tests and mid-scale tests compared to theoretical particle charge limit

The NaCl aerosol size distribution (laboratory-scale testing) is compared to the average ambient aerosol size distribution in Figure 42 for frame of reference. The NaCl distribution is more narrow than the ambient aerosol distribution. Both distributions are used to assess particle losses in laboratory-scale tests and projected losses in the full-scale RASA.

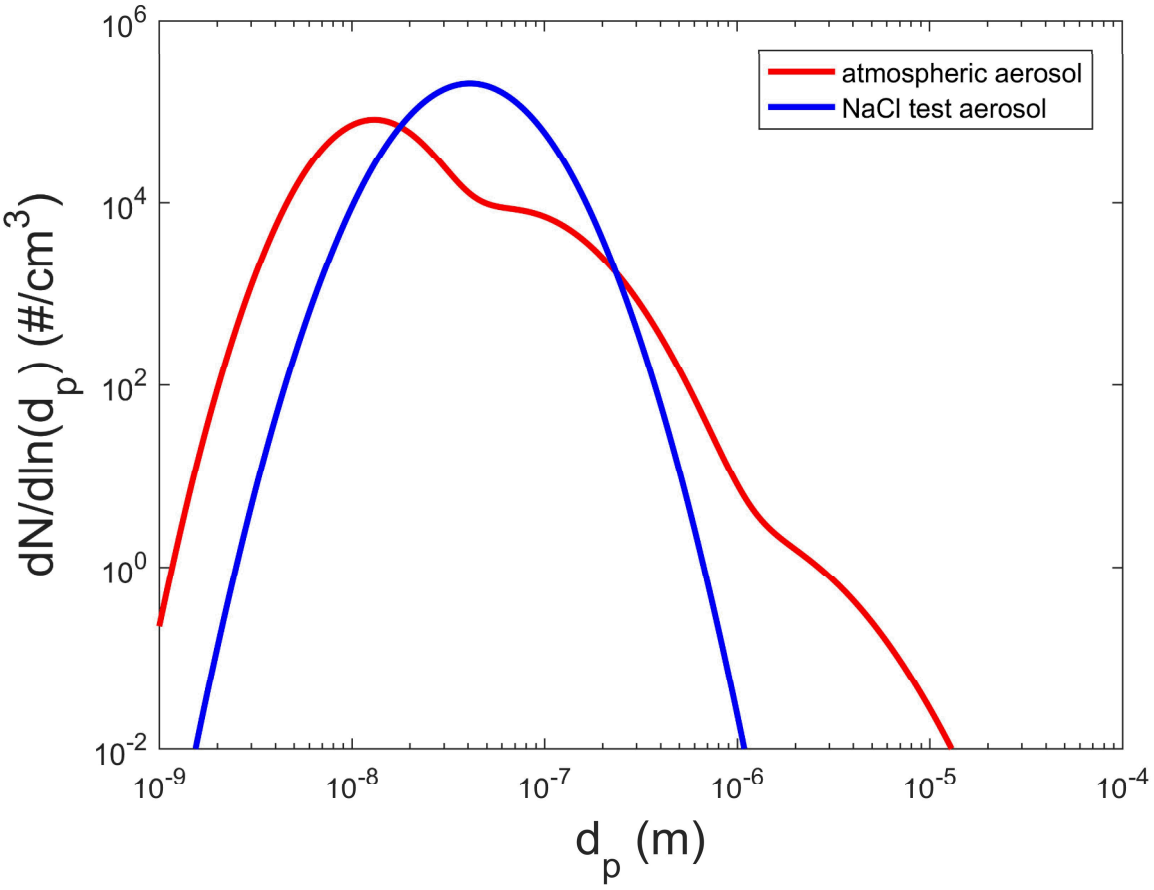

Figure 42. Aerosol number distribution for NaCl aerosol used in laboratory experiments. Data fitted with lognormal distribution.

The electric field strengths due to space charging, and due to the presence of the high voltage ionizer tips, are shown in Figure 43. This figure shows us an important result. In laboratory-scale and mid-scale testing, the electric field strengths due to the space charge effect are nearly three orders of magnitude lower than the electric field strengths due to the presence of high voltage ionizer tips within an electrically grounded enclosure. Both electric fields will cause charged aerosol particles to migrate to the walls of the enclosure. However, from this analysis we conclude that we are likely creating significant particle losses in the region close to the ionizer tips where the electric field strength is high. Engineering solutions may be obtainable to eliminate this component of the electric field and mitigate particle losses that were observed in laboratory-scale testing.

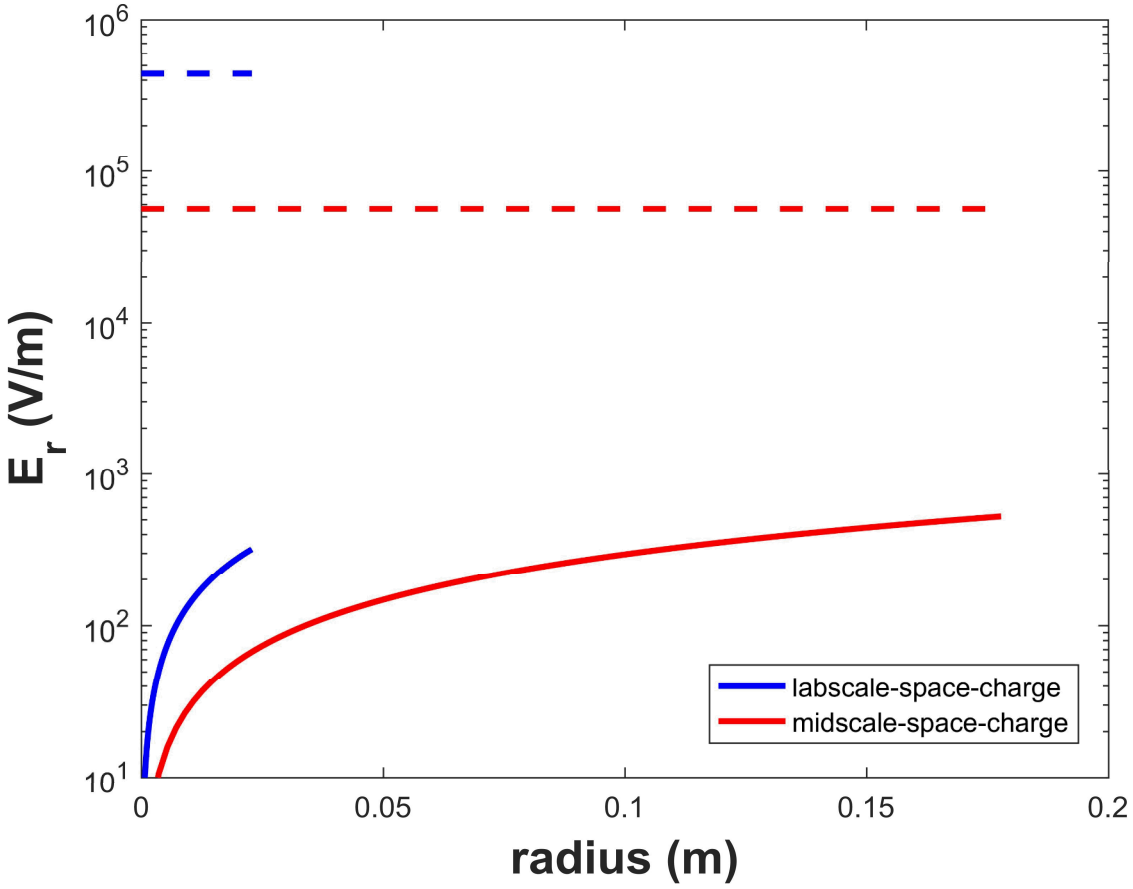

Figure 43. Radial component of electric field inside pipe due to space charge effect

Estimated electrostatic migration velocities are shown Figure 44 along with gravitational settling velocity for particles with a density of 2.3 g cm^{-3} (silicon dioxide). This assumes the field strengths shown in Figure 43 and particle charges shown in Figure 41. Electrostatic migration velocities are significant for particles between 1-10 nanometers. The electrostatic migration velocities become less significant beyond approximately 100 nm.

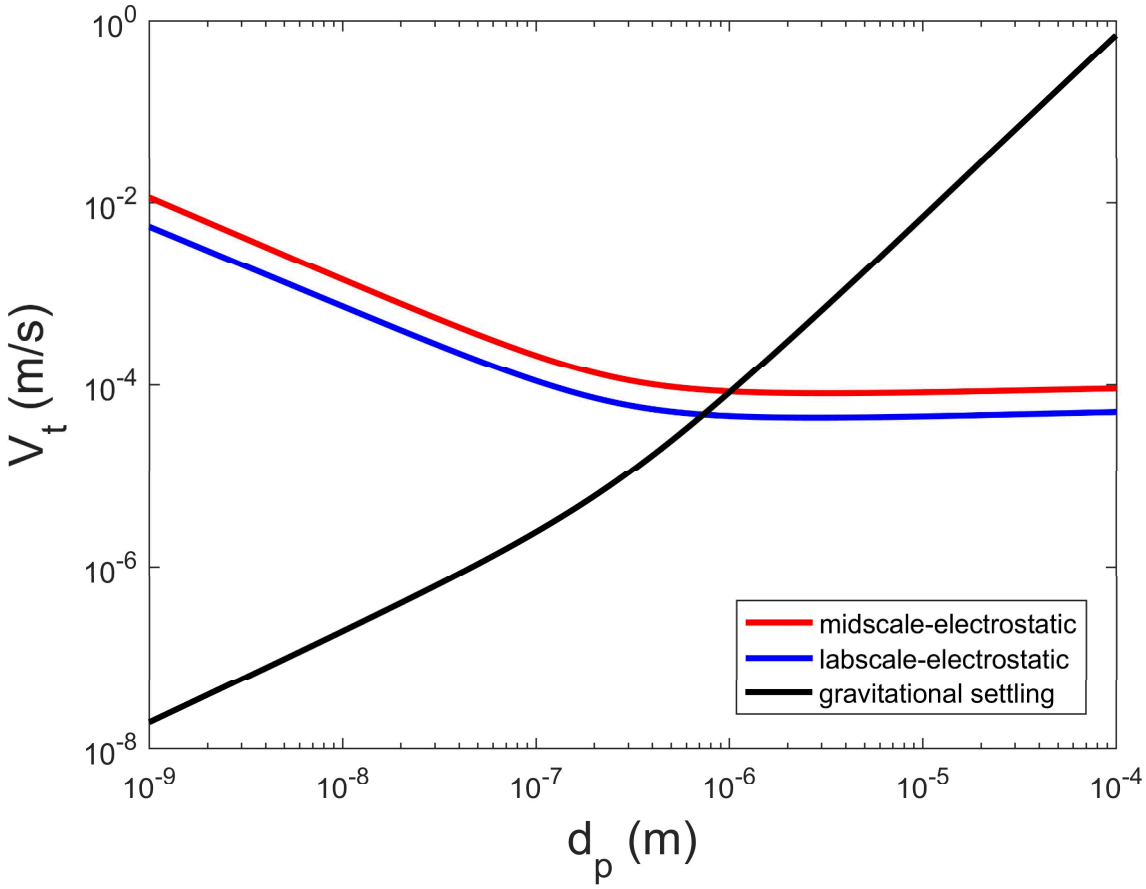

Figure 44. Estimated terminal electrostatic migration velocities for mid-scale and laboratory-scale testing, along with gravitational settling velocity of particles with density of 2300 kg m^{-3}.

Several approximations were used to estimate the penetration of charged particles through test systems. As a first-order estimate, the Deutsch-Anderson equation was used to assess the penetration of charged particles:

$$P = \exp\left(\frac{-V_{te} 2\pi RL}{Q}\right). \tag{23}$$

In (23), the electrostatic migration velocity, V_{te}, was calculated with the space charge electrostatic field at the wall of the tube (mid-scale, lab-scale, or sampling tube). This equation was intended for use with wire-and-tube electrostatic precipitators.

A more accurate approximation was derived by Yu (1977) where a dimensionless time constant was derived for the flow of charged particles through tubes:

$$t_j^* = B_j q_j \frac{n_0 q_{tot}}{\varepsilon_0} \tag{24}$$

where $B_j q_j$ represents the mechanical mobility of particle size j and electrostatic charge of particle size j, and $\frac{n_0 q_{tot}}{\varepsilon_0}$ is the total concentration of particles (n_0) at the entrance multiplied by the total charge of the aerosol (q_{tot}) divided by the relative permittivity. The first factor in (24) comes from the transport of charged particles within an electrical field. The second factor gives the electrical field due to the ensemble of charges. The penetration of particle size j, P_j, is given by the following:

$$P_j = \frac{t_j^*}{1 + t_j^*} \ . \tag{25}$$

Equations (23) and (25) were used to estimate the penetration efficiencies through the (1) laboratory-scale test system, (2) the mid-scale test system, and (3) the ¼" sampling tube used to transport aerosols from the test system to aerosol measurement instruments. Estimates are shown in Figure 45. The cumulative surface area distribution is also given. Below 10 nm, very little surface area is present in the aerosol size distribution. Above 10 nm, the projected penetration of particles is approximately 95%.

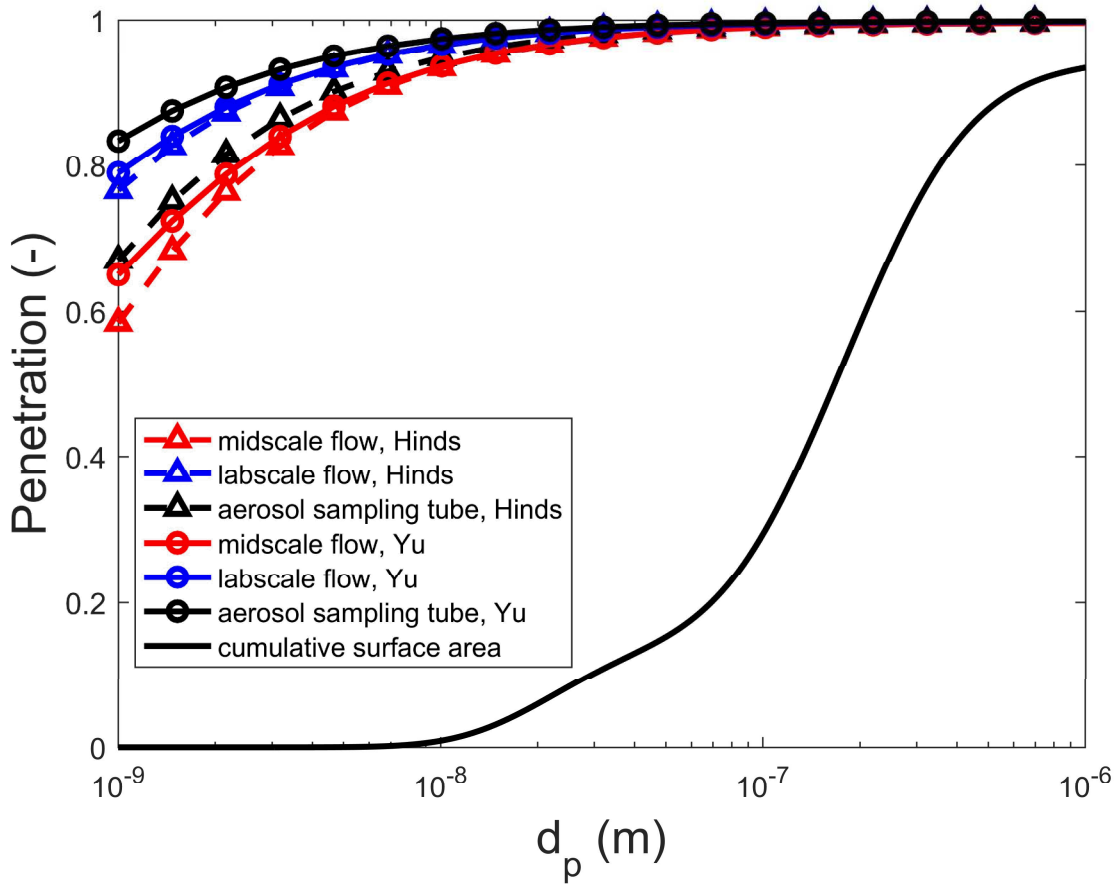

Figure 45. Charged particle penetration through laboratory-scale tubing (2" OD), mid-scale test inlet (14" OD), and aerosol sampling tubing (1/4" OD) along with cumulative surface area distribution for atmospheric aerosol.

Based on these estimates, we believe particle-pre-charging could be achieved with minimal aerosol transport losses in the full-scale RASA. Two approaches would be used to mitigate transport losses: (1) reduce the electric field strength generated between the ionizer tip and grounded sample inlet, and (2) minimize the time of travel between the particle-pre-charging and particle collection (filter) components of the RASA. These results also suggest the particle losses in laboratory-scale testing were attributable to losses in the immediate vicinity of the ionizing tips where high electric fields exist.

5 RECOMMENDATIONS

Ten RASA configurations are given in Table 20. The air flow rate, filter face velocity, and filter pressure drop are given in absolute values as well as relative values compared to the current RASA configuration. Weighted aerosol collection efficiencies are also given from laboratory-scale testing where collection efficiency curves were weighted by the atmospheric aerosol surface area distribution. Relative MDC values were calculated assuming the lower limit of detection scales with air flow rate. This assumption was supported by mid-scale test results. Engineering requirements and motivations are also given for each configuration.

5.1 FM1, baseline, standard flow

This is the current RASA configuration, or the baseline from which all alternate configurations were compared.

5.2 FM1, particle pre-charging, standard flow

A marginal reduction in MDC could be obtained by pre-charging particles that enter the RASA system. The calculated MDC ratio (MDC/MDC_0) is within experimental uncertainties. This configuration is not recommended since FM1 performs well without particle-pre-charging.

5.3 FM2, no particle pre-charging, standard flow

FM2 could be used as the filtration material, at the current RASA air flow rate, to reduce system pressure drop and potentially reduce power consumption. Power savings were not calculated but the ratio of pressure drop, with respect to the baseline, would be approximately 70%. This approach could be applied without changing the RASA blower and blower motor. We recommend GD quantify the maximum air flow rate achievable with the current RASA motor and blower configuration with FM2 as the filter material. A good estimate (±25%) of baseline sensitivity reduction could be calculated based on air flow measurements alone. If power savings is the driver, it may be preferable to explore motor changes to optimize the coupling between the blower and filter.

Table 20. Recommended RASA configurations for power savings and reduction of minimum detectable concentration (MDC)

		Recommended Configuration									
		1	2	3	4	5	6	7	8	9	10
Category	Metric	FM1		FM2						FM3	
Flow	Q (m^3/day)	47,520	47,520	47,520	47,520	51,840	51,840	118,800	118,800	47,520	118,800
	U (m/s)	1.1	1.1	1.1	1.1	1.2	1.2	2.75	2.75	1.1	2.75
	U/U_0	1.0	1.0	1.0	1.0	1.1	1.1	2.5	2.5	1.0	2.5
	ΔP_f (psid)	0.24	0.24	0.17	0.17	0.19	0.19	0.48	0.48	0.05	0.18
	$\Delta P/\Delta P_0$	1	1	0.72	0.72	0.79	0.79	1.99	1.99	0.22	0.73
Aerosol collection efficiency	η	0.97	1.00	0.98	1.00	0.98	1.00	0.98	1.00	0.99	0.97
	η/η_0	1.00	1.03	1.01	1.03	1.01	1.03	1.01	1.03	1.02	1.00
Minimum detectable concentration	LD/LD_0	1.00	1.00	1.00	1.00	1.04	1.04	1.58	1.58	1.00	1.58
	MDC/MDC_0	1.00	0.97	0.99	0.97	0.94	0.92	0.63	0.61	0.98	0.63
Engineering	Electrostatic mods	No	Yes	No	Yes	No	Yes	No	Yes	Yes	Yes
	Blower mods	No	No	No	No	No	No	Yes	Yes	No or yes	No or yes
	Motivation	Status quo	Increase collection efficiency 5-10% below 100 nm	~70% of pressure drop of current material, save power	~70% of pressure drop of current material, save power	Use current blower to get an additional ~10% flow	Use current blower to get an additional ~10% flow	Higher sensitivity at 24 hours, 2-12 hour samples	Higher sensitivity at 24 hours, 2-12 hour samples	Save power	Higher sensitivity at 24 hours, 2-12 hour samples, power savings

5.4 FM2, particle pre-charging, standard flow

FM2 could be used with particle pre-charging. In this configuration, power savings would again the primary driver. The MDC ratio would be marginally lower than the baseline but within experimental uncertainty. The slight reduction in baseline sensitivity is likely not worth the effort of implementing particle-pre-charging in this configuration.

5.5 FM2, no particle pre-charging, marginally increased flow

We hypothesize that the current RASA blower and motor could be adjusted to provide a marginal increase in air flow if FM2 were used (10-20%). This is difficult to quantify based on the blower curve alone and we suggest that General Dynamics measure the flow rate achievable with FM2 and the current RASA blower and blower motor. The objective of this configuration would be to drive the MDC down to approximately 95% of the current value to ensure the RASA meets technical specifications for baseline sensitivity of 10 μBq m^{-3}. We recommend this for consideration although 10-15% reduction in MDC would be preferable. Values presented in the table are estimates. A 10% increase in air flow was assumed but it could be higher. Air flow measurements are needed. Our assessment of the current blower is that it is very close to its maximum capacity. A significant increase in air flow is unlikely.

5.6 FM2, particle pre-charging, marginally increased flow

Similar to configuration 5, FM2, with particle pre-charging, could be used with the current blower and motor with marginally increased air flow to drive the MDC down to approximately 90% of its current value. Again, an increase in air flow of 10% was used here in the absence of measured values on an actual RASA with FM2. We recommend this configuration for consideration although the transport of charged particles within the RASA system should be conceptually engineered prior to any major investment.

5.7 FM2, no particle pre-charging, 2.5x flow

At 2.5 times the baseline flow, the MDC could be driven down to approximately 63% of its current value. Mid-scale tests show that value should be closer to 55-60%. However, this approach would have twice the pressure drop of the baseline configuration. Power consumption would increase and the blower motor would likely need to be sized appropriately (7.5 HP) to achieve this flow rate.

5.8 FM2, particle pre-charging, 2.5x flow

With particle pre-charging, FM2 could be used at 2.5 times the baseline flow. However, the benefit of particle-pre-charging is marginal with respect to particles which have not been pre-charged in this configuration.

5.9 FM3, particle pre-charging, standard flow

FM3 could be used at the baseline flow at approximately 22% of the baseline pressure drop. This could result in significant power savings but would require the use of particle pre-charging. We recommend this for consideration based on potential energy savings and a reduction in blower size required to sample the current volume of air. The reduction in baseline sensitivity may be closer to 55-60% of its current value based on results from mid-scale tests.

5.10 FM3, particle pre-charging, 2.5x flow

FM3 could be used at 2.5 times the baseline flow. With a pressure drop of approximately 73% of the baseline, energy savings may still be achieved while obtaining a MDC of 63% of the baseline value. We recommend this configuration for consideration. The reduction in baseline sensitivity may be closer to 55-60% of its current value based on results from mid-scale tests.

REFERENCES

Baron, P. A. and K. Willeke (2001). Aerosol measurement: principles, techniques, and applications. New York, Wiley.

Bowyer, S. M., D. C. Gerlach, H. S. Miley, S. L. Pratt, C. W. Thomas, J. F. Wacker and M. J. Kniedler (1998). "Radiochemistry of the SBMF filter media used by the DOE CTBT Radionuclide Aerosol Sampler/Analyzer (RASA)." Journal of Radioanalytical and Nuclear Chemistry 235(1-2): 121-124.

Commission, C. T. B. T. O. P. (2007). CERTIFICATION OF IMS PARTICULATE RADIONUCLIDE STATIONS. CTBT/PTS/INF.58/Rev.8. C. T. B. T. Organization.

Commission, C. T. B. T. O. P. (2010). OPERATIONAL MANUAL FOR RADIONUCLIDE MONITORING AND THE INTERNATIONAL EXCHANGE OF RADIONUCLIDE DATA. CTBT/WGB/TL- 11,17/18/Rev.5. C. T. B. T. Organization.

DeCarlo, P. F., J. G. Slowik, D. R. Worsnop, P. Davidovits and J. L. Jimenez (2004). "Particle morphology and density characterization by combined mobility and aerodynamic diameter measurements. Part 1: Theory." Aerosol Science and Technology 38(12): 1185-1205.

Dellinger, J. G., M. Kathleen Alam, John E. Brockman, Josh A. Hubbard, Laura E. Martin, Steve C. Chrisman, Kevin N. Austin, Peter J. Hotchkiss, Linda K. Jones (2009). Progress Report on the Method Development for Lifetime Prediction of IPC1478 Filter Paper. Albuquerque, New Mexico, Sandia National Laboratories.

Dellinger, J. G., M. Kathleen Alam, Josh A. Hubbard, Andres L. Sanchez, John E. Brockman, Laura E. Martin, Steve C. Chrisman, Kevin N. Austin, Peter J. Hotchkiss, Linda K. Jones (2012). Final Report on the Lifetime Prediction of IPC1478 Filter Paper and Storage Recommendations. Albuquerque, New Mexico, Sandia National Laboratories.

Endo, Y., D. R. Chen and D. Y. H. Pui (1998). "Effects of particle polydispersity and shape factor during dust cake loading on air filters." Powder Technology 98(3): 241-249.

Forrester, J. B., F. F. Carty, L. Comes, J. C. Hayes, H. S. Miley, S. J. Morris, M. Ripplinger, R. W. Slaugh and P. Van Davelaar (2013). "Engineering upgrades to the Radionuclide Aerosol Sampler/Analyzer for the CTBT International Monitoring System." Journal of Radioanalytical and Nuclear Chemistry 296(2): 1055-1060.

Hinds, W. C. (1999). Aerosol technology : properties, behavior, and measurement of airborne particles. New York, Wiley.

Hubbard, J. A., Andres L. Sanchez, Jennifer G. Dellinger, Daniel A. Lucero, and Brandon L. Servantes (2012a). Aerosol collection efficiency of electrostatic filter media used for verification of the Comprehensive Nuclear-Test-Ban Treaty. Albuquerque, New Mexico, Sandia National Laboratories.

Hubbard, J. A., Keiko C. Salazar, Kevin K. Crown, and Brandon L. Servantes (2013). Performance Characterization of Blown Microfiber Filter Media for Airborne Collection of Nuclear Debris. Albuquerque, New Mexico, Sandia National Laboratories.

Hubbard, J. A., J. E. Brockmann, J. Dellinger, D. A. Lucero, A. L. Sanchez and B. L. Servantes (2012b). "Fibrous Filter Efficiency and Pressure Drop in the Viscous-Inertial Transition Flow Regime." Aerosol Science and Technology 46(2): 138-147.

Hubbard, J. A., K. C. Salazar, K. K. Crown and B. L. Servantes (2014). "High-Volume Aerosol Filtration and Mitigation of Inertial Particle Rebound." Aerosol Science and Technology 48(5): 530-540.

Liu, B. Y. H. and K. W. Lee (1976). "Efficiency of Membrane and Nuclepore Filters for Submicrometer Aerosols." Environmental Science & Technology 10(4): 345-350.

Miley, H. S., S. M. Bowyer, C. W. Hubbard, A. D. McKinnon, R. W. Perkins, R. C. Thompson and R. A. Warner (1998). "A description of the DOE radionuclide aerosol sampler/analyzer for the Comprehensive Test Ban Treaty." Journal of Radioanalytical and Nuclear Chemistry 235(1-2): 83-87.

Sanchez, A. L., J. A. Hubbard, J. G. Dellinger and B. L. Servantes (2013). "Experimental Study of Electrostatic Aerosol Filtration at Moderate Filter Face Velocity." Aerosol Science and Technology 47(6): 606-615.

Spencer, M. T., L. G. Shields and K. A. Prather (2007). "Simultaneous measurement of the effective density and chemical composition of ambient aerosol particles." Environmental Science & Technology 41(4): 1303-1309.

Thompson, R. C., Miley, H.S. (2002). Filter Media Recommendation Review. Pacific Northwest National Laboratory.

Valmari, T. P., R., Moring, M. (2000). Testing of different types of flat filtering media for IMS radionuclide stations. Helsinki, Finland, STUK – Radiation and Nuclear Safety Authority, Research and Environmental Surveillance, Airborne Radioactivity.

Yu, C. P. (1977). "PRECIPITATION OF UNIPOLARLY CHARGED PARTICLES IN CYLINDRICAL AND SPHERICAL VESSELS." Journal of Aerosol Science 8: 237-241.

DISTRIBUTION

1 Dr. Gary Stradling, Chief
Treaty Verification Technologies Office
Defense Threat Reduction Agency

1 LTC David Williams
Treaty Verification Technologies Office
Defense Threat Reduction Agency

1 Dr. Benjamin Heshmatpour
Treaty Verification Technologies Office
Defense Threat Reduction Agency

1 Dr. Harry Miley
Pacific Northwest National Laboratory
harry.miley@pnnl.gov

1 Mr. Scott Morris
Pacific Northwest National Laboratory
morris.scott@pnnl.gov

1 Mr. Ian Cameron
Pacific Northwest National Laboratory
Ian.Cameron@pnnl.gov

1 Dr. Joel Forrester
Pacific Northwest National Laboratory
joel.forrester@pnnl.gov

1	MS0404	Neill Symons	05752	npsymon@sandia.gov
1	MS0404	Randy Rembold	05752	rkrembo@sandia.gov
1	MS0968	Karen Rogers	05754	ksroger@sandia.gov
1	MS0968	Jeff Martin	05754	jbmart@sandia.gov
1	MS1218	Joe Sanders	05943	jcsande@sandia.gov
1	MS1219	Charlie Craft	05943	cmcraft@sandia.gov
1	MS0899	Technical Library	09536	libdoc@sandia.gov


Sandia National Laboratories